2007

CHARACTERIZATION OF COLLOIDAL NANOPARTICLE AGGREGATES USING LIGHT SCATTERING TECHNIQUES

Mehmet Kozan
University of Kentucky, mkozan@engr.uky.edu

ABSTRACT OF DISSERTATION

Mehmet Kozan

The Graduate School

University of Kentucky

2007

CHARACTERIZATION OF COLLOIDAL NANOPARTICLE AGGREGATES USING LIGHT SCATTERING TECHNIQUES

ABSTRACT OF DISSERTATION

A dissertation submitted in partial fulfillment of the
requirements for the degree of Doctor of Philosophy in the
College of Engineering
at the University of Kentucky

By
Mehmet Kozan

Lexington, Kentucky

Director: Dr. M. Pinar Mengüç, Professor of Mechanical Engineering Department

Lexington, Kentucky

2007

ABSTRACT OF DISSERTATION

CHARACTERIZATION OF COLLOIDAL NANOPARTICLE AGGREGATES USING LIGHT SCATTERING TECHNIQUES

Light scattering is a powerful characterization tool for determining shape, size, and size distribution of fine particles, as well as complex, irregular structures of their aggregates. Small angle static light scattering and elliptically polarized light scattering techniques produce accurate results and provide real time, non-intrusive, and in-situ observations on prevailing process conditions in three-dimensional systems. As such, they complement conventional characterization tools such as SEM and TEM which have their known disadvantages and limitations. In this study, we provide a thorough light scattering analysis of colloidal tungsten trioxide (WO_3) nanoparticles in the shape of irregular nanospheres and cylindrical nanowires, and of the resulting aggregate morphologies. Aggregation characteristics as a function of primary particle geometry, aspect ratio of nanowires, and the change in dispersion stability in various polar solvents without the use of dispersants are monitored over different time scales and are described using the concepts of fractal theory. Using forward scattered intensities, sedimentation rates as a result of electrolyte addition and particle concentration at low solution pH are quantified, in contrast to widely reported visual observations, and are related to the aggregate structure in the dispersed phase. For nanowires of high aspect ratios, when aggregate structures cannot directly be inferred from measurements, an analytical and a quasi-experimental method are used.

KEYWORDS: Aggregation, Fractal Dimension, Small Angle Static Light Scattering, Elliptically Polarized Light Scattering, Sedimentation Rate

Mehmet Kozan

March 15, 2007

CHARACTERIZATION OF COLLOIDAL NANOPARTICLE AGGREGATES USING LIGHT SCATTERING TECHNIQUES

By

Mehmet Kozan

Dr. M. Pinar Mengüç
Director of Dissertation

Dr. L. Scott Stephens
Director of Graduate Studies

November 27, 2007

RULES FOR THE USE OF DISSERTATIONS

Unpublished dissertations submitted for the Doctor's degree and deposited in the University of Kentucky Library are as a rule open for inspection, but are to be used only with due regard to the rights of the authors. Bibliographical references may be noted, but quotations or summaries of parts may be published only with the permission of the author, and with the usual scholarly acknowledgements.

Extensive copying or publication of the theses in whole or in part also requires the consent of the Dean of the Graduate School of the University of Kentucky.

A library that borrows this dissertation for use by its patrons is expected to secure the signature of each user.

Name	Date

DISSERTATION

Mehmet Kozan

The Graduate School

University of Kentucky

2007

CHARACTERIZATION OF COLLOIDAL NANOPARTICLE AGGREGATES USING LIGHT SCATTERING TECHNIQUES

DISSERTATION

A dissertation submitted in partial fulfillment of the
requirements for the degree of Doctor of Philosophy in the
College of Engineering
at the University of Kentucky

By
Mehmet Kozan

Lexington, Kentucky

Director: Dr. M. Pinar Mengüç, Professor of Mechanical Engineering Department

Lexington, Kentucky

2007

To Bilge…

ACKNOWLEDGEMENTS

I would like to thank my dissertation director Professor M. Pinar Mengüç for the visionary researcher spirit he so enthusiastically shared, the financial support he provided, his patience, and his comments and reviews during the writing of this dissertation. Financial support of the Scientific and Technical Research Counsel of Turkey (TUBITAK) which lasted for two years is also gratefully acknowledged.

Thanks also to my dissertation committee including Professor Kaveh A. Tagavi and Professor Dusan P. Sekulic of UK-Mechanical Engineering Department, Professor Czarena Crofcheck of UK-Department of Biosystems and Agricultural Engineering Department, Professor J. Todd Hastings of UK-Electrical Engineering Department, and Professor Mahendra K. Sunkara of University of Louisville Chemical Engineering Department for serving in my committee and their valuable comments. I would like to thank Professor Sunkara also for his rewarding collaboration on characterization of the nanomaterials synthesized in his lab, and Jyothish Thangala and Rahel Bogale of his research team for preparing the nanomaterials and corresponding SEM images.

This dissertation, while an individual work, benefited from the experimental setup that was built or improved by former graduate students and post-doctoral fellows of Professor Mengüç. Among them Dr. Mustafa Aslan who re-built the setup and shared his expertise generously is gratefully acknowledged. Thanks also to Dr. Sivakumar Manickavasagam for making his broad expertise on the experimental setup always available and for his technical support. The first compact version of the bench-top prototype I took some part in building, has now passed some critical stage in reaching the market—thanks to the efforts of Dr. Manickavasagam, as well as of Professor Mengüç.

The discussions with Dr. Rodolphe Vaillon of INSA, Lyon, his insights and encouragement have been invaluable at various stages of this work. Thanks also for his detailed review of this dissertation. I would also like to express my gratitude to my MS advisor Professor Nevin Selçuk of METU, Ankara, for introducing me to research and for her guidance—even with the distance and the passing of time.

The friends and colleagues at the Mechanical Engineering Department including Professor Bora Süzen, Dr. Basil Wong, Dr. Hui Zhao, and Mathieu Francoeur have always been great support. The discussions with Dr. Ing. Regina Hannemann and Dr. Ing. Jens Hannemann of UK-Electrical Engineering Department and their willingness to share their deep understanding of the intricacies of electromagnetic theory, as well as their friendship is also greatly appreciated.

My heartfelt gratitude is for the deep love that was always made apparent by my parents Nedret and Ibrahim Kozan, brother Melih, and sister Gül. For her loving nature, farsighted mind, her unwavering love, and for making everything worthwhile, Bilge—my wife, thank you.

TABLE OF CONTENTS

LIST OF TABLES

LIST OF FIGURES

NOMENCLATURE

a	:	Radius of particle, [m].
c	:	Speed of light in vacuum, $\frac{1}{\sqrt{\varepsilon_0 \mu_0}} = 3 \times 10^8$ m/s .
c_p	:	Particle-particle separation in a particle laden medium, [m].
D_f	:	Fractal dimension, [-].
E_b	:	Columbic potential energy barrier, [J].
I_{vv}	:	Intensity, vertically polarized incident and detected, [J/m^2].
k_b	:	Boltzmann's constant, 1.3806×10^{-23} J/K.
k_g	:	Structure pre-factor.
$[K]$	:	Stokes vector.
L_s	:	Separation distance between colloidal particles, [m].
m	:	Complex index of refraction of the material relative to that of the medium.
M	:	Mass, [kg].
n	:	Complex index of refraction of the material, or medium [-].
n_a	:	Number of particle in unit volume, [1/m^3].
N	:	Number of primary particles in an aggregate.
N_A	:	Avogadro's number, 6.022×10^{23} molecules/mol.
$P(q)$	:	Form factor.
q	:	Magnitude of scattering wave vector, [1/m].
r_o	:	Primary particle radius, [m].
$\vec{r}$	:	Coordinates of the primary particle.
R_g	:	Radius of gyration, [m].
$[S(\theta)]$	:	Scattering matrix.
$S(q)$	:	Structure factor, [-].
SE	:	Scattering exponent, [-].
T	:	Temperature, [K].
t	:	Time, [s].
$V_{T,\,R,\,A}$	:	Electrostatic potential energy, *T, R, A*: total, repulsive, or attractive, [J].
x	:	Size parameter, [-].

Greek Symbols

ε_0	:	permittivity of free space, 8.8542×10^{-12} C^2 / N·m^2.
γ	:	sticking probability, [-].
λ, λ_0	:	wavelength of light in the medium, in vacuum, [m].
μ_0	:	permeability of free space, $4\pi \times 10^{-7}$ N·s^2/C^2.
θ	:	scattering angle, [^{o}].
ρ	:	density, [kg/m^3].
τ	:	optical thickness, [-].
Φ	:	scattering phase function of the participating medium, [sr^{-1}].

Abbreviations

AFM : Atomic force microscopy.
BET : Brunauer-Emmett-Teller adsorption method.
CCA : Cluster-cluster aggregation.
DLVO : Derjaguin-Landau-Verwey-Overbeek model.
EPLS : Elliptically polarized light scattering.
MIP : Mercury injection porosimetry.
PCA : Particle-cluster aggregation.
PMT : Photomultiplier tube.
RGD : Rayleigh-Gans-Debye theory.
SEM : Scanning electron microscopy.
TEM : Transmission electron microscopy.

CHAPTER 1

PARTICLE CHARACTERIZATION AND NANOTECHNOLOGY — A HISTORICAL PERSPECTIVE

1.1. INTRODUCTION

At the moment nanotechnology enjoys an ever growing interest from the public and from researchers from diverse backgrounds and disciplines. Although the coining of the new and exiting term has undoubtedly contributed to the enthusiasm, there is more to nanotechnology than just being a buzzword used for attracting public attention and more funding. The term itself has first appeared in a conference paper in 1974 by Norio Taniguchi [1, 2]. Nevertheless, the idea of building small is usually attributed to Richard Phillips Feynman, whom some call the greatest physicist of twentieth century after Albert Einstein. Based on a talk he gave in 1959 [3], Feynman laid out a framework in 1961 [4] where machines would build even smaller machines and other products with atom by atom control (a process which was later called molecular manufacturing in [5] which reviews the historical developments in the subject).

Nanotechnology encompasses many disciplines such as chemistry, biology, applied physics, and colloidal science, but is more than a simple extension of existing knowledge into the nanoscale [6, 7]. Instead of working with atoms or molecules in huge numbers (e.g., Avogadro's number, N_A=6.022×10^{23} molecules/mol) as in conventional chemical reactions, a much more limited number of molecules are synthesized or tailored—sometimes by dealing with individual atoms—to yield desired, unusual functionalities with the new methods of nanotechnology [8, 9].

Nanomaterials have long been used in technological applications as pigments in paints and as catalysts in heterogeneous reactions [10]: (p. 5). The sub-micrometer metallic or

metallic oxide particles used as catalysts, however, were traditionally called "microcrystallites" or "microstructures" in the literature. This perhaps was a misnomer since their size ranged between 1-10 nm [11]: (p. 307). The current interest is fueled in part by the potential of finding innovative ways to put new materials with new or improved properties into commercial use, by the prospect of manufacturing with atomic precision, and by the pressure to manufacture even smaller electronic devices following the ongoing success in electronics industry [6], [12]: (p. 159). Realization of such objectives could allow production of materials that reach unprecedented strengths and enable us to reduce energy consumption and environmental pollution [13]; to achieve faster computation and higher storage capabilities [14]; or could result in several new applications in medical sciences such as controlled and targeted release drug delivery [15], medical implants [16, 17] or targeted tissue ablation for cancer treatment [18]. At the core of all these, lie the particles in nanometer scale with various geometric dimensions, shapes, structures, and equally diverse behaviors. In this dissertation we will shed some light on their colloidal behavior.

1.1.1. Colloid Science and Nanotechnology

Initial efforts in nanotechnology were driven by a renewed interest in colloidal science and the achievements on engineering and characterization of nanoparticles. These include novel manufacturing and synthesis techniques (atomic force microscope or AFM, wet chemistry methods, chemical vapor deposition), combined with the availability of a new generation of advanced microscopy tools (AFM, scanning tunneling microscope, scanning near field optical microscope), and the ground-breaking new ways of characterization of irregular structures (statistical description of particle morphology by means of fractal theory).

Colloidal particle systems are at the heart of many products we encounter everyday and are inherently within the borders of nanotechnology. Colloidal suspensions range from biological liquids such as blood and milk to technologically relevant materials such as house hold cleaners, paint and lubricating materials [19]: (p. 748). A colloidal system

consists of two phases which *appear* to consist of only one phase to the naked eye—or did so under the microscopes of the day in 1861 when British chemist Thomas Graham coined the term "colloid" to describe a solution containing particles in suspension. Around the turn of the century, such famous scientists as Rayleigh, Maxwell, and Einstein also studied colloids [10]: (p. 5). As explained in Table 1.1 there are several possible phase combinations where either phase could be a gas, a solid or a liquid (two gas phases will mix on a molecular level and do not form a colloidal system) [20]: (p. 1, 3). The particle dimension in the dispersed phase has traditionally been considered to be in the range 1 nm-1 μm, although unique behavior of colloidal particles can still be observed with particle sizes up to 10 μm [20]: (p. 1). A homogeneous mixture in which the particles are larger than 1 μm in at least one dimension (i.e., larger than the range for colloidal particles) is classified literally as a *suspension* [21, 22], however, we will use these terms interchangeably even for nanowires as long as 10 μm without reading too much into the semantics of the terms.

Colloidal particles dispersed in liquids can be the desired end-product (e.g., pigment particles in paint) [23] or the product of a chemical reaction in the process (e.g., aqueous reduction of metal ions in electronic applications) [24]: (p. 59). Colloidal particles can also be a preferred method of storage or an intermediate step to be further utilized in a later process. The commercial polystyrene latex sphere samples we will use for calibration measurements in Chapter 4 available from Duke Scientific [25] are such an example. It is the characterization of this type of colloidal dispersions without chemical reactions we will exclusively focus on in this dissertation. Several considerations are important in control of colloidal behavior: particle size, sedimentation, dispersion of powders, and stabilization of particles in the dispersion (e.g., during production of and while applying paints). These will also be among the topics covered in the present study, however, other important parameters such as flow properties or sintering of particles (e.g., for optimum conductivity in electronic circuit printing) will not [20]: (p. 4-7).

Although it is possible to construct nanoscale structures with the use of AFM tips [8, 26], lithographic techniques or laser tweezers (utilizing the radiation pressure, i.e., momentum

of photons) [27]: (p. 22), wet chemistry methods and colloidal and cluster science are likely to keep their positions as major players in the field due to advantages in speed (especially compared with AFM) and the yield in producing desired nanostructures rapidly and at a production level that would satisfy the demand [8]: (p. 4), [28]: (p. 19). Not surprisingly, the immediate industrial applications of nanotechnology that have moved from the laboratory setting into the marketplace have been the colloidal nanoparticles in large quantities from the chemical process industries to be used in cosmetics [29, 30], protective coatings, and stain resistant fabrics [6, 31]. Methods for chemical synthesis of complex three-dimensional colloids and patterned arrays are potential candidates in the production of highly functionalized structures at high volumes [28]: (p. 20). Further technological developments that affect everyday lives may not come immediately, but it is reasonable to assume that the research efforts will follow the same path of other successful technological developments (e.g., PCs, biotechnology).

1.1.2. Impact of Nanotechnology on Material Science

It has long been known that optical properties of the material in its bulk form are not necessarily the same for particles of the same material in the molecular or nanometer size range. For example, the wavelength shift in the absorption of light by nanoscale semiconductors was first observed as early as the 1960s for colloidal AgI and AgBr as noted in [11]: (p. 306). Particles in the nanometer size range display unusual physical properties which are quite different from their bulk. This originates from their quantum scale dimensions [28]: (p. 19). Quantum physical effects become dominant for particles with less than about one thousand atoms (e.g., 3 nm for silver nanoparticles) [32]: (p. 151). Effective medium properties have often been used in various forms (such as Maxwell-Garnett theory, Clausius-Mossotti relation and its refinements) to circumvent such hurdles in optical property determination at nanoscales [32]: (p. 173-193), [33-35], [36]: (p. 139), [37]: (p.162). Furthermore, synthesis of “mixed grain” (alloy) or composite (e.g., core and shell configuration of spherical geometries) particles can result in properties that differ from any of the individual constituent material layers. Thus, the

variability (and possibilities) in nanomaterials seems to be so broad that the limits of nanomaterials are not yet in sight [28]: (p. 21), [12]: (p. 145), [38].

The physical and chemical properties of nanomaterials which exclusively originate from the physical phenomena in quantum scales are not always understood to a full extent. There is a great deal of gray areas to be clarified in engineering applications at the border of quantum scales, and the science is more likely to follow the engineering applications [39]. This should be of no surprise, however, since most theoretical explanations and science have followed the observations on the existing engineering applications. For example, there was a thriving electrical industry before the complete theory of electromagnetic theory was laid out, including the introduction of telegraph in 1834, invention of telephone in 1876, and the electric light bulb in 1879—all before James Clerk Maxwell presented his unified set of equations of electromagnetics in 1879 and their experimental verifications were made by Heinrich Rudolf Hertz in 1888 [40]: (p. 4), [41]: (p. 5-6). The same sequence of events also took place in development of the—now standard—thermodynamic charts and tables for properties of steam. A widely agreed standard table first appeared in 1930 [42-44], although the steam engine of James Watts (patented in 1765) was already in widespread use in transportation and manufacturing industries.

In the same manner, nanotechnology uses more of an engineering approach in extending the available knowledge of materials science to smaller scales, rather than using the approach of an exact science. Instead of the conventional chemical reactions which follow an exact analytical formalism, the syntheses of nanostructures from a mere handful of molecules are usually achieved by following “recipes” that result in curious chemical and physical properties. Naturally, it is desirable to have a control on the chemical properties (composition in the surface, interfaces, or the bulk) as well as the structural properties (size, geometry, morphology, crystalline, or amorphous structure) of the synthesized particles [24]: (p. 55). Chemical preparation of nanoscale particles with desired material properties is a “bottom-up manufacturing” approach (as opposed to “top-down”) [45]. As an example, chemical vapor deposition (CVD), with which cylindrical

nanoparticles used in this study were synthesized, is considered a bottom-up approach. A good summary of various well established "wet-chemistry" (i.e., liquid phase) methods (aqueous, or using organic or organometallic reagents) used in materials science to synthesize nanoparticles with desired chemical and structural properties is provided by Chow and Gonsalves in [24]: (55-68).

1.1.3. Effect of Nanoparticle Shape and Size

As discussed before, nanoparticles of various materials or their composites present extraordinary optical, mechanical, electrical, and chemical properties. Bismuth nanoparticles, for example, have a melting point lower than that of its bulk as most other metals, and its nanoparticles exhibit superconductivity, although the bulk material (metallic) does not convert into this state [46]. Their remarkably high specific surface areas (surface to volume ratio) and their high surface energy (compared to their bulk) also make nanoparticles desirable for applications as catalysts [47, 48]. In addition, metallic nanoparticles of different geometries have different crystallographic facets and have different fraction of atoms located on their corners or edges, which influence their catalytic activity for various reactions as a function of their shape. For example, it was shown that platinum nanoparticles are the most catalytically active with a tetrahedral geometry (compared to spherical and cubic) and have the greatest fraction of surface atoms on their corners and edges, while the cubic platinum nanoparticles are the least catalytically active and have the lowest fraction of surface atoms on their corners and edges [48].

Electrical transport properties of polymer films with imbedded metal nanoparticles result mainly from the structure of particle clusters in these layers, and physical properties of constituent nanoparticles play only a minor role. Optical spectra (e.g., scattering and extinction characteristics) of nanoparticles are also a strong function of the geometry, as well as size. As the eccentricity of a spheroidal metallic nanoparticle increases and the geometry deviates from a perfect sphere, the plasma resonance (extinction maxima due to

plasmon excitation of surface electrons) of extinction moves towards lower wavelength values. Its peak magnitude, on the other hand, correlates approximately with the particle volume [32]: (p. 2, 149-150, 154 and 171, Figures 6.2 and 6.15).

Colloidal chemistry has an excellent control over the size of spherical particles of various compositions which affect their physical and chemical properties including conductivity, catalytic activity, and luminescence [49]: (p. 294). Spherical nanoparticles have been used in industrial applications for a long time and are still important, as industrial processes are quite capable to control the variations in eccentricity and the polydispersity in size. Nanostructures with geometries other than spherical are also routinely synthesized now using wet-chemistry methods with higher yields of the desired particle shape. Earlier studies were able to synthesize mostly a mixture of various shapes (e.g., tetrahedral, cubic, prismatic, icosahedral, and octahedral nanoparticles made of platinum) [50]. More recently, monodisperse silver nanocubes [51], thin triangular prisms of silver with flat bases [49], silver tetrahedrons with truncated tops (using lithographic techniques) [52], and high aspect ratio single WO_3 nanowires (using chemical vapor deposition) [53] have been reported in the literature—all except the nanocubes starting from spherical nanoparticles. Furthermore, self organization of colloidal metal nanoparticles in polymer solutions makes extensive management of preferred sizes and structures possible [32]: (p. 1).

It is of paramount importance to develop solution based synthesis methods which would selectively yield the desired particle shapes (and in large quantities) if the full potential of nanomaterials is to be realized. Preserving the resulting shape and keeping these nanomaterials well dispersed and readily available for further utilization is equally important as producing them. Stable dispersion of many nanostructures in a variety of solvents, especially without the addition of a dispersant, however, is extremely difficult to achieve as they tend to agglomerate fairly quickly [54].

1.1.4. Irregular Shapes of Nanoparticle Aggregates and Fractal Concepts

Aggregation is a *physical* process in which the dispersed elementary units, which make up the aggregate, stick to one another irreversibly under the influence of inter-particle forces (van der Waals attraction and Coulombic repulsion due to electrostatic double layer) to form tenuous structures. The two main considerations in the study aggregation of fine particles are the reaction kinetics of the process and the morphology of resulting aggregates. The reaction (aggregation) kinetics has been studied in depth since the insightful study of Smoluchowski in 1916. On the other hand, characterization of particles with irregular geometries has been a cause of much discussion and an agonizing task for scientists and engineers in diverse fields of research (including combustion, astrophysics, atmospheric sciences, and materials science among others). Nanoparticles with non-spherical Euclidian geometries mentioned above (e.g., cube, tetrahedron) have long been categorized as "irregular" [55]. However, there was virtually no mathematics available to define *truly* irregular shapes upon which many sciences depended. For example, long lists of observed shapes of ice crystals, snow flakes, and other particulate matter were named and tabulated since the geometries thereof were central to the research and applications in atmospheric and meteorological sciences [56]: (p. 64, 65), [57]: (p. 78).

A breakthrough in mathematics came about with the introduction of the concepts of "fractal geometry" by Benoit B. Mandelbrot in 1975 [58], which was eventually applied to irregularly shaped particles. What seemed as a peculiar geometrical tool at first, was soon shown to be able to describe not only the complex macroscopic geometrical patterns in nature (snowflakes, clouds, coastlines, and rivers), but also the seemingly random structures of aggregates of fines particles. After the first experiments that explicitly investigated and revealed the fractal nature of aggregated particles in a metal smoke by Forrest and Witten in 1979 [59] (which originated from the PhD study of Forrest as detailed in an interesting historical anecdote in [60]), the 1980s witnessed an avalanche of experimental and theoretical studies of the fractal description of aggregates in colloidal and aerosol systems.

All previous knowledge, which did not benefit from definitions of the fractal analysis, was eventually incorporated in the fractal description of irregular aggregate structures. For example, the power law relation between the mean radius (R) and the total mass (M) of a cluster of particles, $M \sim R^D$, was known long before it was realized to also be valid for fractal structures. As we will discuss in detail in Chapter 2; in fractal theory, the exponential coefficient (D) is called the "fractal dimension" and varies between 1 and 3. For a polymer in a dilute solution, for example, D=2 if the solvent is poor and D=5/3 if good (reported as early as 1953, see [61]: (p. 63), [62]: (p. 22), and Chapter 2 of this dissertation for related discussions)—the same limits which roughly correspond to the now famous cluster-cluster aggregation mechanism. The first models of aggregation mechanism, such as the Eden model, which will be elaborated in Chapter 2 of this dissertation, were developed in 1961 for evolution of tumor cells. The reaction kinetics (time evolution of the concentration) of an aggregate of certain size made up of a number of primary particles, and its size distribution in the suspension was represented by the Smoluchowski equation as early as in 1916 (see [62]: (p. 14-23, 92-99) for a detailed discussion). The relation of colloid stability to the attractive (van der Waals) and repulsive (electrostatic double layer) inter-particle forces that result in observed aggregation regimes (e.g., diffusion limited or reaction limited aggregation) were defined by the DLVO theory (Derjaguin-Landau-Verwey-Overbeek model, see Chapter 2 for details). DLVO approach, which represents resultant interaction energy as a function of several solution properties (e.g., ionic strength and dielectric constant of the aqueous phase), was developed in 1940s (see [63]: (p. 839) and Chapter 2 of this dissertation for a discussion). All these studies were eventually associated with fractal theory and incorporated into the study of aggregates.

Until the introduction of fractal concepts into the characterization of particles in colloid, aerosol and other systems (e.g., atmospheric, astrophysical, combustion) the term "irregularly shaped particle" referred almost exclusively to non-spherical geometries, for the simple reason that their mathematical description was not available [55]. With the use of fractal concepts, the complex structures resulting from aggregation processes, which

could not successfully be described as dense porous spheres or other simple geometries, were statistically described in terms of the concepts of fractal theory. Particles which form these clusters can be of any shape, although are usually approximated as spherical particles.

1.1.5. Use of Electromagnetic Theory in Nanoparticle Research

There is a strong industrial demand for finding new ways to achieve stable dispersions of nanomaterials of various geometries and compositions both with and without the use of certain dispersing agents [53]. These nanomaterials have countless potential applications in industry provided that their geometries are well characterized and their aggregation patterns in solutions are well understood. Determining the structure and physical properties of aggregates of nanomaterials (whether occurring naturally or resulting in industrial applications), and how they evolve demand observation and control in real time [64]: (p. 648), [65]: (p. 261). For example, the photo induced (irradiating the nanospheres with fluorescent light) conversion of silver nanospheres into triangular prisms is a time dependent process [49]: (see their Figure 2). The researchers had to resort to the use of time consuming TEM image analyses for process control, despite the fact that they had set forth the bulk production of the desired shape as their goal. Moreover, no information was available on the stability of the resulting dispersion. It is clear that further developments in nanotechnology will continuously demand reliable, rapid, in-situ characterization tools for colloidal systems.

Characterization of colloidal particles can be achieved using advanced microscopy techniques such as SEM (scanning electron microscopy), TEM (transmission electron microscopy), or AFM (atomic force microscopy). Although provide useful information and are necessary in a complete characterization study, such techniques have their known shortcomings of being limited to 2-D observations, of having the risk of modifying aggregate structure during handling, and the potential of orientational biasing [53]. Most importantly, these techniques lack the thoroughness needed in describing the processes that lead to the observed dispersion and sedimentation behaviors, such as the aggregate

morphologies and the aggregation rates [66]. Static light scattering measurements such as the small angle static light scattering and the elliptically polarized light scattering (EPLS) techniques, on the other hand, sample large numbers of aggregates at a time, and provide a statistical average of the aggregate mixture. These techniques have been proven to be powerful *in-situ* characterization tools that can produce accurate results rapidly, and provide details about the size, size distribution, shape and structure of aggregates [53, 67-71]. For a summary of other aggregate characterization methods, including gravitational settling and 2-D image analysis, the reader is referred to [67].

After the landmark description of fractal phenomena by Mandelbrot in 1975 [58] and the pioneering work of Forrest and Witten in 1979 [59] in applying the fractal theory to irregular structures of aggregates, non-intrusive fractal aggregate characterization by means of optics came as yet another breakthrough. Characterization of aggregates of fine particles by fractal theory using both light and x-ray scattering experiments was first achieved by Schaefer and coworkers in 1984 [72]. Extensive in-situ aggregation studies that employ light scattering techniques are available in the literature, but chiefly on clusters which are formed by nearly spherical particles. These studies exploit the fact that most clusters exhibit fractal behavior in determining their size and structure—much like other seemingly random growth phenomena [73, 74]. Aggregation behavior of primary particles in shapes other than spheres does not necessarily present the same patterns as spherical nanoparticles in the same solvents, but their experimental and theoretical characterization remains neglected—a topic which we will lay out the theoretical explanation of in Chapter 2 and investigate in the following chapters.

The underlying principles in using the scattering of light and optical spectra of nanomaterials and their aggregates for in-situ characterization are described by one of the most well established branches of physics—electromagnetics [75]: (p. xii). The success of electromagnetics lies in the existence of a satisfactory set of equations which are verified with conclusive experimental observations. The laws of electromagnetics was discovered in bits and pieces (by Coulomb, Ampere, and Faraday to name but a few), but it was James Clerk Maxwell who in 1879 put together all previous findings into one

consistent and complete set of equations, although he died eight years too soon to see their experimental verification by Hertz in 1888. Maxwell is also well-known for his contributions to thermodynamics with yet another set of equations that also bears the name Maxwell's equations [40]: (p. 4), [41]: (p. 6), [75]: (p. xii). The impact of electromagnetic theory was fundamental and far reaching, and provided a unified theory for many previously observed phenomena.

Electromagnetic theory describes all matter through its explanation of the inter-molecular forces that hold all matter in place and govern the chemical reactions, as well as the interactions of light based on its electromagnetic wave nature with matter, i.e., optics. Inspired by the success of Maxwell's equations, physicists have tried to come up with other unified treatises ever since, but without much avail. Einstein, for example, was haunted by the thought of finding a *unifying* theory that would encompass quantum mechanics and the Newtonian mechanics. Quantum mechanics is the physics of sub-atomic particles which was developed in 1920s, and had superseded the theory of special relativity developed by Einstein in 1905. Einstein introduced his revolutionary theoretical description of special relativity for objects moving near the speed of light where Newtonian mechanics failed. Since Einstein's failed attempt of unified field theory, quantum field theory which combines special relativity and quantum mechanics (introduced in 1930s), the electroweak theory (1960s), and in more recent years the string theory (also dubbed the "theory of everything") have been proposed all with limited success [75]: (p. xii, xiii).

Application of Maxwell's equations to scattering from spherical gold colloids by Ludvig Lorenz in 1891 and by Gustav A. Mie in 1908 have had a long lasting impact on the particle characterization literature and the so-called Lorenz-Mie theory continues to serve as a benchmark for both experimental and numerical studies [27, 36, 76]. In fact, we will utilize the results based on this theory in probing scattering characteristics of aggregates of particles in the shape of circular cylinders in the following chapters. As described in a biographical article [77], Mie himself did not mention this study as one of his major accomplishments in his auto-biography and regarded his formulation a mere application

of electromagnetic theory to experimental investigations of his doctoral student Walter Steubing. Although he suggested extension of his work to ellipsoidal particles, he was much involved with developing a comprehensive theory that would encompass Maxwell's equations as were many of his contemporaries and never worked on the subject again [77]: (p. 4698). Exact solutions of Maxwell's equations for light scattering from a particle of arbitrary shape are not available. However, exact analytical models on infinite cylinders and many exact numerical models for arbitrary shaped (Euclidian) particles, as well as fractal aggregates have since been developed and applied in numerical schemes (e.g., AGGLOME [78, 79], DDSCAT [34, 80]).

1.2. SCOPE AND ORGANIZATION OF THE DISSERTATION

In this dissertation, we provide a thorough light scattering analysis of the effect of geometry of nanoparticles and solution properties on aggregation patterns, aggregation rates, and morphology of resulting structures formed in various commonly used polar solvents without the use of dispersants. The nanomaterials we consider are made of tungsten trioxide (WO_3) and are in the shape of spherical nanoparticles or nanowires of various aspect ratios. The effect of solvent rheology on degree of aggregation and its change in time, as well as the effects of solution pH and electrolyte concentration in the solution are also investigated. In each case, we provide interpretation of experimental results based on fundamental principles from radiative transfer and Lorenz-Mie theory, as well as detailed comparisons with theoretical and experimental investigations in previous studies in the literature.

Aggregation characteristics of suspended nanomaterials as a function of geometry, aspect ratio of nanowires, and the change in dispersion stability in time are described in terms of fractal theory. Vertically polarized incident and scattered light intensities (I_{vv}, for short) and elliptically polarized light scattering technique (EPLS) are used to determine spatial extend (radius of gyration, R_g) and fractal dimension (D_f) of the aggregates. For WO_3 nanowire samples of high aspect ratios for which D_f can not directly be inferred from

measurements, an analytical and a quasi-experimental method both based on spherical primary particle formulations are used to determine I_{vv} and the D_f. Experimental data on aggregates of these geometries are interpreted based on the Porod limit analogy of the Lorenz-Mie theory.

In Chapter 2 we lay out the theoretical foundation required to analyze the I_{vv} and EPLS measurements. The interparticle interactions and solution parameters that lead to observed aggregation characteristics and resulting aggregate structures are discussed. Mathematical formulations for fractal description of aggregates and aggregation mechanisms are given. Extracting a number of useful information from the measured scattering intensity profiles and corresponding analytical formulations for theoretical predictions with regards to light scattering principles are described. We discuss the experimental setup developed at the Radiative Transfer Laboratory and expanded over time with contributions from several of our alumni in Chapter 3, including this author. The experimental procedures followed during the measurements are also summarized in the same chapter. In Chapter 4, the differences in aggregation patterns for WO_3 nanowires of different aspect ratios and the morphology of resulting aggregates are investigated from their light scattering profiles, which are also compared with those for aggregates of WO_3 spherical nanoparticles. In Chapter 5, we investigate the effect of solvent rheology on aggregation behavior and dispersion stability of WO_3 nanowires in commonly used polar solvents and suggest possible aggregation patterns based on the experimental measurements. Chapter 6 aims to quantify the aggregation and settling rates when the same nanowire suspensions at various concentrations are introduced in a monovalent electrolyte solution. We conclude in Chapter 7 with remarks on possible ways to further the investigations presented in this dissertation by improvements in theoretical treatment of experimental analyses and by numerical predictions. We also provide suggestions on extending these studies with new forms of nanowire assemblies or to new nanostructures.

Table 1.1. Types of colloidal dispersions (adopted from [20]).

Phase (Dispersed / Continuous)	Gas (bubbles)	Liquid (droplets)	Solid (particles)
Gas	-	Liquid aerosol (mist)	Solid aerosol (smoke)
Liquid	Foam (shampoo)	Emulsion (mayonnaise)	Sol (ink)
Solid	Solid foam (packaging)	Solid emulsion (butter)	Solid sol (stained glass)

CHAPTER 2

DETERMINATION OF FRACTAL AGGREGATE STRUCTURE BASED ON STATIC LIGHT SCATTERING

2.1. INTRODUCTION

Determining the structure and properties of aggregates, whether occurring naturally or resulting from an industrial application, and their evolution in time is important for understanding and better control of these processes [64]: (p. 648), [65]: (p. 261). The particles that form these aggregates could be of any shape, although many of them can be approximated as small, spherical particles (called primary particles, spherules or monomers) which join together to form tenuous clusters (also called floccules, flocs, agglomerates, or aggregates) [65]: (p. 261), [81]: (p. 1379). A floccule is a mass formed by the aggregation of a number of fine suspended particles, resembling wool, especially in a loose fluffy organization [82], which cannot successfully be approximated as dense porous spheres or other simple shapes.

These geometries can be statistically described in terms of the concepts of fractal theory. As discussed in Chapter 1, fractal geometry has provided the long awaited mathematical tools to describe complex, chaotic and disordered systems, where use of conventional geometrical tools fails [67]. A fractal is an object or quantity that displays self-similarity—on all scales. The object need not exhibit exactly the same structure on all scales, but the same *type* of structures, characterized by "fractal dimension" D_f, must appear on all scales [83]. Its ability to describe "scale invariance" (also called dilational symmetry) from a speck of dust to groups of galaxies is the main feature that is useful for characterization of fine particles [67]. Many interesting applications of the fractal concepts to seemingly random phenomena in nature, including a mathematical model for intricate events of history have been presented in the literature [73, 74].

Aggregates of fine particles are not fractals in the strict sense of the word, since their scaling is only observed over a finite range of length scales, and should be called "natural fractals" [67]: (p. 8, 9). Fractal nature in the aggregation process was demonstrated experimentally, shortly after the pioneering work of Mandelbrot [58], first by using two-dimensional TEM analysis [59], and subsequently by x-ray scattering [72].

2.2. DESCRIPTION OF FRACTAL AGGREGATES

2.2.1. Statistical Scaling Law

The mass (M) of fractal aggregates scales with an overall size (R) according to the simple power law relation

$$M \propto R^{D} \tag{2.1}$$

where D is a measure of fractal characteristics of the aggregate, called the mass fractal dimension [68]: (p. 545), [67]: (p. 6). Assuming a monodisperse size distribution for the primary particles that are spherical in geometry, the mathematical description of a fractal aggregate is given as

$$N = k_g (R_g / r_o)^{D_f} \tag{2.2}$$

where N is the number of primary particles comprising the aggregate, R_g is its radius of gyration, r_o is the radius of primary particles, k_g is the structure pre-factor, and D_f is the fractal dimension of the aggregate [64]: (p. 648). Radius of gyration of an aggregate should not to be confused with its outer (or collision) radius, R_o, which is the size of the smallest sphere that will fully encompass the aggregate [67]: (p. 23). R_g represents an imaginary spherical boundary centered on one (geometrical center) of the constituent primary particles. This is the size that is measured in scattering experiments in the

Rayleigh-Gans-Debye (RGD) limit, as will be discussed below in detail. Radius of gyration used in this study is equal to the root-mean-square distance of mass elements (primary particles) of *identical* composition centered at $\vec{r}_i$, from the geometrical center of mass $\vec{r}_c$, of the aggregate [65]: (p. 262), [67]: (p. 6), [68]: (p.545)

$$R_g^2 = \frac{1}{N}\sum_{i=1}^{N}\left|\vec{r}_i - \vec{r}_c\right|^2 + r_o^2 \tag{2.3}$$

with

$$\vec{r}_c = \frac{1}{N}\sum_{i=1}^{N}\vec{r}_i \tag{2.4}$$

The above definition of R_g with the r_o^2 term yields unity in the limit N=1, e.g., in the case of a single hollow sphere with its mass concentrated in the mantle. It represents a better physical definition, although is not used in most other studies in the literature. For the most general case of primary particles with heterogeneous properties (and excluding the r_o^2 term), R_g is defined as

$$R_g^2 = \int \rho(\vec{r})(\vec{r} - \vec{r}_c)^2 d\vec{r} \Big/ \int \rho(\vec{r}) d\vec{r} \tag{2.5}$$

2.2.2. Universality of Aggregate Fractal Dimension

The fractal dimension cannot assume an arbitrary value. The sparsest possible way of connecting a set of points, e.g., as in a line corresponds to fractal dimension D_f=1, whereas that of a compact structure as in a sphere corresponds to D_f=3. Although, real processes that form *natural fractals* may impose additional limitations [67]: (p. 8), in a real physical process, fractal dimension for most aggregates assume a value within the range [67]: (p. 7-8)

$$1 \le D_f \le 3 \tag{2.6}$$

For an object to remain a single connected entity its fractal dimension must be at least 1, because a line is the sparsest possible way of connecting a set of points, hence the lower limit. Likewise, the fractal dimension must be less than or equal to the dimension of the space in which the fractal exists, or else the space cannot "contain" the fractal [67]: (p. 7). In the above equation d=3 was used for the upper limit, corresponding to the three-dimensional space that the fractal object (aggregate) is in [84]: (p. 65), [85]: (p. 383).

Fractal dimensions higher than 3 have been reported in the literature, especially in the early studies of aggregation when the use of fractal theory was still being discovered [86], [62]: (p. 64). The forth dimension, for example, can be visualized as the path that an ant would follow on the surface of a braided metal wire, similar to those used in telephone poles to secure them to the ground [87]. The convoluted thin wire follows a path in the direction of the cylindrical axis, but goes on around the surface of an imaginary cylinder (adjacent to the other wires). Higher dimensions are harder to visualize, but should be regarded as some other ways of conveniently describing certain fractal geometries.

However, as Martin and Hurd have stated, any value of *aggregate* fractal dimension greater than 3 would be unphysical, since it would correspond to an arbitrary increase in density of the fractal aggregate with radius [84]: (p. 63). This can be seen by using Eq. 2.1 above such that

$$\rho = \frac{M}{V} \propto \frac{R^{D_f}}{R^d} = \frac{1}{R^{d-D_f}} \tag{2.7}$$

where a value of D_f greater than d=3 (for the three-dimensional space) corresponds to an exponential increase in density.

Fractal aggregates can be formed by addition of particles onto larger structures (clusters), or by addition of existing clusters in the system with one another. Both particle-cluster aggregation (PCA) and cluster-cluster aggregation (CCA) have been observed to occur in formation of fractal aggregates in nature and in industrial applications. Short range interparticle potentials control the sticking probability of particles and the resulting structures [88]: (p. 1416). Resulting aggregate structures can be classified according to their formation mechanisms. Each mechanism has "universal" features that are characterized by certain values of D_f (diffusion limited, reaction limited, ballistic, to name a few) [89]: (p. 590).

The analysis of Weitz and coworkers [88] appear to be the first study to determine that different fractal dimensions are associated with different physical mechanisms (aggregation kinetics) of irreversible cluster-cluster aggregation in accordance with interparticle interaction energies (see discussions of the DLVO model below). The now universally agreed range in the literature for cluster-cluster type aggregations is

$$\sim 1.8 < D_f < \sim 2.1 \tag{2.8}$$

Lower D_f limit is a result of diffusion limited cluster aggregation (DLCA), when a collision between clusters *always* results in the formation of a bond. DLCA mechanism produces open, frail looking, tenuous structures. When collisions of particles *rarely* result in formation of bonds, the clusters have high D_f values and are said to follow a reaction limited cluster aggregation (RLCA) mechanism. These structures are still quite tenuous, but are noticeably more compact and look stronger [67]: (p. 8). Figure 2.1 illustrates the association of highly porous, open structures with low fractal dimension (D_f=1.8), and low porosity, compact structures with high fractal dimension (D_f=2.1). Other aggregate morphologies with very low fractal dimension (D_f=1.4) observed for polarizable clusters, and compact spherical aggregates as a result of diffusion limited particle-particle aggregation (D_f=2.6) are also shown and will be discussed below. Although characterization of the structure does not explicitly reveal information about the type of bonds between the constituent particles (e.g., hard or soft agglomerates), identification of

the type of structure (open or compact) does indicate the nature of the agglomerate formation mechanism [90]: (p. 36). For the fractal aggregates which are formed under similar conditions, the D_f value remains similar over a range of sizes, hence can be used to characterize formation mechanisms of the aggregates (e.g., combustion conditions in aerosols) [85]: (p. 383). With this information it may also be possible to qualitatively estimate agglomerate bond type (hard or soft agglomerates), leading us to the most appropriate dispersion methodology [90]: (p. 37).

Similarities in the nature of aggregation irrespective of the type of material of the primary particles were proven (hence the term "universal") even when the interparticle bonds between particles were quite different (e.g., metallic, chemical, or van der Waals) [91]. In a rare study of aggregates formed by non-spherical primary particles, Vincze and coworkers also found that the shape (~140 μm long carbon rods with 35 μm diameter) and size of primary particles (R_g <2.7 mm or R_g>2.7 mm) affect basic features of aggregation only to a certain extent, and the "universality" of D_f with primary particle geometry remains [92]: (p. 7457, Table 2 and 3). In hindsight, the study was limited to a two-dimensional geometry at the water-air interface, and two dimensional images were used to predict the D_f. The extension of the analysis to three-dimensional systems to examine the universal limits on D_f for fractal aggregates formed with primary particles of cylindrical geometries (rods, wires, fibers, but also other Euclidean geometries) using numerical simulations (see the discussion below) and light scattering techniques as experimental verifications are also needed, which coincide to a certain extent with the aim of this dissertation.

Higher fractal dimensions are reported in the literature, e.g., for hematite aggregates in the range $2.3<D_f<2.9$ [93]. Although it was claimed in this study that the lower end corresponds to diffusion limited aggregation and the upper end to reaction limited aggregation processes, the exact mechanism was not associated with a CCA mechanism. Such high fractal dimension values are usually attributed to a (diffusion limited) PCA mechanism, though there is *no* "universal" agreement on the limits of PCA mechanism. The most commonly referred limiting value is the one reported for the diffusion limited

PCA of D_f=2.5 [62]: (p. 64), [89]: (p. 590). Other proposed D_f values ranging from 2.75, 2.8, or 3.0 using different computer simulations based on PCA mechanism have been compiled and cited by Brasil and coworkers in [94]: (p. 496).

Fractal dimensions higher than D_f>3 have been reported in the literature in the context of surface roughness or porous materials for which the light is scattered predominantly from the surface, rather than the bulk of the aggregate (mass fractals) [93]: (p. 242). Surface roughness of a solid particle which can be described in terms of surface fractal dimension, D_s, has caused high fractal dimension measurement of monodisperse hematite spheres when a static light scattering technique was used [93]. This explanation is based on the well-known relation between aggregate structure factor ($S(q)$) and the magnitude of the scattering wave vector (q)

$$S(q) \sim q^{D_s - 2d} \tag{2.9}$$

for a d-dimensional space where $d>D_s>d$-1 [84]: (p. 65). Scattering exponent (SE), which is the exponent of q in the above equation, is used in $SE=D_s$-6 to solve for D_s in the familiar three-dimensional space. SE is also the slope determined from the small angle light scattering experiment as will be discussed below. On the other hand, an accurate fractal description has been shown to be an exception not the rule with the use of BET (Brunauer, Emmett, and Teller) adsorption or MIP (mercury injection porosimetry) methods for porous materials, such as clay or active carbon, which often resulted in D_f>3 [95].

2.2.3. Interaction of Particles Leading to Fractal Aggregation

As pointed out by Lin and coworkers [91], fractal aggregates can be formed by primary particles sticking through chemical bonds (e.g., metallic bonds between gold nanoparticles, or siloxane bonds between SiO_2 nanoparticles due to high pH in solution). However, van der Waals attraction is also commonly observed in aggregating systems (e.g., between polystyrene latex nanoparticles), even when the surface charge distribution

is not interfered with by use of chemical agents or electrolytes [91]. The origin of aggregation kinetics for small particles can be understood by considering the nature of their short range interactions. The stability in particle laden suspensions is generally imparted by the DLVO-type "electric double layer" *repulsion* of similar charges, whereas aggregation of particles into larger clusters can be initiated by the addition of moderate amounts of a simple inert electrolyte to "screen" the repulsion and give way to the van der Waals *attraction* [67]: (p. 3), [96]: (p. 800), [97].

When a conducting system is put into contact with a conducting media, as in the case of a colloidal particle in a solvent, their physical interface gives rise to the "electrical double layer", so named because it implies the formation of two different charge distributions of opposite sign on each side of the interface (ideally with no charge transfer between the two phases) [96]: (p. 800), as shown in Figure 2.2. The van der Waals attraction stems from fluctuating dipole moments within the particles. Dipole moments, in turn, form due to the electric polarizability of the material which the particles are made of [19]: (p. 747). The strength of van der Waals attraction is determined by the difference of refractive indices of the colloidal material and the surrounding liquid.

DLVO model describes the interactions between primary particles based on the energy balance of the two opposing forces. The Healy-Hamaker analytical formulations were employed to define interparticle potential energy and compare these calculations against experimentally observed aggregation behaviors and limits as a function of electrolyte concentration in [98]: (p. 6415, 6417 and Figure 6), [99]: (p. 4918), [100]: (p. 362-363). The total potential energy of interaction between two particles in an aqueous dispersion was obtained by summing electric double layer repulsion (V_R) and van der Waals attraction (V_A) potentials

$$V_T = V_R + V_A \tag{2.10}$$

The repulsion potential which is a function of solution temperature, the surface charge (which determines the Coulombic potential energy barrier, E_b), and the ionic

concentration in the solution (which determines the screening length L_s), can be overcome partially or altogether by either adjusting the electrolyte concentration, or simply by the *random collision* of particles in the solution [62]: (p. 3-5), [88]: (p. 1418), [98]: (p. 6415). V_A is usually represented with a negative sign [98]: (p. 6415). Therefore, the total potential energy with negative values in Figure 2.2 correspond to colloidal particle interactions that would result in aggregation [101]. Colloidal particles can come into rest in the weak *secondary* minimum (e.g., see middle curve in Figure 2.2), at which point "deflocculation" can still occur [98]: (p. 6418). Only those particles with sufficient thermal energy (k_BT) can surmount the potential energy barrier, E_b, and enter the deep, *primary* minimum from which the particle escape is virtually impossible, i.e., "irreversible aggregation" [98]: (p. 6418).

The probability of two particles sticking upon approaching each other within a distance L_s is defined by Weitz and coworkers in [88]: (p. 1418) and in [99]: (p. 4918) as

$$\gamma \simeq e^{-E_b / k_b T} \tag{2.11}$$

where k_bT is the thermal energy of the particles, k_b being the Boltzmann constant, and T the absolute temperature.

In the case when an electrolyte in the solution reduces the surface charge on the particles only slightly (so that the solution ionic concentration is not altered too much), the electrostatic repulsive barrier E_b decreases and the sticking probability increases. However, the small amount of surface charge displaced corresponds to only a small amount of decrease in E_b. Since the thermal energy is still at a small value,

$$E_b \geq k_b T \tag{2.12}$$

and the reaction (sticking) probability is still low (or, $\gamma \ll 1$) [88]: (p. 1418), several number of collisions are required before two particles (or clusters) can successfully stick

to each other [100]: (p. 362). However, the repulsive forces that are present between the particles are not insurmountable, therefore the aggregation rate is only limited by the time it takes for two clusters to overcome the barrier by thermal activation (reaction limited aggregation) [91]: (p. 360). At this point, the aggregation rate is very sensitive to the electrolyte concentration. Since the probability of sticking is so low, the aggregating particles will have the opportunity to explore a large number of configurations, and penetrate deeper into the aggregate, thus result in denser aggregates with higher D_f (i.e., the upper limit in Eq. 2.8 above) [88]: (p. 1418).

Addition of sufficient amounts of electrolyte, on the other hand, could displace all the surface charge, so that

$$E_b \ll k_b T \tag{2.13}$$

and the sticking probability is much higher. In this case, there is negligible repulsive force between the particles, so that the aggregation rate is limited solely by the time taken by clusters to encounter each other by diffusion (diffusion limited, rapid aggregation) [91]: (p. 360). This corresponds to the lower curve in Figure 2.2, in which case the particle surface charge is neutralized by the electrolyte and the potential energy barrier is eliminated [98]: (p. 6418), called "electrostatic screening" [62]: (p. 4). D_f is low since the particles react irreversibly if they encounter even the outer branches of the fractal aggregate (i.e., the lower limit in Eq. 2.8 above). By comparing the thermal energy, k_bT, with the potential energy barrier, E_b, sticking probability of particles can be approximated which in turn can be used to deduce the limits of aggregation reaction regimes, as illustrated in Figure 2.3.

In both regimes, the energies of the bonds formed upon sticking are higher than E_b, the particles are trapped in a potential energy well, hence the growth is *irreversible* [88]: (p. 1418). On the other hand, the particles can also come to rest at a weak potential energy minimum (e.g., if the repulsive barrier is not demolished with a high electrolyte concentration), from which deflocculation is still possible. This *secondary* potential

energy minimum leads to *reversible* aggregation [63]: (p. 839), [98]: (p. 6418), [99]: (4918). The electrolyte concentration above which no further increase in aggregation rate is observed corresponds to the onset of rapid aggregation [98]: (p. 6417). The transition concentration at which slow aggregation gives way to rapid aggregation is called the "critical coagulation concentration", although conflicting definitions are offered in the literature [98]: (p. 6416, 6417).

A commonly used property in colloidal dispersion characterization is the "zeta potential". It is a measure of the magnitude of the repulsion or attraction between particles, and is an important property of colloidal dispersion which helps identify colloid stability [102]. The zeta potential is the overall charge a particle acquires in a specific medium. The magnitude of the zeta potential gives an indication of the potential stability of the colloidal system. If all the particles have a large negative (or positive) zeta potential they will repel each other and there is dispersion stability. The higher the absolute zeta potential, the stronger the Coloumbic repulsion between the particles, and therefore the lesser the impact of the van der Waals force on the colloid [101]. If the particles have low zeta potential values then there is no force to prevent the particles from coming together and the dispersion is unstable. A dividing line between stable and unstable aqueous dispersions is generally taken at ±30 mV. Particles with zeta potentials outside these limits are normally considered stable [103].

The most important factor that affects zeta potential is the pH. A zeta potential value should in principle be quoted with a definition of its environment (pH, ionic strength, concentration of any additives). Usually when the dispersion pH is below or above a range of pH values (e.g., ±30 mV), the zeta potential reaches a constant value (positive or negative) and the dispersion would stabilize due to the (positive or negative) surface charges [104]. Most oxides tend to be positively charged at low pH and negatively charged at high pH. As the pH is raised, the charge (or zeta potential) becomes more negative [105]: (p. 2). Obviously, then, there is a pH value somewhere on the scale where the particles have no charge. This is called the "isoelectric point", around which the dispersion is least stable [104], [105]: (p. 2).

2.3. LIGHT SCATTERING ASPECTS

Light scattered off a colloidal particle carries with it important information about the shape, size, size distribution, and its aggregate structure. Light scattering techniques, such as the small angle static and the elliptically polarized light scattering (EPLS), stand out as an accurate, rapid, non-intrusive, and in-situ characterization method. Although we have focused exclusively on light scattering techniques in this dissertation due to the numerous advantages mentioned above, other techniques of aggregate characterization are also available in the literature. For a discussion of the strengths and limitations of such methods as image analysis and hydrodynamic investigation of settling, we refer the reader to the review article by Bushell and coworkers [67].

2.3.1. Limits of Applicability

Determination of fractal structure from light scattering measurements is based on the Rayleigh-Gans-Debye (RGD) theory. The basic approach of RGD theory is to model the scattering body as a collection of Rayleigh scatterers that do not interact with each other. The total scattered wave is the sum of scattered waves from each of these components which add constructively to produce a total scattered intensity proportional to N^2 [64]: (p. 651, 652), [67]: (p. 11). If also the suspension is sufficiently dilute, the interaction between aggregates can be described as independent scattering [27], and the scattered intensity is proportional to $n_a N^2$, where n_a is the number density of aggregates in the solution [64]: (Figure 22). Note that the N^2 dependence comes from the relation of intensity (I) to amplitude of electric field (E)

$$I = \varepsilon_0 c \left\langle E^2 \right\rangle_t \tag{2.14}$$

where the brackets indicate time averaging over a finite time t, ε_0 is the electric permittivity of free space, and c is the speed of light in vacuum [41]: (p. 39, 45, 49).

In most cases the Rayleigh scatterers are too close to not interact with one another. When aggregates are dense and the primary particles are not small compared to the wavelength of incident light, the near field effects come into play. Scattering is affected by shadowing, dependent scattering effects and multiple scattering, which in principle could invalidate the RGD conditions upon which the fractal dimension analysis is based [67]: (p. 46). However, formulations based on the RGD theory still provides conservative limits given the fact that D_f is determined from the slope on a log-log plot of the scattered intensity (I_{vv}) rather than its absolute value (as will be discussed below). RGD theory is valid provided the following conditions are satisfied

$$|m-1| \ll 1 \tag{2.15}$$

$$\frac{2\pi n}{\lambda_0} L|m-1| \ll 1 \tag{2.16}$$

where L is the characteristic length of the scattering body and m is the *relative* complex refractive index of scatterers in the medium [67]: (p. 11, 13), [27]: (p. xxi, 384, 401). Note also that the refractive index of the medium is included in the above equation to reflect the value of wavelength in the medium, rather than its value in vacuum (λ_0) [41]: (p. 103), n being the complex refractive index for the medium (and not of the particle)

$$\lambda = \frac{\lambda_0}{n} \tag{2.17}$$

Much research was devoted to determine the limits of applicability of RGD theory in the literature. The established view is that the RGD theory for fractal aggregates is valid, since the effect of "multiple scattering" *within* an aggregate (i.e., the interparticle electromagnetic interactions) is relatively small [64]: (p. 673, Figure 21, or see p. 663-673 for an in depth review). In one such study, using a coupled-dipole approximation for light scattering calculations, Singham and Bohren observed that the dipole-dipole

interaction between monomers of a fractal aggregate looses its significance because the fractal nature corresponds to a fluffy structure, composed of distant monomers; as opposed to solid particles of a compact geometry [106]. The interactions for open, tenuous aggregates of D_f<2 was found to be negligible, and was still not significant even for more compact aggregates of D_f=2.5. These observations were also found to be in line with previous findings that the dipole-dipole interactions are less significant in rods or disks compared to relatively more compact geometries such as solid spheres [106]: (p. 1433).

Experimental determination of D_f on a log-log plot is a robust technique provided that RGD conditions are satisfied, hence we do not need to elaborate on *multiple* scattering. However, it is interesting to note the differences in terminology in different analyses performed by researchers in Optics and Radiative Heat Transfer communities. The radiative transfer equation (RTE) is based on attributing a ray nature to light and is an engineering approach to determine the behavior of intensity in participating (absorbing, emitting, or scattering) media. The interaction between particles usually refers *not* to the primary particles within an aggregate, but rather to larger particulate matters (solid or tenuous geometries) seen in particle laden systems and named as "dependent scattering" [27]: (p. 385), [76]: (p. 569-570). At low particle volume fractions, and sufficiently high particle-particle distances (c_p), there will be no systematic relation between the phases of scattered waves [107]: (p. 5). Hence, the "macroscopic" light scattering formulations (RTE computations) reduce to more easily manageable forms, such that total scattering is simply the *summation* of those from each particle in a unit volume [27]: (p. 393), and the particle-particle interaction is called "independent scattering". Hence, "single" or "multiple" scattering refers only to the number of interactions that a pencil of rays of intensity encounters in the medium, and can be either dependent or independent depending on the conditions prevailing in the participating medium. Single scattering prevails if optical depth (or thickness) is less than 0.1 (or τ<0.1) [27]: (p. 299-300). For 0.1<τ<0.3 a correction for double scattering may be necessary. For still larger values of τ, multiple scattering becomes an important factor [107]: (p. 4-5). Dependent effects may

be ignored as long as volume fraction of particles is low (f_v<0.006), or particle separations is high (c_p/λ>0.5) [27]: (p. 385).

2.3.2. Determining Aggregate Morphology from Scattered Intensity Patterns

Scattered intensity from a fractal aggregate at q that corresponds to scattering angle θ (for a constant wavelength in the medium) is conceptualized as the product of two functions

$$I(q) \propto S(q)P(q) \tag{2.18}$$

where form factor $P(q)$ describes the scattered intensity function from an individual primary particle, and the structure factor $S(q)$ describes the additional scattered intensity due to spatial correlation between the particles in the aggregate, where q given by

$$q = |\vec{q}| = \frac{4\pi n}{\lambda_0} \sin\left(\frac{\theta}{2}\right) \tag{2.19}$$

is the magnitude of the scattering wave vector, and n is the refractive index of the dispersion medium, λ_o is the in vacuum wavelength and θ is the angle at which the radiation is scattered [67]: (p. 11). $P(q)$ is effectively constant at small q, while $S(q)$ is effectively constant at large q. Therefore, the overall variation in $I(q)$ at large q is due to primary particles $P(q)$, and overall variation at small q is entirely due to aggregate structure effects $S(q)$.

Structure factor represents the total scattered intensity at $\vec{r}_d$ (e.g., PMT detector) as a result of the incident electric field on a scatterer (e.g., primary particle) at $\vec{r}_p$ normalized over the total number of primary particles N [64]: (p. 651). This means, $S(q) \propto I(q)N^{-2}$, or

$$S(q) \propto N^{-2} \left| \sum_{i=1}^{N} e^{i\vec{q}\cdot\vec{r}_i} \right|^2 \tag{2.20}$$

A rigorous derivation of the above equation from first principles can be found in [64]: (p. 650-651). When the summation is replaced by the integration and fractal geometry of the aggregate is incorporated, $S(q)$ can be determined analytically. Various forms of analytical solutions are proposed in terms of auto-correlation function and cut-off function. The auto-correlation function emerges due to the convolution theorem employed in the integration, and is a measure of probability of spatial distribution of primary particles. The cut-off function, on the other hand, forces auto-correlation function to drop to zero outside the aggregate territory (since the fractal aggregates are not "infinite" in extent, but rather "natural" fractals) [64]: (p. 655-662), [67]: (p. 6-7, 13-16), [68]: (p. 546, 547), [108]: (p. 1323, 1324-1325). As a result of RGD scattering, the aggregate structure factor has the following form

$$S(q) \propto q^{-D_f} \tag{2.21}$$

In the case of small angle static light scattering experiments, the measured scattered intensity corresponds to an "optical structure factor" [64]: (p. 673). The above proportionality can be used to determine D_f from the negative slope of the linear region of a log-log plot of I versus q measurement (where $I(q) \propto S(q)$ only), such as in Figure 2.4. This corresponds to the range

$$\frac{1}{R_g} \ll q \ll \frac{1}{r_0} \tag{2.22}$$

which is called the fractal scattering region.

In the region $q<1/R_g$ (i.e., to the left of fractal scattering region), all N scatterers of the aggregate scatter in phase in accordance with the above described RGD behavior. Scattered intensity in this region is independent of scattering angle and essentially

constant. An increase in the number of aggregates in a system which obeys independent scattering regime would result in a comparable increase in scattered intensity proportional to $n_a N^2$. As the aggregates become larger with time, they also contribute to the increased forward scattering as well [109]: (p. 190). The so-called "Tyndall effect" refers to the observation that in an aggregating system comprised of a constant number of primary particles, the increase in forward scattering (for scattering angles corresponding to $q<1/R_g$) due to the increased number of scatterers (that are now a part of the larger fractal aggregate) is accompanied by a constant slope in the fractal scattering region which does not vary as the aggregation progresses [64]. The typical Tyndall effect results in a parallel shift in intensity in the fractal scattering region (hence the constant D_f) [109]: (Figures 4 and 5).

As q increases a change of slope in scattered intensity profile is observed. The region where q dependence first occurs is defined as the Guinier regime, and is used to measure R_g near $q=R_g^{-1}$. Beyond this length scale, the transition from the Guinier region to the fractal scattering region takes place. Fractal dimension D_f, should be determined away from this transition region at

$$qR_g \gg 1 \tag{2.23}$$

possibly for $qR_g \backsim 5$ [68]: (p. 552).

On the other end of the fractal scattering region at high q is the Porod scattering regime. The overall variation in intensity $I(q)$ at large q is due to primary particles, hence $I(q) \propto P(q)$. In this region, the length scale of the scattering experiment can resolve the size of individual monomers [68]: (p. 542, Figure 6). This can readily be understood if we notice that the length scale of experiments q, contains in it the wavelength of incident light, i.e., $q^{-1} \sim \lambda_o$, following Eq. 2.19.

Length scale of a particle and the incident light is conveniently compared in the form of size parameter, $x=\pi L/\lambda$, where L is the characteristic length of the particle. If the particle can be approximated as a sphere, L is $2a_{eff}$, where a_{eff} is the effective radius of the particle of any shape which has the same volume as that of a sphere of radius a_{eff}. Constant fluctuations in scattered intensity pattern in the Porod regime are characterized by q^{-4} dependence. This power law dependence is a direct result of the scattering from smooth surfaces (in this case primary particles), described by the Lorenz-Mie scattering theory for spherical particles (has the same q^{-4} dependence) [68]. The equation for the form factor, $P(q)$, is analogous to and has the same functional form as the differential scattering cross section—i.e., normalized scattered intensity profile—of a Lorenz-Mie sphere [36]: (p. 72), [68]: (p. 541, 546, 554).

Experimental measurement of vertically polarized incident and scattered (detected) light, I_{vv}, with respect to magnitude of scattering wave vector q provides the same information that a theoretical determination (as discussed above) of structure factor would give [64]: (p. 674). The suggested procedure of analysis is to first determine R_g from a plot of the Guinier equation, and then use this value to fit a D_f to the scattered light profile [68]: (p.552).

R_g is best determined from analysis of scattering in the Guinier regime, where $qR_g<1$, which corresponds to $I(0)/I(q)<4/3$ according to the Guinier equation expressed as

$$\frac{I(0)}{I(q)} \cong 1+\frac{1}{3}R_g^2 q^2 \tag{2.24}$$

The plot of $I(0)/I(q)$ versus q^2 remains linear well beyond these limits and the slope yields $R_g^2/3$ [64] : (p. 675, 676). Although the plot of $I(0)/I(q)$ versus q^2 remains linear (the slope yields $R_g^2/3$) beyond these limits for systems with polydispersity in aggregate size [64], this relation should be used cautiously and only when there is sufficient amount of measurements at low q [53].

An important note on experiments based on the small angle light scattering techniques is that they inadvertently detect scattering from an ensemble (fractal or not) of cluster sizes. The polydispersity in the cluster size causes the shape of the structure factor to be different than that for a single cluster size [64]: (p. 661). A narrow size distribution causes a rapid transition (i.e., a higher D_f), whereas a wide size distribution causes a slow transition to the fractal scattering region [67]: (p. 12). This is similar to the effect of polydispersity in primary particle size [110]: (see their Figures 1 and 2, compare D_f=1.5 for the mixture of 70 nm and 600 nm particles to D_f=1.78 for the mixture of 70 nm and 216 nm particles). I_{vv} when plotted against scattering vector, q, hence gives an effective structure factor for the ensemble, S_{eff}. The R_g measured by the experiment is then the average radius of gyration, $\langle R_g \rangle$ [64]: (p. 676).

Polydispersity in primary particle size also causes the sharp ripples observed in the Porod regime to fade away, however the q^{-4} dependency originating from the Lorenz-Mie spheres remains [68]: (p. 542), [111]: (p. 596). The ripple structure observed in Porod regime in scattered intensity profile resembles that of a Lorenz-Mie sphere, in the form of minima separated by maxima ("Mie lobes"). As the size parameter of primary particles of the fractal aggregate increases, the crossover from Rayleigh scattering to Guinier regime overlaps with the non-linear scattering of primary particles observed in Porod regime [110]. Therefore, experimental data can be interpreted based on the Porod limit analogy of the Lorenz-Mie theory.

For a Lorenz-Mie sphere size of known size, the location of the first dip in the scattering profile roughly corresponds to the scattering angle determined from the well-known Fraunhofer diffraction from a circular aperture of radius a [68]

$$\theta \cong 1.22\lambda / 2a \tag{2.25}$$

Lorenz-Mie scattering theory also shows that as the size parameter of a single spherical particle increase, an effect similar to that caused by polydispersity is to take place. The high frequency variations the of the intensity profile is smoothed out with size parameter

at intermediate values of q, however, increase vigorously at higher values of q [68]: (Figures 4 and 6). The depth of the first dip is also a consequence of the size parameter, which smoothes out and gets shallower the higher the x is. The slope of the curve corresponding to the first Fraunhofer diffraction dip is thus less steep as a result of the shallower first minima for spheres with higher x. Polydispersity in particle size, too, causes the minimum to be a shallow dip unlike observed in the case of a solid sphere uniform in size [64, 111]. Information provided by the Lorenz-Mie theory on the Porod limit of fractal scattering profile will be used to analyze, albeit qualitatively, the monomer sizes of aggregates considered in this study.

Several additional experimental observations were provided by Bushell and coworkers [110] (along with theoretical explanations) on how the polydispersity in primary particle size can alter several aspects of scattered intensity profiles of fractal aggregates. They have shown that due to the increased inter-particle spacing when large nanoparticles are present together with smaller ones, Rayleigh scattering region is confined to a narrower range, and the linear fractal scattering region is distorted at high q (Porod region) as the scattering from individual monomers starts to dominate [110]: (see their Figures 6 and 7). Since the primary particles used in this study are in the shape of long cylindrical nanowires, a similar increase in inter-particle space or dilution of the fractal structure can be expected. In fact, a shorter Rayleigh scattering regime and bulged, non-linear behavior at high q at the far end of the fractal scattering region were observed in most experimental scattering profiles presented in the following chapters of this dissertation. On closer inspection, the comments made in [110] on the Porod limit of the fractal scattering region based on dilution of fractal structure with large monomers, and the observations we have provided above based on the Lorenz-Mie scattering as a function of size parameter x, could in fact prove to be complementary to each other. Nevertheless, further inspections of both results are required for more definitive conclusions. A yet another important finding by Hasmy and coworkers [112] on the effect of polydisperse primary particles is that the transition point between the fractal scattering and the Porod regimes migrates towards lower q values (much like the effect of large size parameters in

moving the Porod regime towards fractal scattering region (or vice versa) so as to cover most of the light scattering profile) [109]: (p. 191), [112]: (Figure 2).

2.3.3. Determining Aggregate Morphology from Elliptically Polarized Light Scattering Measurements

Elliptically polarized light refers to the harmonic electromagnetic wave, the resultant electric field vector ($\vec{E}$) of which (when decomposed into its components) has two perpendicular components with unequal amplitudes that are out of phase from each other at relative phase differences *other than* integer multiples of $\pm\pi/2$. Note that *odd* multiples of $\pm\pi/2$ is its special case of spherical polarization and that of $\pm\pi$ is linear polarization [41]: (p. 319-322).

The intensity and polarization state of light can be described by four Stokes parameters in the form of a column vector [*K*].

$$[K] = \begin{bmatrix} I \\ Q \\ U \\ V \end{bmatrix} \tag{2.26}$$

where *I* represents the total intensity, *Q* the difference between the horizontally and vertically polarized intensities, *U* the difference between the $+45^{o}$ and -45^{o} intensities, *V* the difference between the right-handed and left-handed circularly polarized intensities [90]: (p. 37). These four parameters can be obtained by using a set of filters in front of the beam. An insightful interpretation was also given by a previous work done at the Radiative Transfer Laboratory [113]:

Imagine a set of four filters, each of which, under natural illumination, will transmit half the incident light. The first filter is isotropic, letting waves in all polarization settings go

through. The second filter is a linear polarizer oriented horizontally. The third filter is a linear polarizer oriented at 45 degrees from horizontal in the clockwise direction. The fourth is a circular polarizer opaque to cylindrical polarization states. By measuring the irradiance that passes through each of these filters individually, (I_1, I_2, I_3, and I_4) we can construct the Stokes vector.

$I = 2I_1$	This is simply the irradiance of the original beam.
$Q = 2(I_2\text{-}I_1)$	Tendency to be horizontally (>0) or vertically (<0) polarized.
$U = 2(I_3\text{-}I_1)$	Tendency to be linearly polarized to $+45^o$ (>0) or -45^o (<0).
$V = 2(I_4\text{-}I_1)$	Tendency to be circularly polarized right (>0) or left (<0).

Note that here, I is the intensity (irradiance in some textbooks [41]: (p. 49)) of the beam, and Q, U, and V describe its state of polarization.

The incident and scattered Stokes vectors are related through the scattering matrix [S]

$$[K]_s = [S][K]_i \tag{2.27}$$

where

$$[S(\theta)] = \frac{1}{k^2 r^2}\begin{bmatrix} S_{11} & S_{12} & 0 & 0 \\ S_{12} & S_{22} & 0 & 0 \\ 0 & 0 & S_{33} & S_{34} \\ 0 & 0 & -S_{34} & S_{44} \end{bmatrix} \tag{2.28}$$

and k=1/λ is the wave number and r is the distance from the center of the particle to the detector, θ characterizes the angular nature of this relation [90].

The change in Stokes vector [K] of the incident light is due to its interactions in an optical setup. The scattering matrix [S] of the optical system contains in it the product of

scattering matrix elements of the optical components as well as the scattering medium under investigation and is represented as

$$[S]_{sys} = \left[P_{2,W}\right] \cdot [QWP_Z] \cdot [S]_{par} \cdot [QWP_Y] \cdot \left[P_{1,X}\right] \tag{2.29}$$

where scattering matrices for ideal polarizer and quarter plates can be found in [36, 69]. In this formulation we are interested in determining the six independent elements of the scattering matrix of the particle suspension in the sample cell, $[S]_{par}$.

Elements of the scattering matrix S_{ij} provide information about the randomly oriented particles in the scattering medium. It is comprised of a sequential product of scattering matrices of the optical components in an optical experimental setup, as well as that of the scattering medium. The 4×4 matrix is the sum of the individual scattering matrices for each particle in a cloud of particles, and reduces to the six elements given above for a randomly oriented cloud of particles [69]: (p. 284). A distribution of particle sizes or shapes will produce a different angular profile for each of the scattering matrix elements [90]: (p. 37).

Elliptically polarized light scattering (EPLS) technique can be a powerful tool to identify particle morphology and can be used to determine particle size and shape for conventional as well as fractal geometries. Experimental determination of fractal dimension from EPLS using scattering matrix elements was studied in a recent work [90]. Structure factor is expressed in terms of two of the scattering matrix elements

$$S(q) = S_{11} - S_{12} \tag{2.30}$$

The fractal dimension is then determined in a similar manner from the negative slope of the linear region of a log-log plot of S_{11}-S_{12} versus q measurement. This was shown to be a viable method in determining the fractal dimension of aggregates of one dimensional geometries, such as single and multi-walled carbon nanotubes [114, 115]. Further details

of the EPLS technique used this study will be discussed in the following chapter on experimental set up.

2.4. ANALYTICAL FORMULATIONS FOR FRACTAL AGGREGATES

The scattered intensity profile due to spatial arrangement of primary particles can be taken into account analytically by means of the widely used analytical relation derived by Chen and Teixeira [116]: (p. 2584). It was modified by Amal and coworkers [117]: (p. 316) to its final form as

$$S(q) = 1 + \frac{D_f \Gamma(D_f - 1) \sin\left[(D_f - 1)\tan^{-1}(qR_c)\right]}{(qr_o)^{D_f}\left[1 + 1/(qR_c)^2\right]^{(D_f-1)/2}} \tag{2.31}$$

where Γ is the gamma function, which can be found utilizing IMSL Mathematical and Statistical Libraries imbedded in Compaq Visual FORTRAN [118]. R_c is the characteristic cut-off radius determined by

$$R_g = \sqrt{\frac{D_f(D_f - 1)}{2}} R_c \tag{2.32}$$

The above relation for $S(q)$ was simplified with the assumption $R_c \to \infty$ [119] for the range of q values used, and reduced to

$$S(q) = 1 + \frac{D_f \Gamma(D_f - 1)}{(qr_o)^{D_f}} \sin\left[\frac{(D_f - 1)\pi}{2}\right] \tag{2.33}$$

which will also be used in this study. The scattered intensity from an individual spherical primary particle is given by [119]

$$P(q) = \left(\frac{4}{3}\pi r_o^3\right)^2 \left[3\frac{\sin(qr_o) - qr_o\cos(qr_o)}{(qr_o)^3}\right]^2 \tag{2.34}$$

Thus,

$$I(q) = N_p(\rho - \rho_0)^2 S(q)P(q) \tag{2.35}$$

where N_p is the number density of primary particles, (ρ-ρ_o) is the difference of scattering length densities between primary particles and the solvent [116]: (p. 2584).

The use of $I(q) \propto S(q)P(q)$ would ensure representation of scattered intensity from a fractal aggregate made up of *monodisperse* spherical primary particles over the entire range of q values. D_f can be determined through a least squares analysis by matching the scattered intensity, which was expressed as the product of the analytical expressions for structure and form factors given above, to the experimental data points [117].

Another method suggested by Hasmy and coworkers [119], which takes into account polydispersity in primary particle size, employs the fact that scattered intensity for large size parameter particles can be approximated solely by the form factor in the Porod regime at large q (i.e., $I(q) \propto P(q)$). Any discrepancy from the measurements is, hence, attributed to the interparticle relations characterized by the structure factor ($S(q)$). By using $P(q)$ averaged over a particle size distribution together with the experimental measurements of scattered intensities a quasi-experimental average $S(q)$ is determined

$$\overline{S(q)} \propto I_{vv}(q) / \overline{P(q)} \tag{2.36}$$

A small polydispersity in particle diameter z is introduced to the scattered intensity from an individual spherical primary particle by using a Gaussian probability distribution function $g(z)$ truncated for $z<0$, which accounts for the finite values of the minima in the scattered light intensity profile.

$$\overline{P(q)} = \int_0^\infty P(q)g(z)dz \tag{2.37}$$

with

$$g(z) \sim \exp\left(-\frac{1}{2}\left[\frac{z - z_o}{\sigma} \right]^2 \right) \tag{2.38}$$

The Gaussian distribution function parameters z_o and σ are adjusted so as to provide the best fit between the average form factor $\overline{P(q)}$ and the experimental scattered intensity profile. Initial guess can be improved by making use of the fact that the first minimum in scattered intensity profile from an individual spherical particle roughly corresponds to the scattering angle determined from the well-known Fraunhofer diffraction from a circular aperture [68]: (p. 542).

Unlike the Chen and Teixeira method [116], where the analytical formulas for both terms in $I(q) \propto S(q)P(q)$ were used, fractal dimensions are determined in the second step of the analysis (instead of from $S(q)$ only). Structure factor computed from the Hasmy et al. method [119] using $\overline{S(q)} \propto I_{vv}(q)/\overline{P(q)}$, is normalized such that $\overline{S(q)}/\overline{S(q_{\max})} \to 1$ for $q_{max} \to \infty$

$$\frac{\overline{S(q)}}{\overline{S(q_{\max})}} = \frac{I_{vv}(q)/\overline{P(q)}}{I_{vv}(q_{\max})/\overline{P(q_{\max})}} \tag{2.39}$$

Despite the corrections needed for multiple scattering, refraction and shadowing effects in the RGD approach with high size parameter primary particles, this procedure was able to predict most features of the structure factor, and was shown to be a viable way of accurately predicting fractal dimensions of different aerogels that have gone through a

cluster-cluster aggregation process with primary particle size parameters as high as x=300 [119]: (p. 9352).

It should be emphasized, however, that the use of analytical formulas for $S(q)$ and $P(q)$, which were originally derived for spherical primary particles, will inadvertently generate certain inaccuracies when used for modeling cylindrical primary particles of tungsten trioxide (WO_3) nanowire aggregates of this study. To what extent the formulas provide satisfactory approximations of the experimental findings is explored in the following chapters.

2.5. SIMULATION OF FRACTAL AGGREGATE STRUCTURES

Computer simulations have played a significant role in understanding structure of fractal aggregates, since it is difficult to devise experiments that can isolate the aggregation mechanisms discussed above [67]: (p. 4). Numerical simulations that generate fractal-like structures are based on algorithms that imitate formation of fractal geometries in nature. In general, these "mimicking" algorithms can be divided into two classes along the same lines of experimentally observed mechanisms: particle-cluster aggregation (PCA) algorithm in which the simulation is based on the assumption that aggregation occurs between isolated particles and clusters, and cluster-cluster aggregation (CCA) algorithm which is based on aggregation between clusters [65]: (p. 262). In any case, it is assumed that the formation of basic units ("nucleation"), has completely been achieved when aggregation phenomena start to take place [62]: (p. 2).

Other algorithms, such as the ballistic model where straight line particle trajectories randomly located in space are assumed, are usually limited to representing fractal aggregates observed in aerosols [62]: (p. 66). Ballistic versions of both PCA and CCA models create more compact aggregates, which is more dramatic for the CCA model than for the PCA [62]: (p. 86). Although "sequential algorithms" were used in the literature to obtain a quick picture of structures resembling a fractal aggregate, where identical

particles are added on randomly one by one and adherence of the resulting aggregate to the statistical scaling law is checked at each such step [120]: (p. 2858), such algorithms were shown to be poor substitutes of "mimicking" algorithms as they exhibit certain discrepancies from fractal properties [65]: (p. 264).

2.5.1. Particle-Cluster Aggregation Models

All PCA models follow an iterative rule in which, starting from a seed particle at the origin, particles are added one after another on the aggregate [62]: (p. 52). The PCA algorithm allows constructing aggregates with a wide range of fractal dimensions, but is more suitable for compact clusters with larger fractal dimensions, i.e., $2.1<D_f<3.0$. For lower D_f values the aggregates created with a PCA model lose their fractal properties even though the statistical scaling law is satisfied [94]: (p. 492).

A detailed discussion of several PCA models, along with suggestions of certain variations to the original algorithms is presented in the landmark compilation by Jullien and Botet [62]: (p. 52-76). The two well-known PCA models are the Eden model [121] and the Witten-Sander model [122, 123]. In the Eden model, the addition process is based on a random cellular growth or random selection of the site that the new aggregate will be added, whereas in the Witten-Sander model the addition is based on a diffusive (Brownian) motion (or random walk) of the new particle until a vacant site which neighbors an occupied site is reached. "Brownian motion" of colloidal particles was first recorded by the botanist Brown while studying a suspension of pollen grains in the microscope. The cause of this motion is, in turn, the motion of the molecules making up the suspending fluid. All of the atoms or molecules are in random or thermal motion and at any given instant the local concentration of a small volume element of the fluid will be either higher or lower than the global average concentration. The thermal motion of the colloidal particles will tend to be in the direction of the lower molecular densities. As these fluctuate in a random manner, so does the directional motion of the colloidal particles. [20]: (p. 1-2). Neither of the two models (Eden or Witten-Sander) is rigorously

self-similar, but are still considered "self-affine" fractals for which the repeating units are somewhat biased on one direction [62]: (p. 30, 72).

As a historical note, it is interesting to note that the Einstein's PhD dissertation on Brownian (diffusive) motion has found its way into the particle aggregation (especially in *dynamic* light scattering experiments), as well. According to the famous Einstein-Stokes the aggregate size (hydrodynamic radius, R_h) is related to the thermal energy k_bT of particles mentioned above (along with translational diffusivity coefficient, D, in the solution of viscosity η) [100]: (p. 357).

$$R_h = \frac{k_b T}{6\pi\eta D} \tag{2.40}$$

Eden model is a commonly used method and has three versions suggested by [62]. In Version-A, the new particle is added on a non-occupied site neighboring to a site occupied by one of the monomers of the existing aggregate, by choosing this site at random among all the possibilities. Initially, *all* of the empty neighboring sites of the existing fractal aggregate have the same chance to accept the new particle. Version-B, which was the *original* algorithm proposed by Eden, considers all unsatisfied bonds, i.e., all nearest-neighbor couples of sites, where one site is occupied and the other is empty. One of these bonds is chosen at random and the new particle is added on the corresponding empty site. An empty site bound by more than one bond to occupied sites of the aggregate, has more chance to accept the new particles in Version-B than in Version-A, because it is counted more than once. In yet another variant (Version-C) first illustrated in [124], any particle of the aggregate has, a priori, the same chance to accept a new particle in its neighborhood. One particle of the aggregate is chosen at random and all the neighboring sites are investigated. If there are some empty neighboring sites, the new particle is added at random on one of these sites [62]: (p. 52, 53).

The differences experienced in the three versions in short length scales are no longer seen for sufficiently large sizes, however Version-C is the method recommended in the

literature [125]. The highly tormented appearance of the aggregate surface due to the random nature of Eden model can be observed in the example given in Figure 2.1, which was developed using the built-in random number generator in Microsoft FORTRAN Power Station [126] following the modified Eden algorithm Version-C.

Like the Eden model described above, Witten-Sander model is also based on random addition of particles on the existing cluster. A particle is placed as the seed at the origin. A point is chosen at random on a circle of large radius centered on the origin, and a particle which is released on the lattice site nearest to this point starts a random walk on the lattice, and as such, essentially is a statistical Monte-Carlo simulation [86]: (p. 1495). The random walk, which simulates the Brownian motion of a particle in a fluid, continues until the particle irreversibly sticks to the seed particle at a vacant neighboring site. The particle is assumed to have drifted away, if it travels to a point of predetermined distance away from the seed, or the cluster after sufficient enough iterations. This is usually three times the radius of the imaginary circle the particle was launched from [86]: (p. 1497), or five lattice steps (lattice spacing is equal to a monomer diameter in Witten-Sander model) more than the largest arm of the cluster [62]: (p. 61, 62). Witten-Sander model results in compact fractal aggregates of about D_f=2.5, when a sticking probability of 1.0, which corresponds to instantaneous, diffusion limited reaction, is assumed [123]: (p. 606), [62]: (p. 64).

2.5.2. Cluster-Cluster Aggregation Models

CCA type simulations allow particles and clusters to diffuse according to a specified trajectory (usually Brownian or linear) and stick irreversibly (according to a specified probability) with no restructuring at a point of contact. This type of simulation imposes natural limits on the resulting fractal dimensions such that the fractal dimension range $1.8<D_f<2.1$ observed in the experiments is recovered by the numerically generated fractal aggregates, as well. In the most popular "hierarchical" approach, which was built on a similar approach for PCA of Witten-Sander model and was concurrently proposed in two different studies [127, 128], clusters that have only the same number of primary particles

are allowed to stick each other to form progressively larger aggregates [62]: (p. 78), [94]: (p. 492), [129]. A detailed discussion on CCA models can be found in the same book by Jullien and Botet referred for PCA models in [62]: (p. 77-102).

CCA algorithms can be utilized to obtain fractal aggregate structures in the entire range of fractal dimensions $1.0<D_f<3.0$ in the three-dimensional space. Although seems plausible at first sight, the probability of finding numerically generated fractal aggregate structures of $D_f>2.1$ rapidly approaches to zero as the aggregate size (N) increases, when a CCA algorithm is adopted [94]: (p. 492). Experimentally observed fractal dimensions that are smaller than predicted by CCA mechanisms were also modeled taking into account electrostatic attraction biases. The existence "polarizable" clusters with opposite electrical charges can overcome the Brownian motion and result in quite linear structures ($D_f\sim1.4$) due to aggregation of clusters tip-to-tip [130, 131].

2.5.3. Restructuring in Fractal Aggregates

In general, the aggregation models mentioned above assume that neighboring primary particles touch each other at a single point, despite the fact that strong attraction forces or lack of rigidity, e.g., sintering at high temperatures, can cause a degree of overlap under different conditions [94]: (p. 492). Aside from such sintering behaviors, restructuring of structures can occur in case aggregate suspension suffers some shearing forces. This is unlike the event of breakage of individual monomers which can be seen in certain suspensions (e.g., in the case of very high aspect ratio cylindrical rods, where the geometry of the primary particles makes them more susceptible to shear that we will present in the following chapters), but is rather due to breakage and redistribution of interparticle bonds within the aggregate as when a branched structure collapses onto itself [94]: (p. 493).

Structures resulting from salt-induced perikinetic aggregation, for example, are so weak as to restructure at the slightest shear introduced by an attempt to transfer them from one vessel to another [67]: (p. 19). Even in the absence of hydrodynamic forces that would

shear the aggregate and bend branches, the van der Waals attraction forces will ensure that primary particles will bond one another when brought close enough within the aggregate, thus may cause restructuring [67]: (p. 10). Hydrodynamically induced restructuring, however, is in general not a self-similar process. At small enough scales no restructuring should be expected because the differential velocity will be small. The differential fluid velocity will increase with the length scale. Eventually a length scale above which the structure will be torn apart will be reached for a given shear rate [67]: (p. 19).

CCA models produce fractal aggregates having coordination numbers exactly equal to two because the probability of forming more contact points is vanishingly small for a primary particle in the absence of restructuring. Each aggregation event thus results in the formation of one and only one bond. In the case of aggregation of real colloidal particles coordination number may be somewhat higher due to some degree of restructuring [67]: (p. 9). Several researchers have tackled this problem in the literature in terms of both quantifying and modeling of the restructuring in aggregates [94, 132]. Hydrodynamic forces due to sedimentation in the suspension is not generally regarded as strong enough to cause restructuring of the aggregates (e.g., in the experiments reported by [33]: (p. 187, 190), although the density difference between WO_3 nanomaterials and water is somewhat higher than for their hematite-water suspension).

2.6. ADDITIONAL CONSIDERATIONS ON FRACTAL AGGREGATES

Fractal description is not sufficient to fully characterize an aggregate. For example, strength of the structure is related to the number (called “coordination number”) and types of bonds existing between primary particles. The influence of restructuring on coordination number was studied on numerically generated aggregate structures in [112], coordination number distribution functions in numerically generated aggregates that have undergone restructuring were presented in [94]. In the case of natural processes that lead to fractal aggregates some degree of restructuring is inevitable, and coordination numbers

higher than 2 should be expected [67]: (p. 9-10). On the other hand, the aggregate structure consisting of only cylindrical primary particles can be more rigid than that of spherical particles due to their particular connections as seen in Figure 2.5 (e.g., sticking of two cylinders along their lateral surfaces), such that alternative definitions of coordination number might need to be developed [92]: (p. 7454 and Figure 4).

Spherical primary particles growing on a fiber were constructed in [133, 134], and aggregation of linear strips in two-dimensional space was simulated in [135]. In the asymptotic limit with sufficient number of primary particles, similar limits on D_f are obtained if primary particles of geometries other than spherical are used as the *seed* particle according to [62]: (p. 68). Although a thorough analysis in three-dimensional systems based on simulations of fractal aggregate formation with cylindrical and other primary particle geometries seems to be missing in the literature, as is the case for experimental verification using light scattering techniques.

The effect of triangular, square, and hexagonal lattice structures on fractal dimension was compared in [136-138]. Lattice structure is very influential on the fractal dimension (e.g., for the Witten-Sander model [62]: (p. 76)), in contrast with the early findings that the cubic lattice produced essentially the same D_f with non-lattice simulations (i.e., by considering all possibilities of a 4π solid angle on a sphere for the random walk) [86]: (p. 1499-1500, 1504-1505). The issue of diffusion direction of non-spherical primary particles (e.g., WO_3 nanowires) can also be quite important since these geometries may not have the three-dimensional symmetry as spherical particles. The value of structure pre-factor k_g can be important in some applications, but was overlooked in the literature until several experimental and numerical studies were compiled and the numerically determined k_g values were found to be inferior to those from experiments [81]: (p. 1381), [67]: (p. 31-35) including aggregates with overlapping primary particles (e.g., due to sintering) [94]: (p. 492). Fractal dimension distribution in a suspension of aggregates with different structures were taken into account by means of a “configurational averaging” in [90, 94, 139].

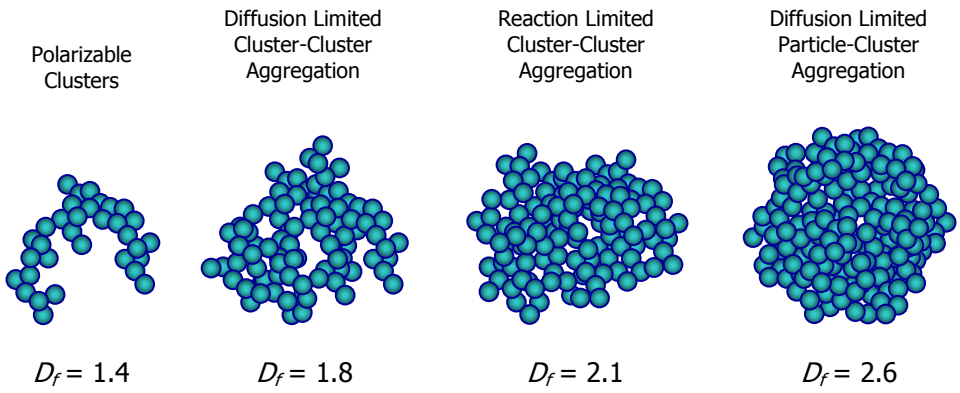

Figure 2.1. Schematic of aggregate structures of limiting fractal dimensions.

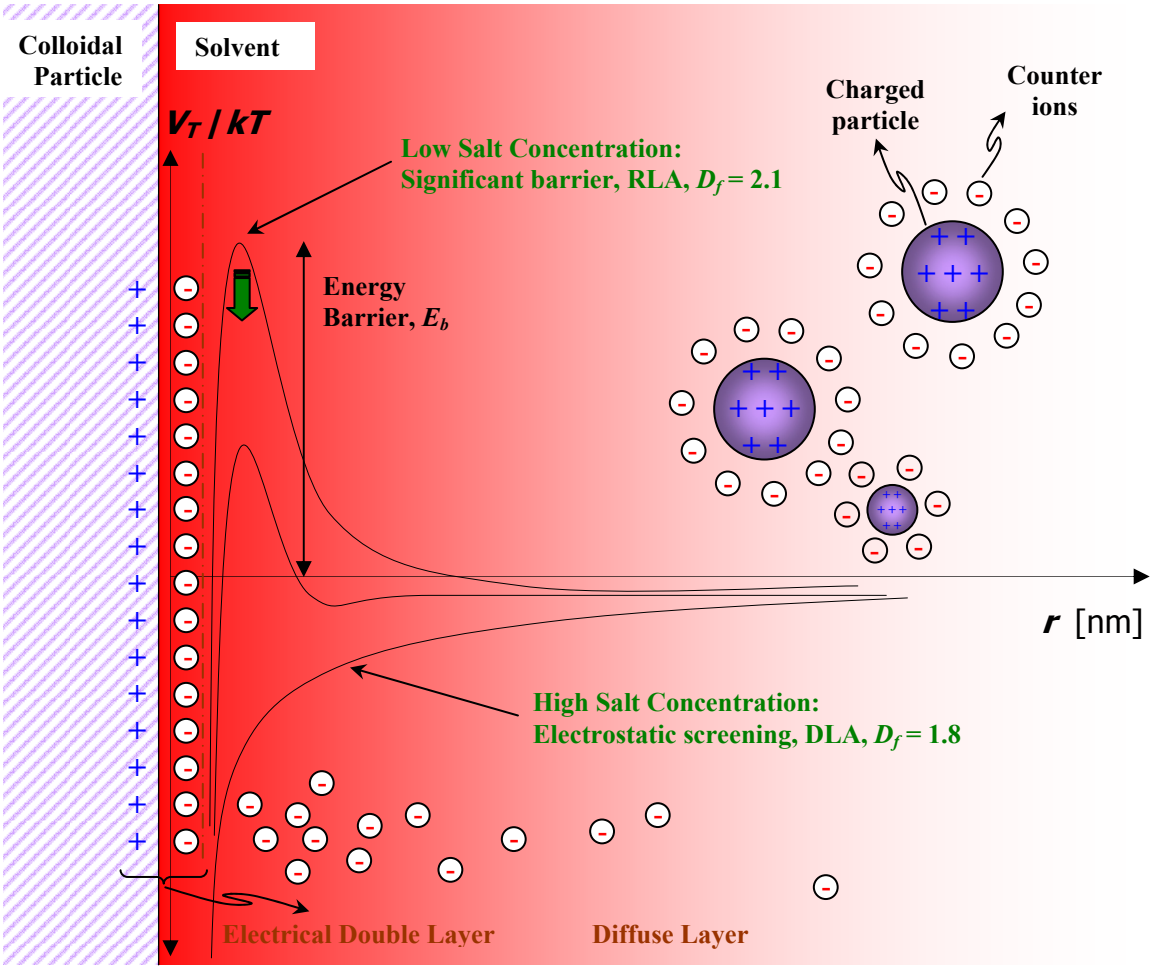

Figure 2.2. Potential energy between charged colloidal particles (clusters) in an electrolyte solution as a function of separation distance between particles and electrolyte concentration. (For theory see text in §2.2, and references [19, 98, 100, 101, 140, 141].)

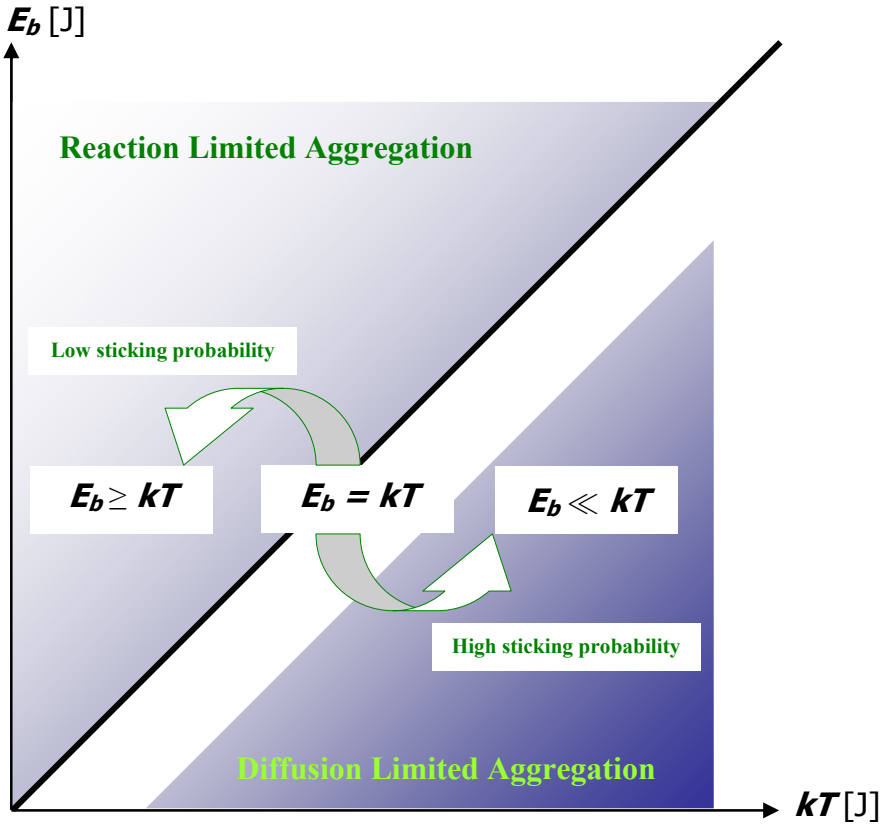

Figure 2.3. Regime map for sticking probability, $\gamma \simeq e^{-E_b / k_b T}$.

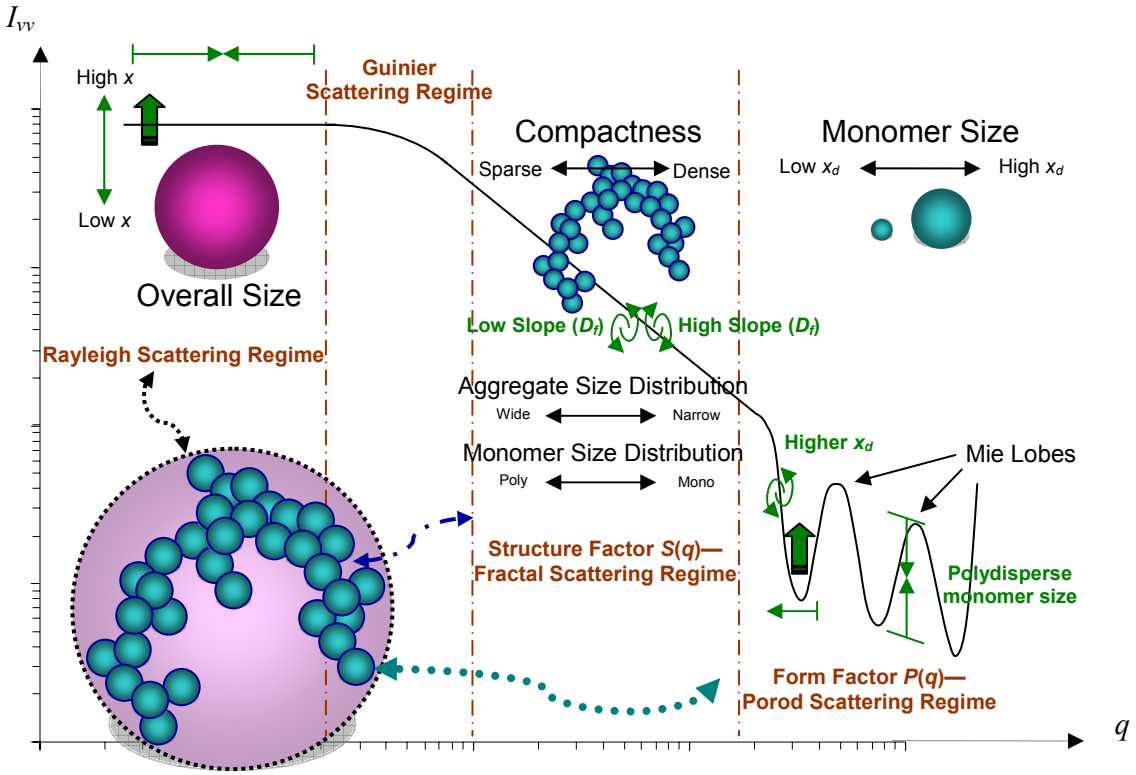

Figure 2.4. Scattered intensity regimes for fractal aggregates.

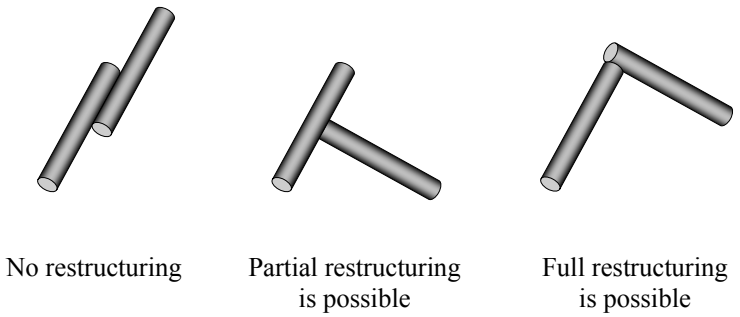

Figure 2.5. Possible sticking configurations for cylindrical particles in a *two-dimensional* medium (e.g., water-air interface) [92]: (p. 7454).

CHAPTER 3

OUTLINE OF EXPERIMENTAL SYSTEM

3.1. INTRODUCTION

The light scattering experiments were carried out using the experimental system designed and set up in the Radiative Transfer Laboratory at the University of Kentucky. A photograph of the optical system is given in Figure 3.1. The design was first proposed as detailed in [69, 142] and later modified as outlined in [143-145]. The EPLS experimental setup used in this study is similar to that was used for elliptically polarized light scattering measurements given in [145], although there are certain modifications performed for the EPLS measurements as can be seen from the discussions below. Further modifications were also made on the setup to perform measurements of vertically polarized incident and detected light (I_{vv}). Over the years, significant information has been amassed on the use of the elliptically polarized and the vertically polarized incident and detected light setups for characterization of various irregularly shaped particles. The reader is referred to [146] for an exhaustive list of these studies.

3.2. DETAILS OF THE EXPERIMENTAL SETUP

Two different experimental setups were used in this study by modifying the configuration of optical components of the original system. The original setup based on elliptically polarized light scattering (EPLS) uses six different combinations of retarder and polarizer angles itself. The second setup based on the measurement of vertically polarized incident and detected light (I_{vv}), on the other hand, is the most commonly encountered system in the literature and referred to as the small angle static light scattering technique.

3.2.1. Elliptically Polarized Light Scattering (EPLS) Setup

Optical components in both the incident and the scattered beam paths are attached to a dovetail optical rail (Edmund Scientific), which are used to mount and position the optical components. The components along the incident light path consists of a set of neutral density filters (NDF), an optical modulator (C, chopper), a variable neutral density filter (V-NDF), a beam splitter, a beam stabilizer, a motorized quarter wave plate (Y-QWP, on motorized rotational stage Y), and iris-1 (IR1) as shown in Figure 3.2.a.

The beam stabilizer is used along the incident light path to minimize the wave front fluctuations of the elliptically polarized beam [147]. The beam stabilizer consists of a quarter wave plate (s-QWP) and a motorized polarizer (P1, on motorized rotational stage X), which are used to reduce the effect of laser power drift over time. The orientation of the polarizer P1 is kept constant at $+45^{o}$ during the EPLS experiments. The quarter wave plate component (s-QWP) of the beam stabilizer was not used in this study to conform to the original design and use the coefficient matrix ([*C*]) (see below for description) developed for the existing setup.

The beam splitter placed after the V-NDF divides the beam into two parts. The first part goes to the reference photo multiplier tube (r-PMT, Hamamatsu-R446) in order to record the laser power during the experiments. The reference voltage value is collected by the data acquisition board (Computer Boards Inc. PCIM-DAS-1602/16) and stored on the hard drive of a desktop personal computer. The second part of the beam passes through the optical components along the incident path as mentioned above before finally entering to the sample cell, which is a glass beaker with a height of 76 mm, diameter of 50 mm and the wall thickness of 3 mm. The sample cell contains particles under investigation suspended in a solution.

As shown in Figure 3.2.b, the scattered light beam path consists of iris-2 (IR2), a lens (L1), a quarter wave plate (Z-QWP, on motorized rotational stage Z), a pin-hole (PH), a

polarizer (P2, on motorized rotational stage W), a second lens (L2), a filter (red) and a photomultiplier tube (PMT, Hamamatsu-R446). L1 has a focal length of 125 mm (Newport KBX067) and L2 has a focal length of 38.1 mm (Newport KBX049). The pin-hole (PH) with a 1000 μm diameter helps restrict the field of view of the detector. Signals received by the PMT are first amplified with a lock-in amplifier, then collected by a data acquisition card and stored on the PC.

The dovetail optical rail that the scattered light path optics are mounted on is attached to a rotational stage (RS). The first polarizer (P1) and the first quarter wave plate which are on the incident beam path (Y-QWP); and the second quarter wave plate (Z-QWP) and the second polarizer (P2) which are on the scattered beam path are all mounted on motorized rotational stages. All four optical components and the rotational stage (RS) are controlled by a multi-axis controller (Galil Inc. DMC-1850-ISA) via the PC.

The power of the incident beam is adjusted using both the NDF and V-NDF in order to avoid damage to the detectors. A 20 mW HeNe laser (λ=632 nm) is employed as the light source. The laser is mounted on a two-axis translation stage and a two-axis tilting stage for alignment of the laser beam position and tilt. The difference in refractive index between air and the glass sample cell causes strong reflection of the incident light. The IR1 is placed in front of the sample cell to control the incident beam diameter and to eliminate any back reflection from the sample cell back surface. Both iris openings are cautiously adjusted to keep the stray light out of the plane of incidence.

3.2.2. Small Angle Static Light Scattering Setup

The EPLS setup is modified to perform measurements using a vertically polarized incident and detected light, I_{vv}. This is the most commonly encountered optical configuration in the literature for fractal characterization of aggregates. It uses less number of optical components, and only one set of scattered intensity measurements (as opposed to six in the EPLS setup) is required. By using this configuration, we plan to compare our measurements performed on the aggregates of fine particles with different

geometries to other important findings in the literature. These measurements also serve as a benchmark for fractal description using the EPLS system, since such studies in the literature are scarce except for the ones produced by our "extended" group.

The EPLS setup uses an additional quarter wave plate in the path of both the incident beam (Y-QWP) and the scattered beam (Z-QWP) as described above. Scattering matrix elements (see Chapter 2 for the related theory) that describe the particles suspended in the sample cell are extracted from six sets of measurements over the same scattering angle range, and as such is a more complicated technique than the simple measurement of I_{vv}.

The I_{vv} measurements on the other hand, require only two polarizers (one placed before and the other after the sample cell) with transmission axes of both kept at 90^{o} with respect to the parallel axis of the incident beam (horizontal). In all I_{vv} measurements performed in this study P1 (on motorized rotational stage X) and P2 (on motorized rotational stage W) were used as the two polarizers unless otherwise is stated. The two quarter wave plates used in the EPLS (Y-QWP and Z-QWP) setup were removed, although the QWP of the beam stabilizer situated before the first polarizer was left unchanged in some experiments without causing any noticeable effect [41]: (p. 349). The rest of the setup was identical to that was used in the EPLS technique.

3.3. MEASUREMENT OF SCATTERING MATRIX ELEMENTS USING THE EPLS TECHNIQUE

As discussed in the theory in Section 2.3.3, elements of scattering matrix (S_{ij}) can be used to determine fractal dimension of aggregates of colloidal particles, but also provide other valuable information about the particles in the medium. Recall that the change in Stokes vector [K] of the light due to its interactions in an optical setup is described by

$$[K]_s = [S]_{sys}[K]_i \tag{3.1}$$

and that we are interested in determining the six independent elements (see Chapter 2 for related theory) of the scattering matrix of the colloidal particle suspension in the sample cell, $[S]_{par}$, from the scattering matrix $[S]_{sys}$, which contains in it scattering matrix elements of the optical components as well

$$[S]_{sys} = \left[P_{2,W}\right] \cdot [QWP_Z] \cdot [S]_{par} \cdot [QWP_Y] \cdot \left[P_{1,X}\right] \cdot [QWP_s] \tag{3.2}$$

3.3.1. The Numerical Procedure

The procedure of extracting the desired information through measurements of scattered intensity in the EPLS setup is described in [69], here we highlight some crucial steps. Recall from Chapter 2 that the Stokes vector is a 4×1 column vector, with scattered intensity as the first element. The PMT detector measures only the intensity of the scattered light, therefore we need consider only the first element of the emergent stokes vector $[K]_s$, which is the output intensity I_o [69]: (p. 284).

The expression for I_o contains in it sines and cosines of the orientation angles for the retarders (quarter wave plates) and polarizers (from Eq. 3.2 above), but also the six independent scattering matrix elements of the particle cloud (S_{11}, S_{12}, S_{22}, S_{33}, S_{34}, and S_{44} originating from $[S]_{par}$ in Eq. 3.2). Solution of the six unknown scattering matrix elements requires a set of six equations, which can be provided by six different combinations of retarder and polarizer angles. The system of equations thus obtained can be written as

$$[B]_{6\times1} = [C]_{6\times6} \begin{bmatrix} S_{11} \\ S_{12} \\ S_{22} \\ S_{33} \\ S_{34} \\ S_{44} \end{bmatrix}_{par} \tag{3.3}$$

where [C] contains the coefficients of scattering matrix elements (e.g., trigonometric terms for optical components), and [B] contains the intensity information at all six measurements. The multiplicative function in front of [B] is $(I_i+U_i)/(k^2r^2)$, but neither I_i nor U_i is measured [69]: (p. 285). This hurdle is overcome by the normalization of measured scattered intensity as elaborated below.

The six S_{ij} elements in the above equation are computed for various particle shapes using the AGGLOME code [78] written in FORTRAN, at scattering angles in the range θ=0°-180°. The angles of rotation for the optical components in the setup are set arbitrarily, and the multiplication of $[C][S]_{par}$ is used to determine the intensity vector, [B]. Some *average* value is determined for the S_{ij} matrix by re-evaluating it (solving the matrix equation above) several times (e.g., 50, [69]: (p. 287)), after some variance (e.g., ±3.5% or ±7.5%, [69]: (p. 285)) is introduced in intensities through random number generation libraries. By using the *average* S_{ij} matrix elements this time, an iterative procedure is followed to determine the optimum values of rotation angles for the optical components in the setup so that the *new* S_{ij} matrix is less than 10% in error (in terms of the *norm* of the vector, [69]: (p. 288)) compared to the *average* S_{ij}.

Over the years, through many refinements in experimental and theoretical aspects of the procedure, a new and improved combination of six sets of rotation angles for the optical components is determined. The values that have been used in several applications in this and recent works at the Radiative Transfer Laboratories are tabulated, and available at the Radiative Transfer Laboratory.

3.3.2. How the Raw Data is Processed

Two types of measurements can be performed: continuous or incremental. The data can be compiled by recording intensities continuously (e.g., 10 readings per second) while the rotational stage (RS) is being moved at a low sweeping speed between two pre-determined scattering angles. The data within the same range of scattering angles can also be recorded at certain scattering angles, e.g., equal increments apart, for a pre-determined

duration (e.g., 10 seconds at each discrete angle) and an averaged intensity can be determined. For each scattering angle, the inverse of the coefficient matrix [*C*] is multiplied by the vector comprised of the intensities (continuous or averaged) from the six sets, [*B*]. The resulting vector contains the six independent scattering matrix elements for the suspended particle mixture. The incremental measurements are more reliable, but more tedious and the amount of data to be processed after measurements is immense. The labor is greatly reduced by use of the two FORTRAN algorithms designed to determine average intensities and the extremum at each scattering angle, and to subsequently determine the particle S_{ij} elements by multiplying these matrices with the inverse coefficient matrix [148].

3.4. EXPERIMENTAL PROCEDURE

3.4.1. Calibration of the Setup

Good experimental practices demand the standardization of the measurements from the more elaborate EPLS setup by calibrating it against known results. Proper alignment of the optical components is made certain by performing calibration measurements on the experimental setup using spherical polystyrene latex particles (Duke Scientific) and comparing the S_{ij} elements from measurements against known values from the Lorenz-Mie scattering theory for spherical particles of the same size and optical properties. This was done before each study presented in this dissertation.

Experimental procedure followed in each of the studies in this dissertation is detailed in the related chapters. However, it should be noted that light scattering measurements with both the EPLS technique and the I_{vv} intensity need to be performed with rather dilute samples [67]: (p. 46), where the electromagnetic interaction between particles can be described as independent scattering [27]: (p. 385) (see Chapter 2 for related theory).

3.4.2. Normalization of Experimental Data

All the intensities including the vertically polarized incident and detected light intensity measurements (I_{vv}) and intensities of all six sets of measurements using the EPLS technique reported in this study correspond to the angular scattered intensity measured relative to the intensity read by the reference PMT

$$I_{vv} \equiv I_{rat}(\theta) = \frac{I_{scat}(\theta)}{I_{ref\ PMT}} \tag{3.4}$$

or, following the paths of the scattered and the reference light beams,

$$I_{rat}(\theta) = \frac{I_{laser} C_{laser\ filter} C_{V-NDF} (1 - C_{beam\ splitter}) C_{sys} \sigma_{med} \Phi_{med}(\theta)}{I_{laser} C_{laser\ filter} C_{V-NDF} C_{beam\ splitter} C_{ref\ PMT\ filter}} \tag{3.5}$$

where σ is scattering coefficient and Φ is the phase function of the two-phase medium, i.e., particles in the solution. C constants represent the fraction of intensity transmitted from a particular optical component: filters in front of the laser source, variable neutral density filter, filters in front of the reference beam PMT, and the beam splitter. C_{sys} correspond to fraction transmitted from the rest of the optical components including the fraction of light traveling in the direction of the laser that is transmitted after the beam splitter. This procedure also helps eliminate any changes in scattered intensity readings that may be a result of fluctuations in the laser power *during* the experiment.

The shade of the V-NDF is the most frequently varied filter setting between any two sets of experiments. This is because an optimum shade that would let the highest amount of scattered intensity reach the scattered intensity PMT at the far end, without compromising the PMT itself, is sought during the measurements on each sample. With the use of I_{rat} instead of the actual intensity reading, the user simply sets a suitable shade that corresponds to the maximum allowed intensity for the PMT-card combination (scattered and reference beams), as long as the sets of filters in front of the reference

PMT are kept unchanged. This is an easy yet very effective way to simplify the burden on the operator.

Once a combination of filters used for the *reference PMT* is modified, however, I_{rat} readings in that set of measurements can no longer be directly compared to another. This hurdle has been overcome by simply normalizing I_{rat} with its value at a predetermined scattering angle, θ_{ref} (e.g., at the smallest scarring angle)—usually one that corresponds to the highest intensity value in the scattered intensity profile

$$\frac{I_{rat}(\theta)}{I_{rat}(\theta_{ref})} = \frac{\Phi(\theta)}{\Phi(\theta_{ref})} \tag{3.6}$$

The normalized relative scattering intensities at scattering angle θ for any two sets of measurements are directly comparable, since in this case scattering profiles are only a function of scattering characteristics of the particles that are being analyzed suspended in the solution.

Figure 3.1. Overall view of the experimental setup.

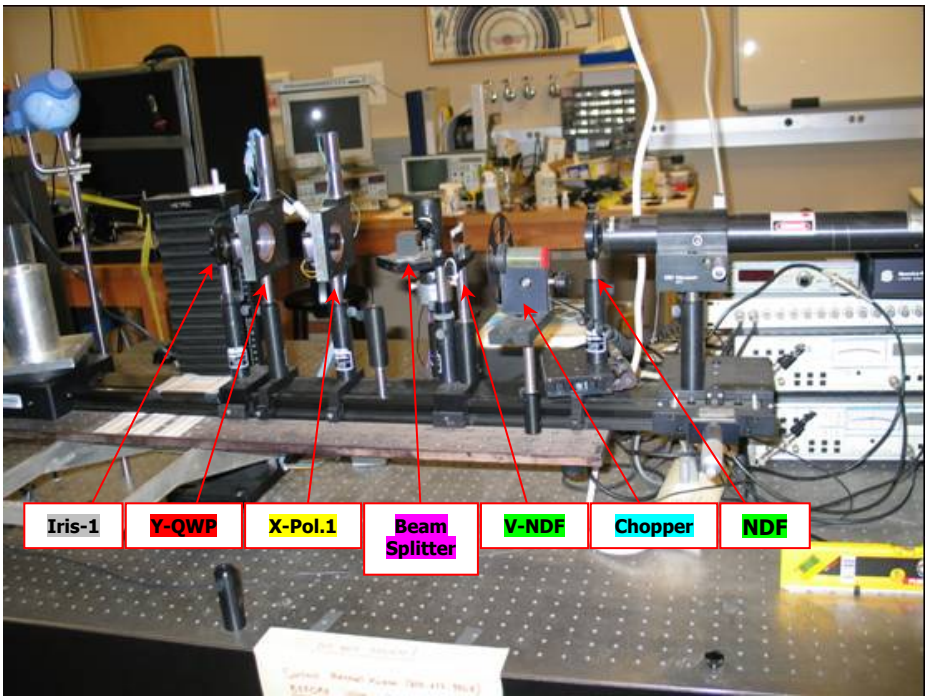

Figure. 3.2.a. Optical components in the *incident* beam path.

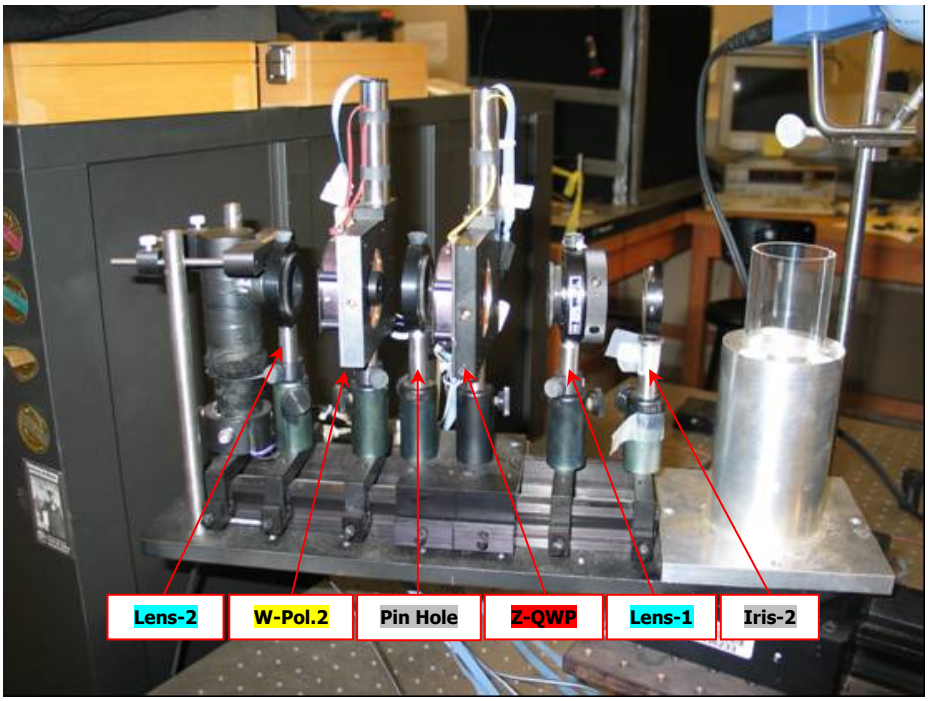

Figure. 3.2.b. Optical components in the *scattered* beam path.

CHAPTER 4

APPLICATION TO AGGREGATES OF WO_3 NANOPARTICLES AND NANOWIRES

4.1. INTRODUCTION

Several solution based processes depend on stable dispersion of nanomaterials in the solvents. Functionalization and dispersion of one-dimensional nanomaterials, such as of single walled nanotubes (SWNT) which are insoluble in all known solvents when untreated (soluble only in presence of a surfactant), have attracted much interest in the literature, although the dispersion of inorganic nanowires remains relatively unexplored [66, 149]. The pursuit of finding new ways to achieve stable dispersions of one-dimensional nanomaterials that possess the properties of SWNTs, but do not require the use of dispersing agents, has led the researchers to investigate materials of new geometrical structures and composition, such as nanowires of metallic oxides. Recent advances in the synthesis of nanowires—cylindrically shaped one-dimensional nanomaterials with high aspect ratios—present unique opportunities as well as challenges in material sciences [53, 150]. Such geometries have potential applications in electronic devices and circuits provided that the nanowires are well characterized and their aggregation patterns in solutions are well understood, which demand observation and control in real time.

Much of the research efforts examining dispersion characteristics of nanowires in polar solvents, however, were singly based on advanced microscopy analyses (such as SEM and TEM) of the resulting structures sampled from dispersion and sediment phases of the suspensions, and their settling times [66]. Although provide useful information and are necessary in a complete characterization study, such techniques have their known shortcomings of being limited to 2-D observations, of having the risk of modifying

aggregate structure during handling, and the potential of orientational biasing [53]. Similarly, turbidity measurements that is based on light transmission measurements provide useful information on how well the nanomaterials are dispersed and on their concentration, but without any reference to the underlying structure of nanomaterials present in the suspension. For example, the size distribution analyses from commercial instruments that use light transmission measurements are generated by assuming any and all clusters as spherical particles of some effective diameter.

Most importantly these techniques lack the thoroughness needed in describing the processes that lead to the observed dispersion and sedimentation behaviors, such as the aggregate morphologies and the aggregation rates. Light scattering techniques, such as the small angle static light scattering and elliptically polarized light scattering (EPLS), have been proven to be powerful in-situ characterization tools that can produce accurate results rapidly, and provide details about the size, size distribution, shape and structure of agglomerates [53, 67-69].

Extensive in-situ aggregation studies that employ light scattering techniques are available in the literature on clusters which are formed by nearly spherical particles. These studies exploit the fact that most of these clusters exhibit fractal behavior in determining their size and structure. However, aggregation behavior of cylindrical particles does not necessarily present the same patterns as the aggregates of spherical or irregular nanoparticles in the same solvents. Experimental and theoretical characterization of aggregates formed by primary particles in shapes other than spheres remains neglected in the literature.

In Chapter 3, the EPLS setup and the small angle static light scattering configuration (using I_{vv}) were described. In the present chapter, based on I_{vv} intensity measurements, we provide a thorough light scattering analysis of the effect of geometry of nanomaterials on aggregation patterns and morphology of resulting aggregates formed in various commonly used polar solvents without the use of dispersants. The findings that are presented in this chapter have also been submitted as a conference paper to RAD-V the

Fifth International Symposium on Radiative Transfer, and was suggested for publication in the Journal of Quantitative Spectroscopy and Radiative Transfer [146]. The nanomaterials made of tungsten trioxide (WO_3) were in the shape of spherical nanoparticles or individual nanowires of various aspect ratios. Aggregation characteristics as a function of geometry, aspect ratio of nanowires, and the change in dispersion stability in time were described in terms of fractal theory. The effect of solvent rheology on degree of aggregation and its change in time will be investigated in Chapter 5.

Two types of WO_3 nanowires used in this chapter were named according to their diameters: "uneven" and "single". Nanowires with large uneven diameters (~200 nm) were ~2 μm in length, whereas single WO_3 nanowires were of varying lengths (4, 6, and 10 μm) but had approximately the same cylindrical diameter (~40 nm). Irregular WO_3 nanoparticles were approximated as spherules of 40 nm diameter.

Vertically polarized incident and scattered light intensities (I_{vv}) were used to determine spatial extent (or radius of gyration, R_g) of the aggregate, the fractal dimension (D_f), and the change in aggregate structure as a function of time. For the single WO_3 nanowire samples of higher aspect ratios where D_f could not directly be inferred from measurements, an analytical method based on spherical primary particle formulations and a quasi-experimental method based on predicting the structure factor ($S(q)$) were used to theoretically determine scattered intensities and D_f. Experimental data on aggregates of these nanowire geometries were interpreted based on the Porod limit analysis, i.e., the scattering behavior of Lorenz-Mie spheres. The shapes of particles are also verified using SEM images.

4.2. EXPERIMENTAL DETAILS

4.2.1. Nanowire Synthesis and Preparation of Nanowire and Nanoparticle Suspensions

Preparation of suspensions of nanoparticles and nanowires (following their synthesis in a hot filament CVD reactor) were performed by the research team of Dr. Sunkara at the University of Louisville. We will highlight some aspects of the nanowire synthesis and preparation of their suspensions important for this chapter, and refer our joint article for further details [53].

Different sets of experimental conditions resulted in different WO_3 nanowire geometries, which we will name as "single", "uneven" and "bundled". Experimental conditions that produce all three nanowire types are summarized in Table 4.1. The first two types of nanowires were produced while the quartz reactor walls were heated by a furnace. The differences in substrate temperature and gas flow rates caused "uneven" diameters in some nanowires or more uniform, "single" nanowires that are circular cylinders in geometry in others, when the furnace heating was employed. Without the furnace heating, the nanowires had the appearance of single nanowires "bundled" together to form diameters of approximately 100 nm with an average wire length of 2 μm. Measurements performed using these samples will be presented in Chapter 5.

Once the nanowires or nanoparticles were combined with the selected solvent, ultrasonication was used to disperse the nanomaterial in the solution. High power ultrasonication using an ultrasonic horn was performed for about 2 minutes followed by the use of a low power ultrasonic bath for about 15 minutes to further disperse the nanowires. Solutions containing single nanowires which had a nominal diameter of about 40 nm were subjected to the high power ultrasonic horn again for different ultrasonication periods to obtain nominal lengths of 4, 6, and 10 μm. Nanowires with large uneven diameters (~200 nm) were ~2 μm in length. WO_3 nanoparticle suspensions were prepared using commercially available nanoparticles of approximately 40 nm diameter (Aldrich, Inc.).

WO_3 nanoparticles and uneven nanowires were suspended in ethanol (ρ=0.789 g/cm^3, n=1.36) both with 1.0 wt% initial concentration before dilution. 4 and 6 μm single WO_3 nanowires suspended in isopropanol (ρ=0.804 g/cm^3, n=1.377) had an initial concentration of 0.1 wt% before dilution. 10 μm single WO_3 nanowires suspended in acetone (ρ=0.791 g/cm^3, n=1.357) were initially at 0.5 wt%.

4.2.2. Light Scattering Setup

As always, the experimental setup for the EPLS technique was tested for proper alignment and configuration of the optical components by comparing experimentally measured scattering matrix (S_{ij}) elements with those from the Lorenz-Mie scattering theory. The setup which was used to measure scattering matrix elements was modified to carry out the vertically polarized incident and detected light (I_{vv}) measurements, as described in detail in Chapter 3. As detailed in Chapter 3, the main difference from the EPLS measurements is that in the I_{vv} measurements the quarter wave plate located after the polarizer in the path of the incident beam, and the quarter wave plate located before the polarizer in the path of the scattered beam were both removed.

4.2.3. In-Situ Characterization Procedure

All measurements were performed while the diluted sample was stirred gently with a small size stirrer set at a low rpm. The paddle type stirrer (IKA model RW11) was immersed in the liquid away from the path of the laser beam, close to the liquid surface. The samples which arrived as suspensions of WO_3 spherical nanoparticles and WO_3 nanowires were diluted to volume fractions in the order of f_v=10^{-6} to ensure independent scattering behavior.

I_{vv} measurements were first performed for suspensions of WO_3 nanoparticles and "uneven" WO_3 nanowires in ethanol. Samples were carefully drawn out of their bottles with a Fisherbrand Finnpipette and transferred into sample cell containing 100 ml of the

solvent used. After gently stirring the suspension, the sample cell was placed into its place in the experimental setup. The same procedure was followed for all other samples. Although the samples were dispersed, or broken to desired length by means of ultrasonication in the synthesis and sample preparation stage, no further ultrasonication was used again on any WO_3 sample before the light scattering measurements.

Measurement of I_{vv} intensity was performed starting from scattering angle θ=3°. Continuous plots are the average of two measurements for all figures given below unless otherwise stated. Continuous measurements were performed at a low sweeping speed with PMT readings of 10 counts/s. The majority of experiments were performed between θ=3°-90° and lasted for 174 seconds, except for the two experiments with ethanol (for spherical nanoparticles and uneven nanowires of 2 μm) where measurements between θ=3°-145° lasted for 284 seconds. All samples except in limited number of cases with ethanol were also subjected to measurements at discrete scattering angles, with 1° increments up to about θ=10° and higher increments thereafter. Measurements on 2 μm uneven nanowires were taken for 15 seconds (150 readings at each point) at discrete scattering angles, and for 10 seconds for other nanowire samples. Similar measurements on "single" WO_3 nanowires of about 40 nm diameter but with higher average lengths of 4, 6, and 10 μm were also performed to investigate the effect of higher aspect ratios.

For the incremental measurements, the readings fluctuated evenly around a mean intensity at each discrete angle. Relative variance at low q, where detected intensities were the highest was negligible—especially on a log-log plot—but increased considerably at the last few data points of very high q. A similar behavior, i.e., higher noise at high q compared to that at lower values of q, was also observed for continuous measurements.

4.3. RESULTS AND DISCUSSION

4.3.1. SEM Analysis of WO_3 Nanoparticles and Nanowires

SEM images showing aggregates of spherical WO_3 nanoparticles and nanowires are given in Figure 4.1. Almost perfectly spherical compact aggregates are formed by irregular WO_3 nanoparticles as seen in Figure 4.1.a. The primary particles forming the compact spherical aggregates seem to have different shapes and some size distribution, however, can safely be approximated as spherules for all general purposes with r_o=20 nm radius. SEM images for "single" WO_3 nanowires of different aspect ratios are given in Figure 4.1.b. WO_3 nanowires, too, have a distribution of wire lengths and diameters, although, the cylindrical diameters are fairly constant and of about 40 nm. Some compact spherical aggregates seen in the figure were probably formed during the commercial production stage. According to our communications with Dr. Sunkara's group, initially, their size was much lower (as obtained powders) and the shapes were not as spherical as shown in Figure 4.1.a, as observed from SEM analyses. This implies the continuation of an aggregation process in which spherical clusters continue to grow (e.g., as irregular nanoparticles or clusters stick on the surface). However, they never tried to re-disperse these aggregates [53].

The size parameter of the individual monomers of WO_3 nanowires are x=10, 20, 30, and 50 (x_{eff}=2.5, 1, 1.2, and 1.4) for 2 (uneven), 4, 6, and 10 μm average length wires, respectively. For nanowire samples as well as for spherical nanoparticles, λ=632 nm and r_o=20 nm were used in the I_{vv} versus qr_o plots to consistently compare all measurements. The question arises on whether the applicability of RGD theory is still justified with such large particle sizes for the determination of fractal dimensions. The first criteria of RGD is satisfied using relative refractive index m of WO_3 in ethanol, $|m-1|=0.5<1$. The second criteria is satisfied for spherical nanoparticles (x=0.2) $nx_{eff}|m-1|=0.14<1$, but not for the longest 10 μm average single nanowires (even with the use of the much smaller effective size parameter, $nx_{eff}|m-1|=0.95\sim1$), or for uneven nanowires ($nx_{eff}|m-1|=1.7$). Nevertheless, in the next section we will show that we can rely on the validity of finding

the D_f from log-log plot of I_{vv} intensity versus q (rather than absolute value of I_{vv}) as discussed in the theory in Chapter 2.

4.3.2. Fractal Behavior of Aggregates of WO_3 Nanoparticles and Nanowires

Figure 4.2.a shows the I_{vv} versus q measurements corresponding to the spherical aggregates of WO_3 nanoparticles and 2 μm uneven WO_3 nanowires, both suspended in ethanol at $f_v=1.1\times10^{-6}$. Experimental plots are the average of two measurements performed for scattering angles between $\theta=3^o$-145^o. Measurements are normalized by the highest attained intensity at $\theta=3^o$ for comparative purposes.

I_{vv} intensity profile for WO_3 nanoparticles in Figure 4.2.a perfectly follows the behavior of fractal aggregates. The constant intensity observed in Rayleigh regime is followed by the transition into the Guinier regime which ends at about $qr_o=0.023$ corresponding to scattering angle $\theta=5^o$. The linear behavior in the fractal scattering region that takes on at this point continues until about $qr_o=0.124$ or $\theta=27^o$, after which point the first ripples (which is partly due to increased noise) reminiscent of the Porod regime is observed. However, polydispersity in the suspension causes the rapid variations in intensity at high qr_o to be smoothed out. There is a wide linear region in this and the rest of the figures in this study (including incremental measurements) that we confine our fractal analysis to regions away from the onset of these ripples in the continuous measurements. $D_f=2.59$ was found from the slope of the fractal scattering region by making a linear fit on data points between $\theta=5^o$-25^o.

A similar behavior is observed for the uneven WO_3 nanowires, opening the door for a fractal description of the nanowire aggregates. The transition from Guinier region to fractal scattering region as well as the onset of Porod region corresponds to about the same scattering angles as for WO_3 nanoparticles. $D_f=2.32$ was found from the slope of the fractal scattering region for uneven WO_3 nanowires by making a linear fit on data points between $\theta=5^o$-35^o.

The fractal dimension observed for the irregular WO_3 nanoparticle sample in Figure 4.2.a is close to the value of 2.5 mentioned in Chapter 2 for the PCA mechanism, but the SEM picture of the sediment phase comprises mainly of compact spherical aggregates (clusters) and very few particles. Our observations via the SEM images have implied an increase in size and sphericity of the compact spherical aggregates in time, as discussed for Figure 4.1.a above, due possibly to sticking of irregular nanoparticles on the cluster surface. A more precise description of the underlying mechanism during which compact spherical aggregates were formed by nanoparticles, however, warrants further research (e.g., by use of well defined spherical nanoparticles as in [93]). The fractal dimension for uneven WO_3 nanowires, on the other hand, is slightly higher than the value of 2.1 realized for reaction limited (slow) CCA mechanism. We provide further analysis which substantiates the slow aggregation rate (in agreement with CCA mechanism) of uneven nanowires by investigating their shelf life in the next section. Nevertheless, it should be noted that the lower slope of uneven nanowire aggregates as opposed to that of irregular nanoparticles is expected since the nanowire aggregates do not form compact spherical structures as seen from the SEM images. The high fractal dimensions observed in the two WO_3 samples given in Figure 4.2.a suggest that a cluster-cluster type of aggregation model could define the aggregation process. Particle-cluster type of aggregation models, such as Witten-Sanders Model which yield D_f~2.5 should also be considered [62]: (p. 61), [89].

A $I_{ref}/I(q)$ versus q^2 plot is given in Figure 4.2.b for aggregates of WO_3 nanoparticles and 2 μm uneven WO_3 nanowires, both in ethanol. Using the Guinier equation given before, the linear fits between θ=6°-14° yield R_g=3 μm and R_g=1.8 μm for nanoparticles and uneven nanowires, respectively. Guinier analysis for R_g determination must, in the most strict sense, be based on data in the region qR_g<1, which makes $I(0)I(q)$=4/3. Nevertheless, it has been shown that data well beyond these limits is acceptable for aggregates of spherical primary particles with high polydispersity [64]: (p. 675), when there is sufficient amount of measurements at low q. Here we have adopted the use of I_{ref} representing the value at $I_{vv}(\theta=3^o)$ to consistently compare results of scattering from all aggregates investigated in this study.

An important concern with Figure 4.2.b is the apparent exponential behavior of the curves at first few q data points. This is related to the PMT saturation at smaller scattering angles encountered in *continuous* measurements, which delays the precipitous decline in $I(q)$ relative to I_{ref}. Guinier analyses based on incremental measurements on the same samples at later times (not shown) were always situated above the continuous measurements (e.g., see Figure 5.4.b in Chapter 5), and have shown linear behaviors extending to the low q values. The plots in Figure 4.2.b should not be considered as the most proper way of determining R_g, but still provide important information as they serve as an indication of relative sizes.

It is also possible to ensure a linear behavior at small q values in $I_{ref}/I(q)$ plot, and even extend it to higher q by using samples with slightly higher particle concentrations (e.g., $f_v \sim 10^{-5}$, not shown) in the light scattering measurements. This will result in higher scattered intensities at side angles (isotropic scattering) due to increased number of particles at the small end of particle size distribution. However, we present here the results corresponding to volume fractions in the order of $f_v \sim 10^{-6}$ for better comparisons between different measurements.

4.3.3. Effect of Extended Shelving on Nanowire Aggregate Structure

An interesting question is if the morphology of aggregates of 2 μm average length nanowires would change if shelved over extended periods of time. Figure 4.3.a presents the results of an attempt to answer this question. Scattered intensity profiles for uneven WO_3 nanowire aggregates of 2 μm average length nanowires at two different volume fractions are given in Figure 4.3.a. The lower curve presents I_{vv} versus qr_o measurements that were performed on the same 2 μm WO_3 nanowires diluted to the same volume fraction of $f_v=1.1\times10^{-6}$ after the 1.0 wt% suspension was shelved for about 6 months. The more concentrated sample at $f_v=4.4\times10^{-6}$ (upper curve) was prepared by transferring appropriate amounts from the initial suspension to the $f_v=1.1\times10^{-6}$ sample.

Solid lines correspond to the average of two continuous measurements performed for scattering angles between θ=3°-90°. Experiments between the same scattering angles were repeated by performing the measurements at discrete scattering angles for 15 seconds. Each data point is the average of 150 readings at a certain scattering angle. To find the slope a linear fit was performed on incremental measurement data points between θ=9°-18°, D_f=2.11 was obtained for the f_v=1.1×10^{-6} sample. A linear fit on incremental data points of the f_v=4.4×10^{-6} sample between θ=9°-20°, gave the exact same fractal dimension D_f=2.11.

One feature that is apparent in Figure 4.3.a is that the incremental measurements perfectly follow the trend of the continuous measurement except for a shift in intensity readings to lower values. Incremental measurements for all other samples in this study behaved similarly: overall trends of continuous measurements were followed, albeit at lower intensities. This suggests that the continuous measurements are tainted with the effect of higher intensities incident on the PMT at a preceding measurement. In fact, although the overall behavior is somewhat changed, D_f=2.32 is obtained for a linear fit on the continuous measurement data between θ=10°-18° in Figure 4.3.a for the f_v=1.1×10^{-6} sample. Note that this is exactly the same D_f obtained on the same sample six months ago, although the linear fractal scattering region is now confined to a narrower range. The difference in D_f from incremental and continuous measurements is somewhat higher in this figure than others due to the presence of the pronounced knee region. However, using incremental measurements provide more reliable estimates and should be preferred when available. Therefore, D_f = 2.11 was reported in Table 4.2 for both samples. Continuous measurements, on the other hand, provide a good indication of the onset of different regimes in the scattering profile and will be used as an aid e.g., to determine the linear region where the fractal dimension is determined from.

Figure 4.3.a exhibits some important differences from Figure 4.2.a in the scattering profile of f_v=1.1×10^{-6} sample. The transition from the Guinier to the fractal scattering regime is not as mild in Figure 4.3.a for the 6 month old sample as in Figure 4.2.a. The power law dependency of I_{vv} on q in the fractal scattering regime which corresponds to

the linear region in the I_{vv} versus qr_o plot is confined to a shorter range, and the first Porod ripples appear as early as qr_o=0.094 or θ=20^o.

Despite a similar fractal dimension (from continuous measurements), the difference in scattering profile in Figure 4.3.a demonstrates the existence of a change in aggregate morphology at the end of an extended period of time. These changes are a result of a combination of a cluster-cluster type aggregation of WO_3 nanowires in time, and the restructuring of WO_3 nanowire aggregates due to hydrodynamic shear or even due to van der Waals forces.

A decrease in number of particles in the small end of the aggregate size distribution manifests itself as a decrease in side scattering, hence the slump in I_{vv} in the fractal scattering region. The emergence of a knee region in forward scattering angles shows that the number of larger aggregates is more than that of the smaller aggregates in this sample. This implies the presence of aggregation of smaller particles into larger particles in the time period studied. On the other hand, considering the large R_g of the samples investigated in this study, stirring the diluted suspension, even at a low rpm might have caused the bonds between nanowires to break and the aggregates to restructure.

A similar knee behavior and a shorter fractal scattering region were observed due to shear induced restructuring of fractal aggregates formed by monodisperse spherical primary particles in [151]: (compare Figures 3 and 4) and also in [152]: (p. 277 and Figure 7). Fraunhofer scattering measurements of extremely large particles (in the order of 3-4 mm) also displayed a knee region in [153] (a simple empirical correlation between measurements and theoretical simulations to find actual D_f was proposed, p. 362). As was mentioned above, the WO_3 nanowires have a wide size distribution. The aggregation of smaller nanowires could have contributed to a decrease in aggregate size distribution, hence a rapid transition from Guinier to the fractal scattering region and a higher D_f (see Figure 2.4). The breakage of bonds, on the other hand, might have introduced an opposite effect and contribute to lowering the slope due to coexistence of small and large primary particles in the sample [110]: (e.g., the decrease in the *slope*—although is not necessarily

the correct D_f as discussed in [109] related to their Figure 6—for a mixture of 70 nm and 600 nm particles in their Figure 2 compared to higher D_f value for aggregates of 70 nm particles alone).

An increase in the fractal dimension would not necessarily point to the existence of a tendency of WO_3 nanowires to aggregate, but would be an additional proof of the presence of restructuring of the aggregates in the suspension. Note that even if no shearing forces to complicate the structure were present, restructuring may still occur due to van der Waals attraction between aggregate branches. R_g, on the other hand, is an indication to the emergence of larger particles formed by aggregation and should be observed along with any increase in absolute values of forward scattered intensities to follow an aggregation process.

Formation of larger particles by aggregation of WO_3 nanowires was observed by determining the increase in R_g. Using the Guinier equation R_g=3.1 μm was found as shown in Figure 4.3.b from the same data given in Figure 4.3.a. Although there is no change in fractal dimension (continuous measurements), the average aggregate size in the suspension has increased considerably over the period of 6 months.

If the more concentrated sample were in the dependent scattering regime scattered light intensity at side angles would increase even more [70], thus lower the slope in the fractal scattering region. It is obvious that the more concentrated sample still obeys the independent scattering regime and the increase in number of scatterers result in higher intensity through the entire range of scattering angles, yet has the same slope in the fractal scattering region. Simply put, increasing the number of aggregates in the sample (higher f_v) provided a smoother transition between the Guinier and the fractal scattering region due to increased side scattering by smaller aggregates. An even more concentrated sample of $f_v=1.1\times10^{-5}$ prepared in the same manner gave the similar trends (not shown), however with a slightly lower fractal dimension D_f=1.97. The decrease in slope could be blamed on restructuring due to stirring, but is also an indication that volume fractions above $f_v\sim10^{-5}$ should be avoided.

4.3.4. Effect of Nanowire Aspect Ratio on Aggregation

An important parameter in nanowire syntheses is the dimensions of the cylindrical particle. In this section we will investigate the effect of geometry of cylindrical nanowires in terms of their aspect ratios. Figure 4.4 shows I_{vv} versus q measurements performed for "single" WO_3 nanowires of 4, 6, and 10 μm average length between $\theta = 3^o$-90^o. Measurements for 2 μm average length nanowires of Figure 4.2.a are also plotted on the same figure for comparison. 4 and 6 μm WO_3 nanowires were suspended in isopropanol at $f_v=0.6\times10^{-6}$ and $f_v=0.3\times10^{-6}$, respectively. 10 μm WO_3 nanowires were suspended in acetone at $f_v=1.1\times10^{-6}$.

A linear fit performed on incremental data points gave for 4 μm WO_3 nanowires *Slope*=-7.48 between $\theta=7^o$-10^o, for 6 μm WO_3 nanowires *Slope*=-6.63 between $\theta=6^o$-9^o, and for 10 μm WO_3 nanowires *Slope*=-6.28 between $\theta=5^o$-8^o. Continuous measurements gave similar slopes within similar ranges of scattering angles: *Slope*=-7.54, -6.84, and -5.52 (between $\theta=6^o$-10^o, $\theta=6^o$-10^o, and $\theta=5^o$-12^o) for 4, 6, and 10 μm WO_3 nanowires, respectively.

The slopes obtained for WO_3 nanowire aggregates longer than 2 μm are beyond the physical limit of fractal dimension $D_f=3$ which is realized for a sphere. The high slopes in this figure cannot be attributed to surface fractals due to the surface roughness of WO_3 aggregates either, since in that case the scattering exponent with the effect of surface roughness would change between $3<-Slope<4$, and as such the slopes in Figure 4.4 should not be interpreted as fractal dimensions in three-dimensional space.

In the absence of theoretical formulations for cylindrical primary particles and experimental D_f and R_g values, it is difficult to provide a quantitative analysis of aggregation characteristics. We can, however, comment on how the available data should be interpreted based on the Porod limit analysis of the spherical Lorenz-Mie particle

scattering profiles, and present arguments relating to the observations of the experimental profiles.

The higher values of the slopes indicate that measurements for aggregates of 4, 6, and 10 μm average length WO_3 nanowires are indeed beyond the fractal scattering region, and in the Porod regime. The crossover from the Rayleigh scattering to Guinier regime, now overlaps with the non-linear scattering of the primary particles observed for the primary particles in the Porod regime [110]. The main reason for this lies in the high size parameter of individual nanowires, i.e., in the comparable length scales of the primary particles and the wavelength of incident light. In this region, the effect of form factor $P(q)$ dominates I_{vv} especially after first few data points at small q over the structure factor $S(q)$, hence $I_{vv} \propto P(q)$, and the scattering profile is a result of scattering from individual monomers. The linear regions in the scattering profiles in Figure 4.4 where the slopes were obtained can, therefore, be viewed as a feature of the curve before the first Fraunhofer dip in the Porod regime and the vibrations that follow can be attributed to the typical ripples seen in this region.

Polydispersity in the 4 μm suspension causes the minimum I_{vv} observed at about q=2.9 to be a shallow dip, above what would otherwise be as in the case of a solid sphere uniform in size [64]: (p. 653 and Figure 6), [111]: (p. 596 and Figure 1). The locations of the first dips of all three nanowire samples follow the Fraunhofer equation and shift to lower scattering angles with average size as seen in Figure 4.4 (see Chapter 2 for the related theory). The locations of first inflection points on the incremental measurements are at about q=2.9, q=2.4, and q=2.1 for the 4 μm (x=20), 6 μm (x=30) and 10 μm (x=50) nanowires, respectively. Average spherical particle diameters approximated from the Fraunhofer equation for the WO_3 nanowires of 4, 6, and 10 μm average length based on the location of the first dips are D=3.7, 4.4, and 4.9 μm, although use of these values as the size of primary particles needs further justification.

The depth of the first dip is also a consequence of the size parameter of the individual monomers, which smoothes out the first sharp dip with higher x resulting in a shallower

first dip in the intensity profile, and a lower slope as primary particle increases [68]: (see their Figure 6). The scattered intensity observed for the 6 μm WO_3 nanowires at the first dip is indeed above that for the 4 μm WO_3 nanowires. However, for the 10 μm WO_3 nanowires the scattered intensity at the first dip is not higher than that of the 6 μm sample contrary to what was expected.

This deviation from the expected theoretical behavior of Lorenz-Mie spheres could be attributed to increased intensity at the Fraunhofer dip due in part to the presence of large nanowires in the 4 and 6 μm WO_3 nanowire suspensions. Recall that 4 and 6 μm nanowire samples were prepared by high power ultrasonication of 10 μm samples, thus the presence of unbroken wires longer than the average nanowire length might have increased their respective intensities at the Fraunhofer dip. The polydispersity that was observed from the SEM analysis for shorter WO_3 nanowire samples should be present to a lesser extent in the 10 μm WO_3 sample.

Another important observation in Figure 4.4 is that the high frequency variations at high q is more pronounced for 10 μm average length WO_3 nanowires, also in line with the predictions of Lorenz-Mie scattering theory for high size parameter spheres. Rapid variations of the scattered intensities at high q for the 4 and 6 μm nanowire samples, on the other hand, are smoothed out by polydispersity and the intensities fare at about a constant value. In fact, the Porod ripples for both nanowire samples are of the same order of magnitude, but confined to a narrower band and at a higher intensity value than that for the 10 μm nanowires. Had there been a monodisperse suspension of 4 and 6 μm nanowires the scattered intensity would continue to diminish with q following the familiar Lorenz-Mie ripple structure as the 10 μm sample did [154]: (p. 147, Figure 1.b). The effect of an increase in size parameter of primary particles was a decrease in D_f in [110], who used the explanation that a dilution of large particles in a web of smaller particles caused the bulging in scattering profile at high q end of the fractal scattering region (i.e., near Porod region). However, our explanation which is based on the effect of a change in size parameter on the scattering profiles of Lorenz-Mie spheres gives a

similar, yet more fundamental answer in the *Porod* regime. Further experimental and theoretical analyses are required including the use of exact solutions for infinite cylinders to verify these comments which are chiefly based on scattering behavior of Lorenz-Mie spheres. A summary of observations on the measurements is tabulated in Table 4.2.

4.3.5. Theoretical Determination of Aggregate Structure for High Aspect Ratio Nanowires

It was observed in Figure 4.4 that for WO_3 nanowire samples of high aspect ratios D_f cannot directly be inferred from measurements. We provide analytical and quasi-experimental methods based on spherical primary particle formulations to determine I_{vv} and the D_f and discuss the reliability of these methods in this section. In Figure 4.4 theoretical values of scattered intensity is fitted on incremental I_{vv} measurements of 4, 6, and 10 μm single WO_3 nanowires using Chen and Teixeira formulation [116], but incorporating a Gaussian size distribution into the form factor ($P(q)$) as suggested by [119], such that $I_{vv}(q) \propto S(q)\overline{P(q)}$. As we have mentioned above, the scattering profiles have migrated into the Porod regime due to the comparable length scales of single WO_3 nanowires and the wavelength of incident light used in the measurements. Average form factor $\overline{P(q)}$ curves alone can be used in this regime to predict the scattered intensity I_{vv}, although we have observed a minor improvement with the inclusion of the structure factor $S(q)$.

Normalized intensities at each q are determined by evaluating the resulting integral equation for $P(q)$ (from Eq. (2.34) and Eq. (2.37) in Chapter 2) by iteratively changing Gaussian probability distribution function parameters and the lower and upper limits of integration for particle diameters. The parameters that minimize the square root of the mean of squared deviations between the predicted and incremental normalized intensities *relative* to the incremental measurements (to take into account the exponential decrease in the order of magnitude of experimental I_{vv} with q) were determined as best fit parameters. Two or three times the nominal wire length gave satisfactory results as the upper limit of integration which was also observed by [119]. The lower limit was allowed

to change only for values very close to zero, and iterations for D_o were concentrated around the particle diameters approximated from the Fraunhofer equation. Rather than trying to fit $I_{vv}(q)/I_{vv}(q_{\min})$ to all available incremental intensity measurements, most of the incremental readings that correspond to high q values with high experimental noise were excluded (especially for the highly polydisperse 4 and 6 μm nanowires) in the curve fitting process. This decreased the overall deviation, and a higher agreement with the measurements was obtained. The best fit parameters are tabulated in Table 4.3.

Introduction of a size distribution function is necessary for the suspensions studied, but the Gaussian distribution seems to have little success in predicting scattered intensity at higher q especially for the 4 and 6 μm nanowires—perhaps due to mono-modal size distribution inherently assumed in the present use of Gaussian probability distribution function, which fails to represent the wide size distribution caused by the ultrasonication. Prediction on the I_{vv} intensity profile for the 10 μm WO_3 nanoparticles, on the other hand, seems to fit the experimental data points to a better degree. This may be thought to be related to the fact that available data cease to exist at high q (see Figure 4.6.a for a complete range of measurements), because the incremental intensity readings are simply below the measurement sensitivity of the experimental setup. But the incremental measurements has a similar trend with what is predicted from the theory and measurements being below measurement sensitivity is quite expected—for the 10 μm nanowires which have a relatively narrow size distribution, the continual decrease in predicted scattered intensity with q is in line with the familiar Lorenz-Mie ripple behavior. Because of the pronounced tail of small particles in the size distribution, 4 and 6 μm nanowires on the other hand, have a constant, rather than a decreasing intensity profile at high q.

The original method suggested by Hasmy et al. [119], which is illustrated next, employs a quasi-experimental method to approximate the scattered intensity for particles of large size parameters with only the form factor (recall, $I_{vv} \propto P(q)$ in the Porod regime). Using a similar iterative method as described above, normalized average form factors

$\overline{P(q)}/\overline{P(q_{\min})}$ at each q corresponding to the incremental measurements were computed for the aggregates of 4, 6, and 10 μm WO_3 nanowires. Predicted scattered intensity profiles are similar in nature to those of the modified Chen and Teixeira method used above, which also included the analytical structure factor formulation to represent I_{vv}. The best fit parameters are presented in Table 4.4. Using the average form factor in $\overline{S(q)} \propto I_{vv}(q)/\overline{P(q)}$, the normalized $\overline{S(q)}/\overline{S(q_{\max})}$ versus q was plotted in Figure 4.5, such that $\overline{S(q)}/\overline{S(q_{\max})} \rightarrow 1$ for $q_{max} \rightarrow \infty$. The slope determined in the linear portion of $\overline{S(q)}/\overline{S(q_{\max})}$ versus q plot gives, as usual, the fractal dimension D_f of the aggregates of WO_3 for the 4, 6, and 10 μm (Day-1) nanowires.

Unlike an initial wide dip in the $S(q)$ against q plot and the following dampened harmonic behavior for monodisperse spheres observed in [119], the oscillations for the pseudo-experimental structure factor $S(q)$ of polydisperse WO_3 nanowires in this study intensify vigorously after the first similar dip. Rather than trying to fit $\overline{P(q)}/\overline{P(q_{\min})}$ to all available incremental intensity measurements, most of the incremental readings that correspond to after the first wide dip were excluded in the curve fitting process. This decreased the total deviation, and a higher agreement with the measurements was obtained.

4.3.6. Change in Aggregate Morphology of Nanoparticles and Long Nanowires with Time

Measurements were also performed to detect possible changes in aggregate morphology with time. Figure 4.6 shows I_{vv} versus q measurements between $\theta = 3^o$-90^o, carried out in a span of six days for a second batch of spherical aggregates of irregular WO_3 nanoparticles and aggregates of 10 μm average length single WO_3 nanowires, both suspended in acetone at $f_v = 1.1 \times 10^{-6}$. Initial concentrations of both samples were 0.5 wt% in this case. Measurements for both types of geometries on the same day are presented in the same figure for better comparison. Measurement for WO_3 nanowires on Day-1 is carried to Figure 4.6.a from Figure 4.4. Continuous measurement plot in Figure 4.6.c is

from one set of measurements, and the only such curve in this chapter. Underflows in I_{vv} profile for continuous WO_3 nanowire measurement in Figure 4.6.c were remedied by converting out of range readings to non-zero values of $I/I_{ref} \sim 10^{-6}$ to improve visual appearance.

A gradual increase in fractal dimension from 2.52 (between θ=7°-20°) to 2.58 (between θ=8°-25°) and 2.62 (between θ=8°-20°) followed by a decrease to 2.57 (between θ=7°-17°) is observed for incremental measurements on spherical aggregates of WO_3 nanoparticles on Days 1, 2, 3 and 6, respectively. A similar behavior was observed in Figure 4.6 for the slopes of WO_3 10 μm nanowire aggregates in acetone. The increase in slope before the first Fraunhofer dip from -6.28 (between θ=5°-8°) to -7.94 (between θ=6°-8°) is followed by a decrease to -6.75 (between θ=6°-10°) and -5.23 (between θ=7°-8°) for incremental measurements on Days 1, 2, 3, and 6, respectively, and are tabulated in Table 4.2. As discussed above, slopes larger than 3 should not be interpreted as fractal dimensions in three-dimensional space, but are rather a consequence of comparable length scales of the primary particles and the incident wavelength of light.

Figure 4.6 also shows the theoretical average scattered intensities for 10 μm WO_3 nanowires for the six days the measurements were performed on, based on *modified* Chen and Teixeira formulation mentioned above [116, 119]. Predicted intensities follow the normalized experimental scattered intensity profiles to a good extent well after the first Fraunhofer dip (until about q=3.3, or θ=14°), after which point discrepancies from the high q variations in incremental scattered intensities are observed. However, computations based on the spherical primary particle formulations were only able to predict approximately the same average spherical primary size of about D_o~3.9 μm, which are also tabulated in Table 4.3. The slight increase in the width σ of the predicted average diameter on Day-6 is also worth noting as it implies a wider size distribution, possibly due to shear from constant mechanical stirring, though a high degree of confidence on the exact values is hard to claim. D_f~1 obtained from the scattered intensity predictions indicates the length scale of the light is considerably smaller than that of the aggregates for all three nanowire lengths as shown in Table 4.3, such that it

can resolve the length scale of individual monomers, but is not able to discern the overall structure of the aggregates in the suspensions.

Structure factor computed from the Hasmy et al. method for 10 μm nanowire aggregates during the measurement span of six days is given in Figure 4.7. Further experimental and theoretical investigations are required before the D_f values found can be used with confidence.

Figure 4.8 provides an easy comparison of the measurements on 10 μm nanowires at forward scattering angles. A mild hike in forward scattered intensity in the form of a knee region is observed for the measurements on Day-2 and Day-3, similar to those observed in the uneven 2 μm samples mentioned above. Despite the changes in slopes before the first Fraunhofer dip, the intensity profiles for 10 μm nanowires on all four days of measurements are quite similar. The location of the first Fraunhofer dip for all four measurements is also at about the same q. The knee region that appears in some of the measurements is an indication to the likelihood of some increase in overall size due to aggregation in first three days. This observed in spite of the negligible difference seen in forward scattering intensities for all four measurements (i.e., no Tyndall effect is observed).

We believe these observations demonstrate the presence of a low level of aggregation of the 10 μm nanowires, along with a change in fractal geometries due possibly to restructuring induced by stirring of the suspensions. Considering the increase in the length scale for the 10 μm nanowires compared to those that are shorter, shear forces created by the constant stirring of the suspensions may cause breakage of the aggregates or even of individual primary particles themselves. Since the slope before the first Fraunhofer dip is inversely related to the size of the primary particle, the abrupt increase in slope on Day-2 can be viewed as an indication of a decrease in average primary particle size due to breakage (recall the discussions above and Lorenz-Mie analysis of [68] based on size parameters given in Chapter 2). However, a competing effect of aggregation is also present. The steady decrease in slope that follows Day-2, on Day-3

and Day-6 is then due to larger structures being formed in the primary particle length scale, which can be viewed as if the new aggregated structures acting as if they are the new primary particles, thus increasing the average aggregate size in the sample.

The increase in the small size tail of the particle distribution due to breakage manifests itself as additional incremental measurement readings at high q in Figure 4.6.d for Day-6. This is a stark difference from what the scattered intensity profile for 10 μm nanowires looked like at the beginning in Figure 4.6.a. The scattered intensity profile in Figure 4.6.d at high q now resembles more to those of 4 and 6 μm nanowires in Figure 4.4, with the rapid variations smoothed out and at a somewhat constant intensity value due to increased polydispersity.

Aggregates of WO_3 nanowires of high aspect ratios (single nanowires with average lengths that are longer than 2 μm) do not lend themselves to experimental determination of the radius of gyration, either. Radius of gyration of the spherical aggregates of the WO_3 nanoparticles, on the other hand, remained almost unchanged during the same period. Figure 4.9 gives R_g=3.7 μm obtained on Day-1 from the Guinier analysis of the incremental scattered intensity measurements. Incremental measurements (not shown) for Day-2, 3, and 6 gave R_g=3.9, 3.8 and 3.7 μm, respectively. Continuous measurements for the same measurements are also plotted in the figure for comparison.

4.4. SUMMARY

In this chapter we discussed experimental and theoretical characterization results for WO_3 nanoparticles and nanowires of different aspect ratios. We have shown quantitatively that the different primary particle geometries result in different aggregation characteristics with WO_3 nanoparticles and nanowires. Aggregates of WO_3 nanoparticles were more compact and almost spherical in shape (D_f~2.6), whereas for the 2 μm WO_3 nanowires of ~200 nm diameter their aggregates were more open, although still with a considerably high fractal dimension (D_f~2.1) which corresponds to the structures that

result from the reaction limited (slow) cluster-cluster aggregation mechanisms reported in the literature for spherical primary particles. Similarly, comparing the extent of the aggregates formed by nanoparticles and 2 μm nanowires, the initial R_g were considerably larger for nanoparticles (3-4 μm) than for the 2 μm nanowires (1.8 μm).

An interesting observation made on the 2 μm uneven nanowires was that their aggregates increased in size when stored for an extended period of about six months to R_g=3.1, although their overall fractal geometry remained unchanged. The increase in R_g as well as the high D_f give us the clue that a cluster-cluster type of aggregation model could define the aggregation pattern of 2 μm uneven WO_3 nanowires. However, the shear forces created by stirring of the samples complicates the aggregate structure, as the high D_f could be attributed to an increase in D_f due to restructuring of the aggregates formed by a reaction limited cluster-cluster aggregation.

In a much shorter time scale, aggregates of high aspect ratio WO_3 nanowires of 10 μm length and 40 nm diameter did not aggregate appreciably and did not change their fractal structure in about six days of measurements. Although measurements on aggregates of 10 μm WO_3 nanowires did not allow experimental determination of R_g and D_f, experimental profiles revealed a low level of aggregation in the same period of time.

For nanowires longer than 2 μm, migration of the Porod scattering regime toward the forward scattering angles was observed which results from the comparable length scales of primary particles and the wavelength of light used (i.e., high x). We have resorted to the use of an analytical and a quasi-experimental model, both of which were based on the formulations for spherical primary particles, to determine the fractal dimensions of aggregates of 4, 6, and 10 μm nanowires. Numerical results from the quasi-experimental model indicate a decreasing trend in D_f with average wire length, with $D_f \sim$ 1.87, 1.70, and 1.41 obtained for aggregates of 4, 6, and 10 μm WO_3 nanowires, respectively.

This suggests that as the wire length decreases the tendency of WO_3 nanowires to create entangled, more closed aggregates increases, with 2 μm nanowires showing the highest

degree of compactness (D_f~2.1). It should be emphasized, however, that the polydispersity in size distribution was higher in the shorter wire length samples (due to the ultrasonication used to prepare these samples), and is an important factor in increasing D_f values (wide size distribution decreases D_f).

A diffusion limited cluster-cluster aggregation model could successfully predict the aggregation mechanism for 4 and 6 μm nanowires, whereas the longest nanowires of 10 μm average length has a small tendency to aggregate and arrange themselves tip-to-toe found in polarizable clusters [131].

The results from theoretical models developed for spherical primary particles should be used cautiously, since e.g., any comments for Porod regime would chiefly be based on scattering behavior of Lorenz-Mie spheres. Size distribution functions that could better represent the nanowire aggregates than the Gaussian probability distribution function should be identified, especially for such samples as the 4 and 6 μm nanowires with high polydispersity. Most importantly, a more accurate representation of the form factor $P(q)$ for cylindrical primary particles should be developed, using the exact solutions for infinite cylinders. Experimental measurements could also be repeated with a light source of higher wavelength comparable to the nanowire lengths to infer the D_f and R_g experimentally.

Table 4.1. Synthesis conditions and resulting dimensions of WO_3 nanoparticles and nanowires.

Sample	Solvent	Synthesis Conditions	Nominal Diameter, nm
2 μm nanowires ("uneven" diameter)	Ethanol	T_{sub}=900°C 1.5 sccm O_2 100 sccm Ar T_{fil}=1690°C	200
4, 6, and 10 μm nanowires ("single")	Acetone Isopropanol	T_{sub}=800°C 0.4 sccm air 100 sccmAr T_{fil}=1690°C	40
2 μm nanowires ("bundled")	1-Methoxy 2-Propanol N,N-Dimethylformamide Water	T_{sub}=600°C 11 sccm air T_{fil}=1690°C	100
Nanoparticle	Ethanol	Commercial Powder	40

Table 4.2. Fractal properties of aggregates of WO_3 nanoparticles and nanowires ("Single" nanowires of 4, 6, 10 μm average length with ~40 nm diameter, and 2 μm nanowires with ~200 nm "uneven" diameter. *See text).

WO_3 Sample	Solvent	Initial wt%	D_f (or Slope)	R_g, μm
Nanoparticle	Ethanol	1.0	2.59	3
2 μm Nanowire	Ethanol	1.0	2.11*	1.8
2 μm Nanowire (6 mo. later)	Ethanol	1.0	2.11	3.1
4 μm Nanowire	Isopropanol	0.1	-7.48	-
6 μm Nanowire	Isopropanol	0.1	-6.63	-
Nanoparticle Day-1	Acetone	0.5	2.52	3.7
Nanoparticle Day-2	Acetone	0.5	2.58	3.9
Nanoparticle Day-3	Acetone	0.5	2.62	3.8
Nanoparticle Day-6	Acetone	0.5	2.57	3.7
10 μm Nanowire Day-1	Acetone	0.5	-6.28	-
10 μm Nanowire Day-2	Acetone	0.5	-7.94	-
10 μm Nanowire Day-3	Acetone	0.5	-6.75	-
10 μm Nanowire Day-6	Acetone	0.5	-5.23	-

Table 4.3. Parameters for predicted I_{vv} [116] with Gaussian size distribution function [119] for WO_3 nanowires. (*See text: might exclude measurements at high q.)

Sample	D_f	$D_o \pm \sigma$, μm	RMS Dev.	# of Meas. Used*	# of Integ. Segments	Lower Lim. D_{min}, μm	Upper Lim. D_{max}, μm
4 μm	1.01	3.1±0.35	0.441	14 of 22	29	0.03	22
6 μm	1.01	3.1±0.85	0.271	10 of 21	28	0.03	22
10 μm Day-1	1.01	4.0±0.75	0.371	18 of 18	15	0.03	16
10 μm Day-2	1.01	3.8±0.6	0.158	16 of 16	23	0.04	22
10 μm Day-3	1.01	3.9±0.6	0.181	8 of 11	23	0.04	16
10 μm Day-6	1.01	4.0±0.85	0.502	17 of 17	15	0.04	16

Table 4.4. Mean normalized structure factor ($\overline{S(q)}/\overline{S_{\max}}$) parameters for aggregates of WO_3 nanowires [119]. (*See text: might exclude measurements at high q.)

Sample	D_f	$D_o \pm \sigma$, μm	RMS Dev.	# of Meas. Used*	# of Integ. Segments	Lower Lim. D_{min}, μm	Upper Lim. D_{max}, μm
4 μm	1.87	3.3±0.32	0.153	9 of 22	21	0.03	16
6 μm	1.70	3.7±0.65	0.142	8 of 21	23	0.03	22
10 μm Day-1	1.41	4.75±0.77	0.106	10 of 18	12	0.03	16
10 μm Day-2	1.81	4.5±0.45	0.181	10 of 16	17	0.04	22
10 μm Day-3	1.83	4.3±0.55	0.344	8 of 11	12	0.04	22
10 μm Day-6	1.30	4.6±0.9	0.061	9 of 17	17	0.04	22

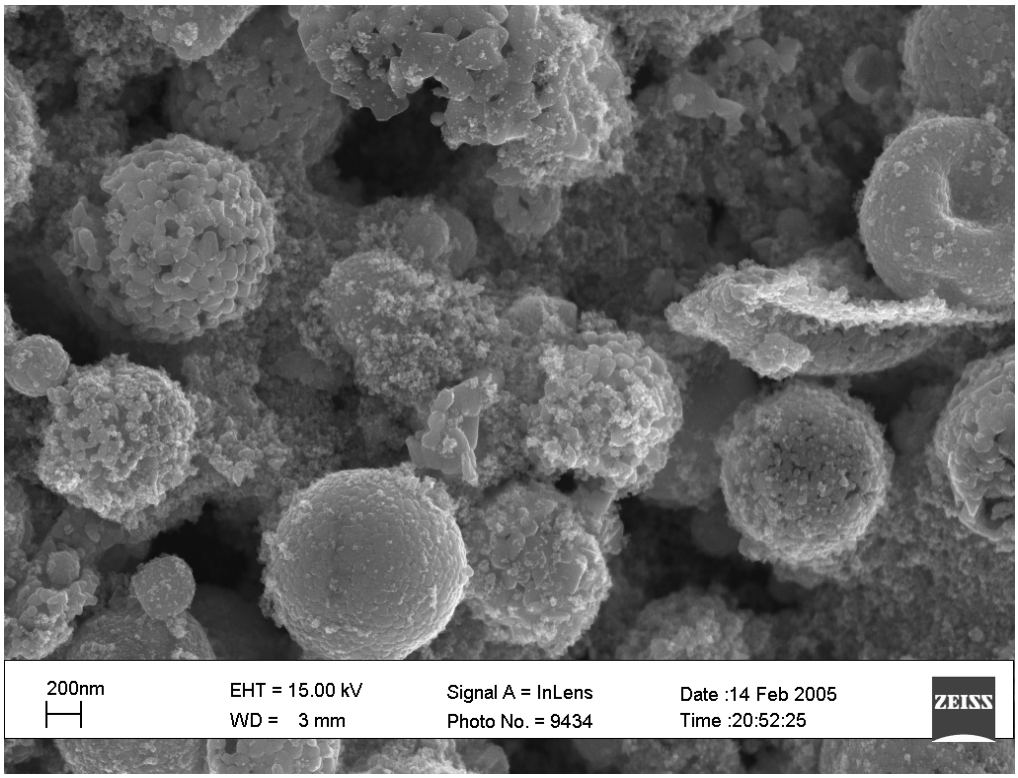

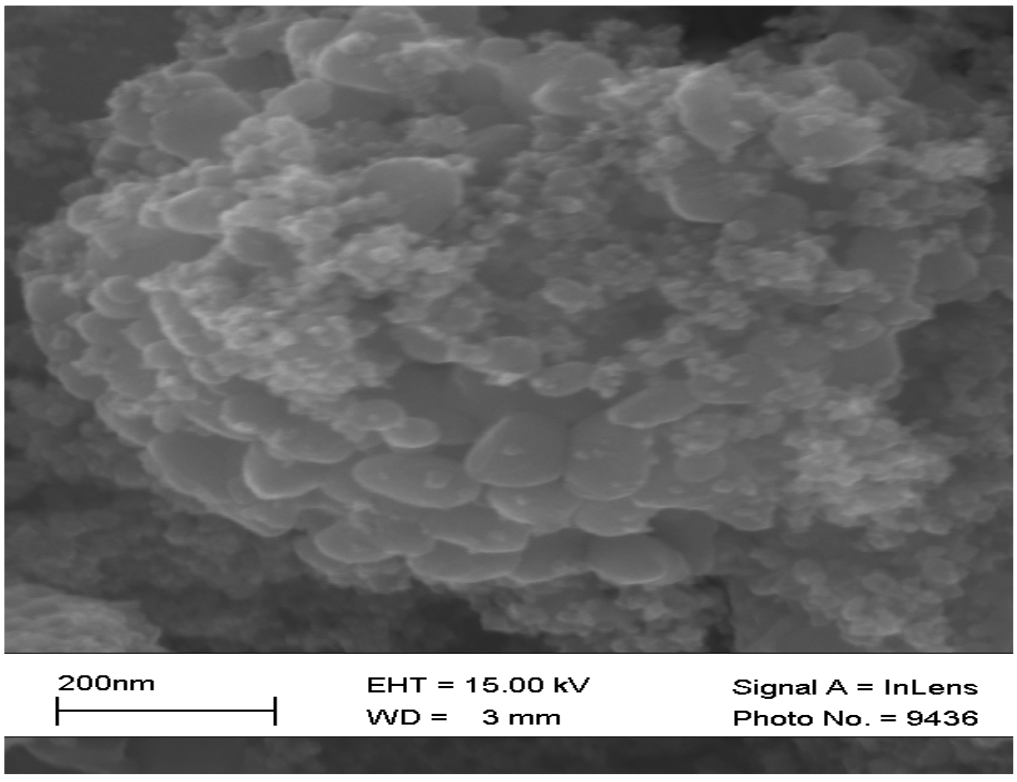

Figure 4.1.a. SEM images of WO_3 spherical nanoparticle aggregates.

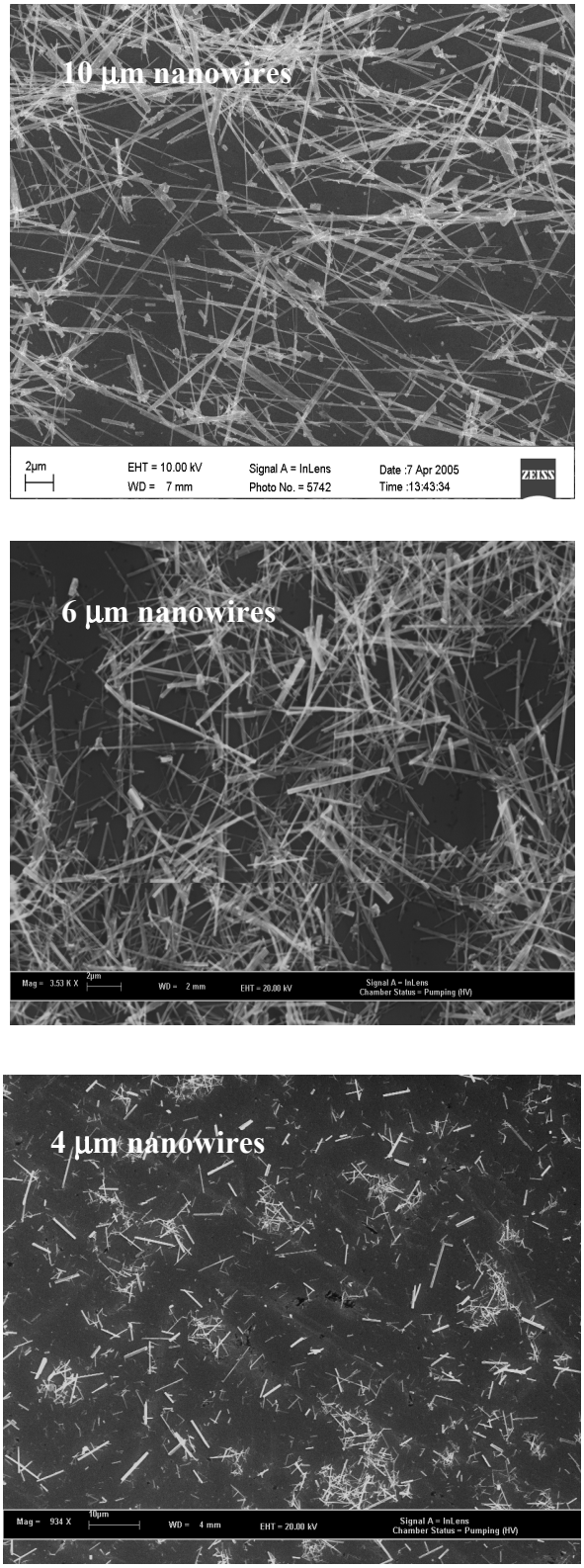

Figure 4.1.b. SEM images of aggregates of "single" WO_3 nanowires after 5 minutes, 20 minutes, and 1 hour of ultrasonication (10, 6, and 4 μm average length, respectively).

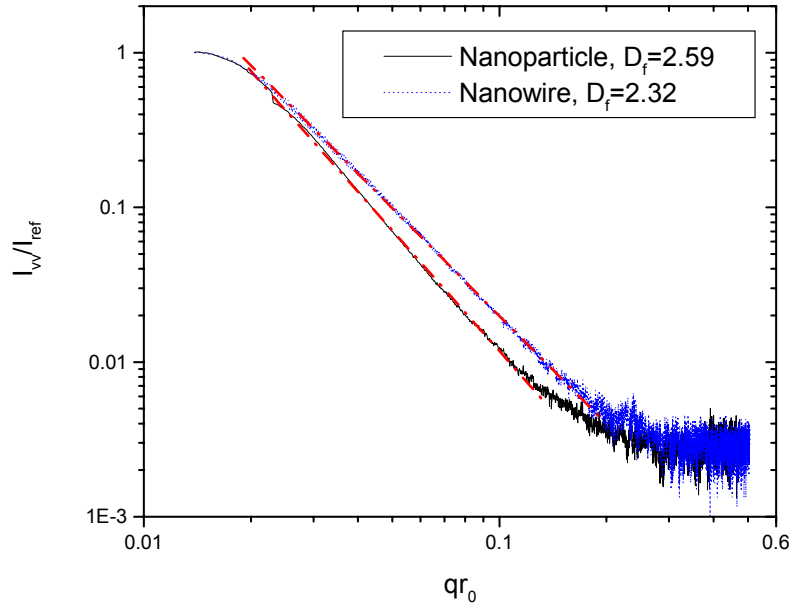

Figure 4.2.a. Determination of fractal dimension using small angle static light scattering for aggregates of WO_3 nanoparticles (lower curve) and nanowires (upper curve, 2 µm average length, "uneven" diameter) in EtOH. Linear fits (dash-dot) are for data points between θ=5°-25°.

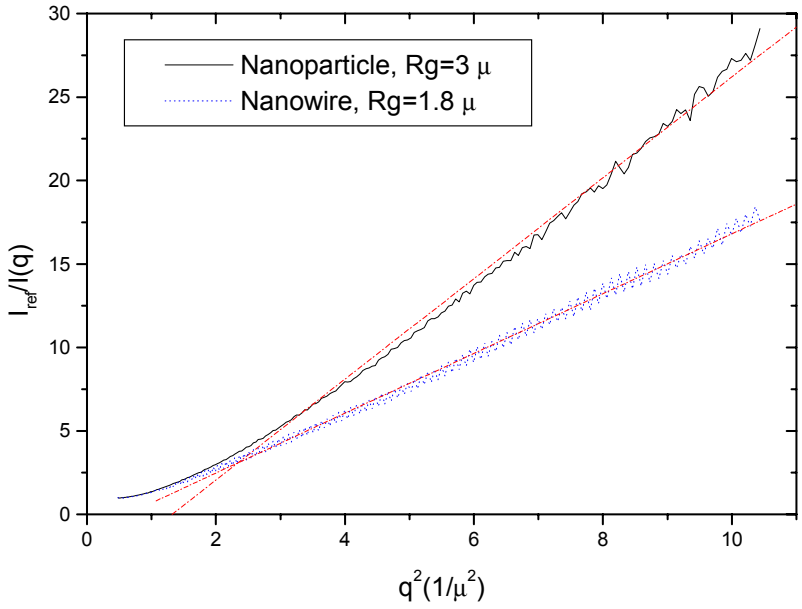

Figure 4.2.b. R_g for aggregates of WO_3 nanoparticles and "uneven" nanowires (2 µm average length) in EtOH. Linear fits (dash-dot) are for data points between θ=6°-14°.

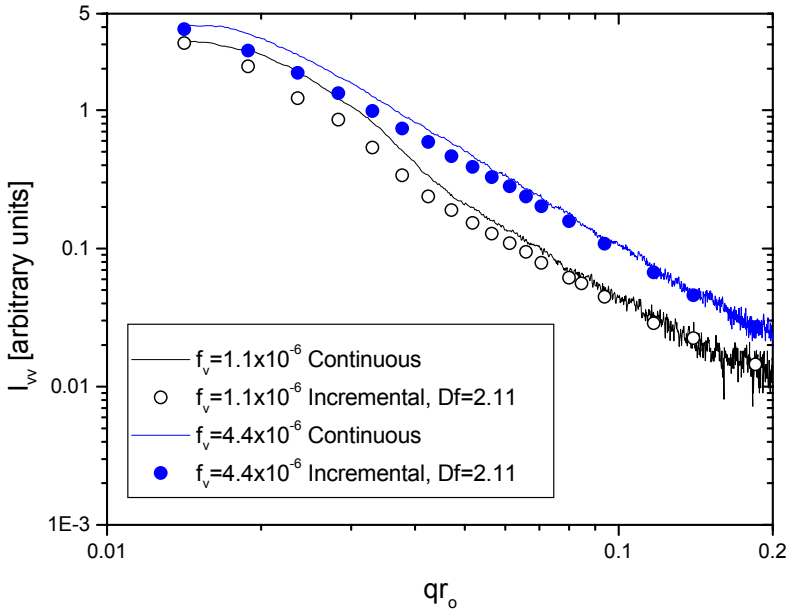

Figure 4.3.a. Determination of fractal dimension using small angle static light scattering for "uneven" WO_3 nanowire aggregates in EtOH shelved for 6 months. Linear fits are for incremental data points between θ=9°-18° (f_v=1.1×10^{-6}) and θ=9°-20° (f_v=4.4×10^{-6}).

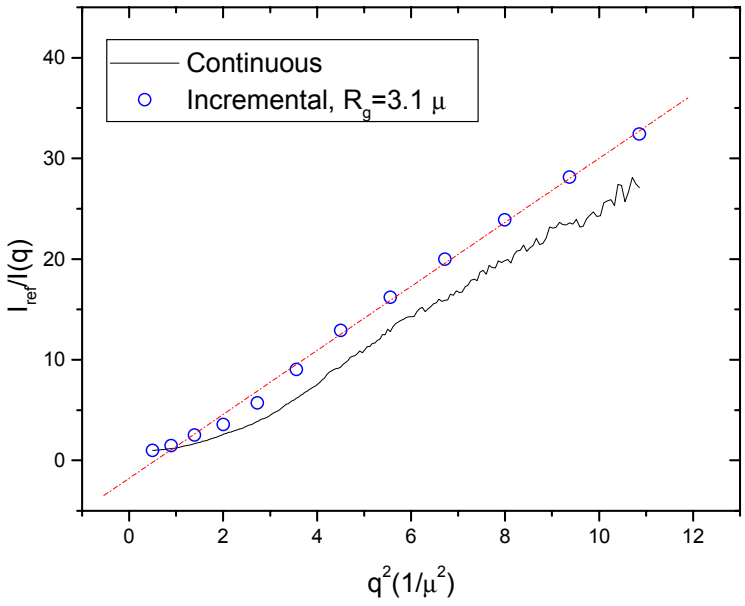

Figure 4.3.b. R_g for aggregates of "uneven" WO_3 nanowire aggregates in EtOH (2 μm average length) shelved for 6 months (f_v=1.1×10^{-6}).

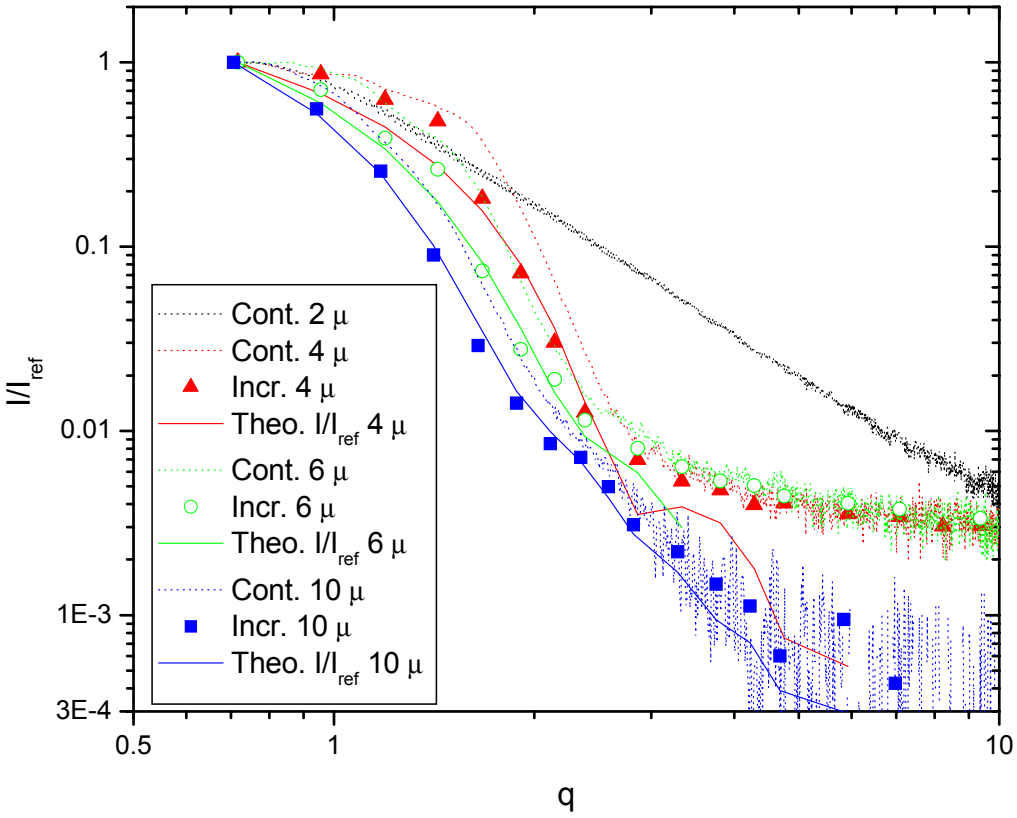

Figure 4.4. Small angle static light scattering measurements for aggregates of 2, 4, 6, and 10 μm WO_3 nanowires. Linear fits (not shown) for incremental data points between θ=7°-10°, θ=6°-9°, and θ=5°-8° give *Slope*=-7.48, *Slope*=-6.63, and *Slope*=-6.28 for 4 μm, 6 μm, and 10 μm nanowires, respectively. Theoretical fits are using modified Chen and Teixeira method [116] with Gaussian size distribution function [119] for individual nanowires.

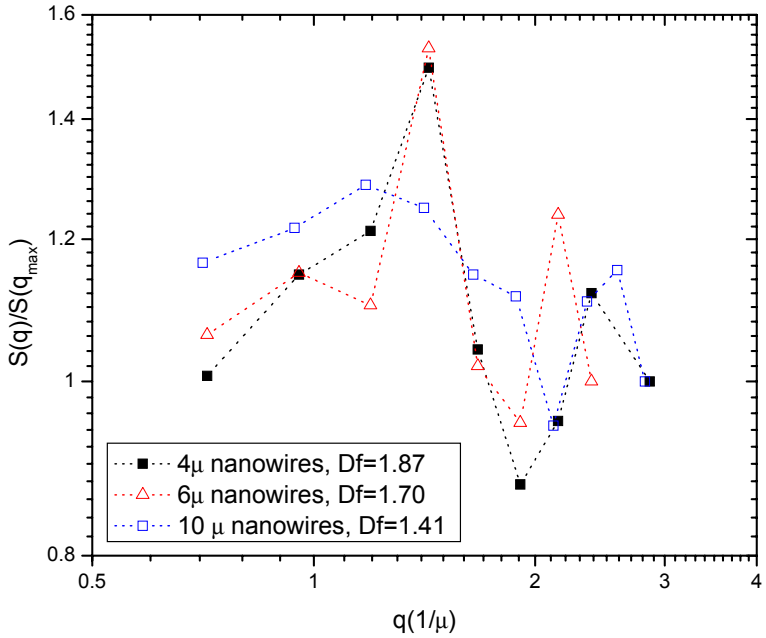

Figure 4.5. Normalized structure factor using quasi-experimental method of Hasmy et al. [119] for aggregates of 4, 6 and 10 μm (Day-1) WO_3 nanowires.

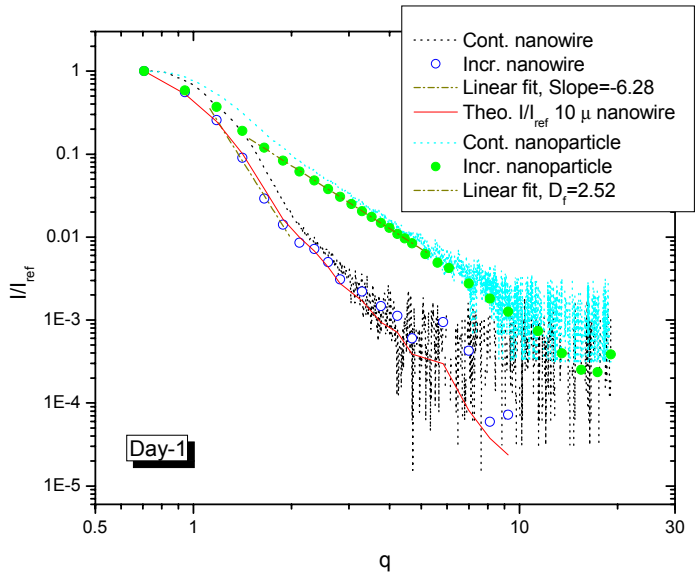

Figure 4.6.a Small angle static light scattering measurements for aggregates of 10 μm WO_3 nanowires and nanoparticles in acetone on Day-1. Linear fits are for incremental data points between θ=5°-8° and θ=7°-20°, for nanowires and nanoparticles, respectively. Theoretical intensity [116] is fitted on incremental I_{vv} measurements of 10 μm WO_3 nanowires using a Gaussian size distribution function [119].

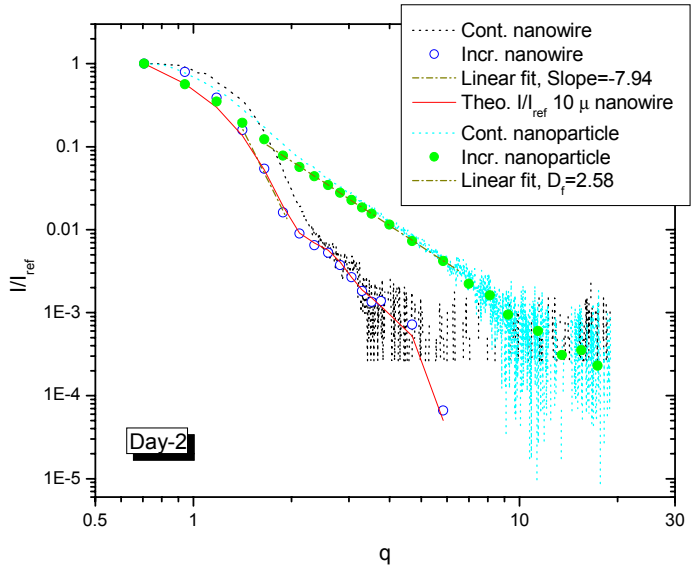

Figure 4.6.b Small angle static light scattering measurements for aggregates of 10 μm WO_3 nanowires and nanoparticles in acetone on Day-2. Linear fits are for incremental data points between θ=6°-8° and θ=8°-25°, for nanowires and nanoparticles, respectively. Theoretical intensity is fitted on incremental I_{vv} measurements of 10 μm WO_3 nanowires [116, 119].

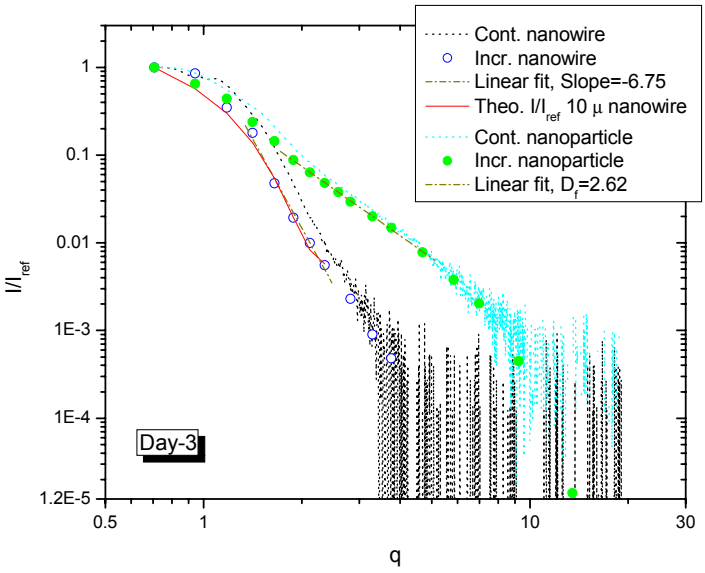

Figure 4.6.c Small angle static light scattering measurements for aggregates of 10 μm WO_3 nanowires and nanoparticles in acetone on Day-3. Linear fits are for incremental data points between θ=6°-10° and θ=8°-20°, for nanowires and nanoparticles, respectively. Theoretical intensity is fitted on incremental I_{vv} measurements of 10 μm WO_3 nanowires [116, 119].

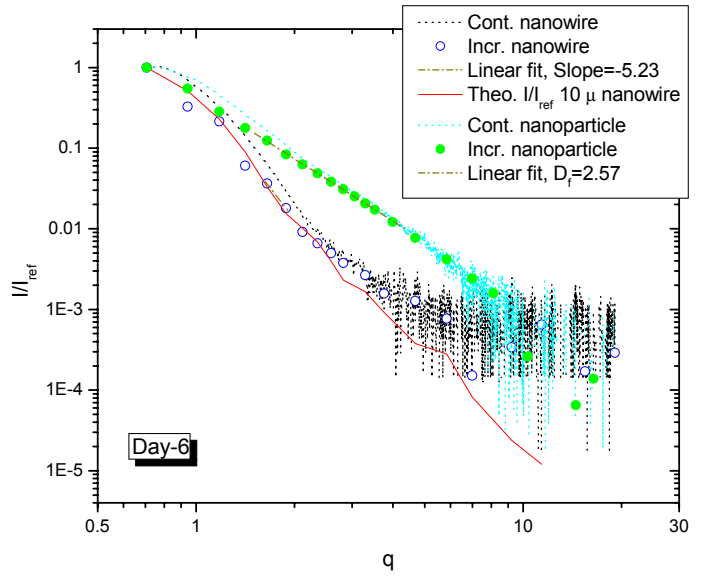

Figure 4.6.d Small angle static light scattering measurements for aggregates of 10 μm WO_3 nanowires and nanoparticles in acetone on Day-6. Linear fits are for incremental data points between θ=7°-8° and θ=7°-17°, for nanowires and nanoparticles, respectively. Theoretical intensity is fitted on incremental I_{vv} measurements of 10 μm WO_3 nanowires [116, 119].

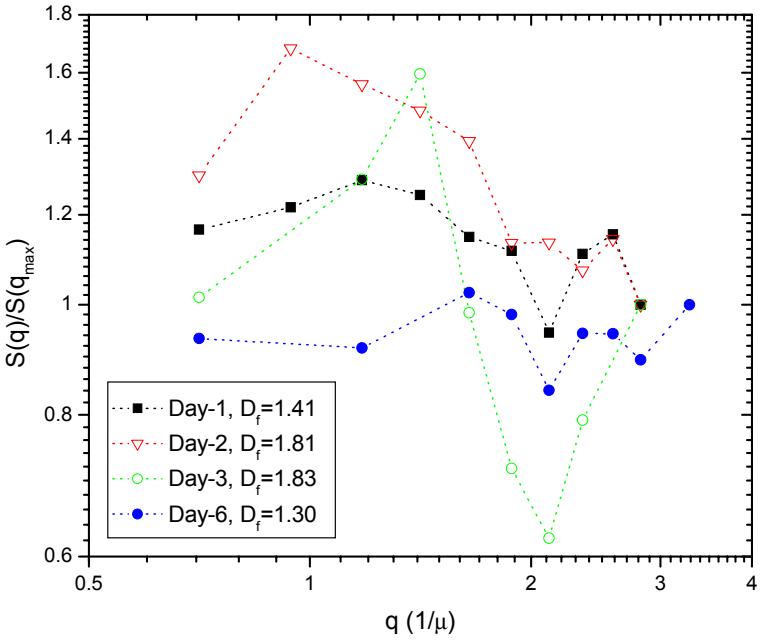

Figure 4.7. Normalized structure factor using quasi-experimental method of Hasmy et al. [119] for aggregates of 10 μm WO_3 nanowires.

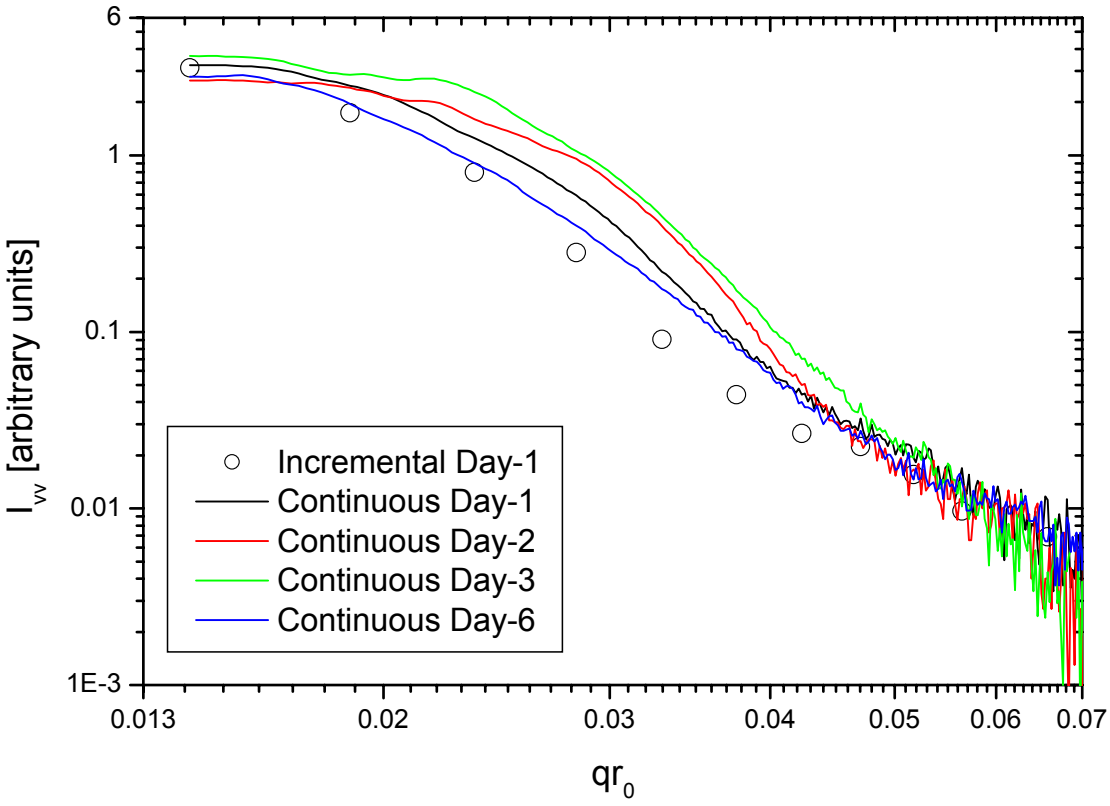

Figure 4.8. Comparison of small angle static light scattering measurements for aggregates of 10 µm WO_3 nanowires in acetone in a span of six days.

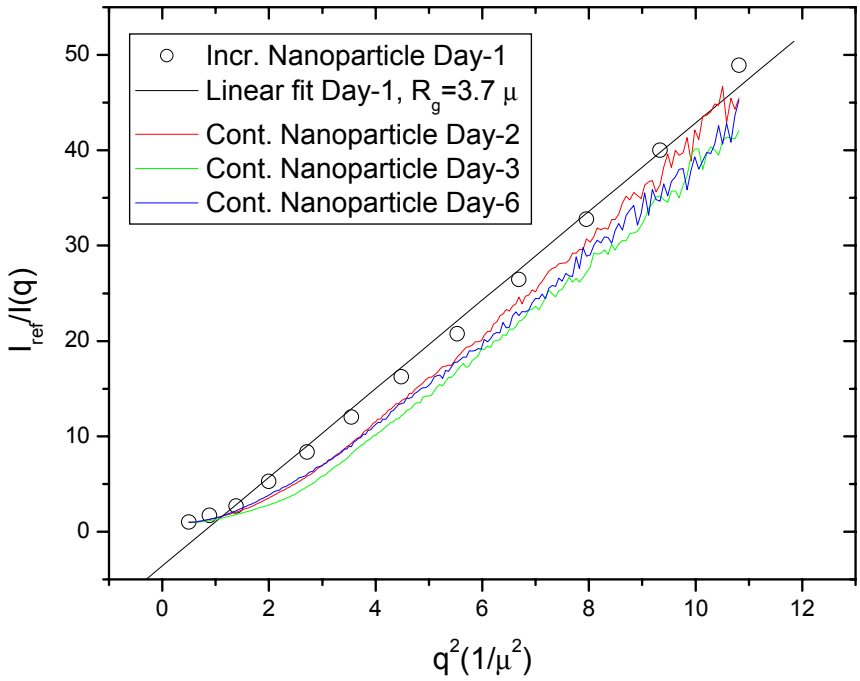

Figure 4.9. Comparison of R_g for aggregates of WO_3 nanoparticles in a span of six days. Incremental measurements on Day-2, 3, and 6 (not shown) give R_g=3.9, 3.8, and 3.7 μm, respectively.

CHAPTER 5

DISPERSION STABILITY AND AGGREGATION BEHAVIOR OF WO_3 NANOWIRES IN POLAR SOLVENTS

5.1. INTRODUCTION

Dispersion of nanomaterials of diverse shapes in a variety of solvents is important for applications involving cosmetics, pharmaceuticals, paints, inks, composites and catalysts. However, stable dispersion of many nanostructures in a variety of solvents, especially without the addition of a dispersant, is extremely difficult to achieve as they tend to agglomerate fairly quickly [54]. Nanomaterial powders can be dispersed in these solvents by breaking their agglomerates using mechanical milling and ultrasonication [90, 155], but there is evidence that effectiveness of ultrasonication is limited, and may even cause re-agglomeration after certain levels [156]. As a result, there have been numerous efforts to produce stable dispersions of nanoparticles using surfactants, polymer coatings and adjusting the pH.

The process of aggregation is integral to how colloid systems evolve irrespective of the geometry of the nanomaterials. It is important to understand the structure and properties of the resulting clusters to better control many important industrial processes mentioned above [64, 65]. The stability of these colloidal systems is generally imparted by the DLVO-type electric double layer repulsion, whereas aggregation of fine particles into larger aggregates can be initiated by the addition of moderate amounts of a simple inert electrolyte [67]: (p. 3)—a topic which we will return in Chapter 6.

Characterization of colloidal particles can be achieved using advanced microscopy techniques, such as SEM, TEM or AFM. However, off-line analysis techniques such as

SEM have the potential risk of modifying aggregate structure during handling or biasing aggregate orientation on a slide. Therefore, it is preferable to use non-intrusive in-situ characterization tools that can produce accurate results rapidly, such as the small angle static light scattering technique we have utilized in Chapter 4 [67]: (p. 5), [68]. Static light scattering technique samples large numbers of aggregates at a time, and provides a statistical average of the aggregate mixture. Elliptically polarized light scattering (EPLS) technique is also based on static light scattering and provides additional details on the size, size distribution, shape and structure of particles and their agglomerates. Details of the EPLS technique used in this study can be found in Chapters 2 and 3 of this dissertation and in [69, 144].

Extensive in-situ agglomeration studies using these powerful techniques are available on clusters which consist of a number of small, spherical particles forming tenuous geometries. These geometries usually cannot successfully be approximated with simple shapes and conventional geometrical tools, but are statistically described in terms of the concepts of fractal geometry [90], [65]: (p. 261), [81]: (p. 1379). The research on fractal aggregates formed by primary particles in shapes other than spheres, however, is scarce. As an example, we have shown in the previous chapter that the aggregation behavior of cylindrical particles does not necessarily follow the same patterns as the agglomerates of spherical or irregular nanoparticles in the same solvents.

Recent advances in synthesis of one-dimensional nanowires, the cylindrically shaped materials with high aspect ratios, present unique opportunities and challenges in material science. Typical diameters of these nanowires range between 1-100 nm and their lengths between 1-10 μm. Only recently, a few studies discussed the dispersion of nanowires in various polar solvents without the use of dispersants [66, 149], and we will address this issue here in detail. In Chapter 4, we investigated the effect of aspect ratios of nanowires on their aggregation patterns and the morphology of resulting aggregates and compared these findings with those of spherical nanoparticles. In the present chapter, we will investigate the effect of various commonly used polar solvents such as water, 1-methoxy-2-propanol (1M-2P) and N,N-dimethylformamide (DMF) on the stability of the

dispersions of tungsten trioxide (WO_3) nanowires, their aggregation behavior and the aggregate structures that would lead to observed fractal properties.

The geometry of WO_3 nanowires were established using SEM pictures. The primary particles comprising the WO_3 aggregates have the appearance of circular cylinders "bundled" together that resulted in an overall diameter of about 100 nm and an average wire length of 2 μm. The morphology of WO_3 aggregates formed by nanowires is described by means of the small angle static light scattering and the EPLS techniques. Scattered light intensities will be used to determine spatial extent or radius of gyration of the aggregate (R_g), fractal dimension (D_f), and the change in aggregate structure as a function of time and solvent type. To our knowledge, this study is the first attempt for in-situ description of the underlying causes, such as aggregate morphologies and aggregation rates, of the observed dispersion and sedimentation behaviors of inorganic nanowires that were not subjected to any surface treatment or functionalization.

5.2. EXPERIMENTAL DETAILS

5.2.1. Nanowire Synthesis and Sample Preparation

WO_3 nanowires were synthesized by the research team of Dr. Sunkara at the University of Louisville in a hot filament CVD reactor. The main difference in the experimental conditions that resulted in the observed morphology of "bundled" nanowires is that a furnace around the quartz reactor walls was not used. Instead, the radiation from the tungsten filament (1690^{o}C) heated the reactor walls to temperatures around 500-600^{o}C. The other important difference of the bundled nanowires was in the way their suspensions were prepared. After a high power ultrasonication followed by a low power ultrasonic bath, the suspensions were left on the shelf in glass vials for a few hours. Thicker wires and their agglomerates sedimented and the well-dispersed supernatants were taken out into a new glass vials which comprised the actual samples the light scattering experiments were made on. The sediments were collected and the

weight percents of the dispersed nanowires were calculated. The reader is referred to our joint article for further details [53].

5.2.2. Light Scattering Setup

In this chapter, the EPLS setup was used to measure scattering matrix elements, but was modified to *also* carry out the vertically polarized incident and detected light (I_{vv}) measurements, as described in detail in Chapter 3. After the EPLS measurements, the quarter wave plate located after the polarizer in the path of the incident beam, and the quarter wave plate located before the polarizer in the path of the scattered beam were removed to also perform the I_{vv} measurements.

5.2.3. In-Situ Characterization Procedure

The samples which arrived as suspensions of WO_3 spherical nanoparticles and WO_3 nanowires were diluted to volume fractions in the order of $f_v=10^{-6}$ to ensure independent scattering behavior. Samples were carefully drawn out of their bottles with a Fisherbrand Finnpipette and transferred into sample cell containing 100 ml of the solvent used. After gently stirring the suspension, the sample cell was placed on the cell holder platform in the experimental setup. Although the samples were dispersed, or broken to desired length by means of ultrasonication in the synthesis and sample preparation stage, no additional ultrasonication was used on any "bundled" WO_3 nanowire samples before light scattering measurements. The sample of well dispersed WO_3 nanowires (ρ=7.16 g/cm^3, m=1.98+i0.009) on which the measurements were performed had an average diameter of around 100 nm and a nominal length of 2 μm as determined from SEM images.

Measurement of I_{vv} intensity was performed starting from scattering angle $\theta=3^o$. Continuous plots are the average of two measurements for all figures given below unless otherwise is stated. Continuous measurements were performed at a low sweeping speed with PMT readings of 10 counts/s. The majority of experiments were performed between $\theta=3^o$-90^o and lasted for 174 seconds. All samples were also subjected to measurements at

discrete scattering angles, with 1^o increments up to about $\theta=10^o$ and higher increments thereafter. Incremental measurements on WO_3 nanowire samples were taken for 10 seconds (100 readings) at each angle. Similar to the measurements in Chapter 4, the incremental readings fluctuated evenly around a mean intensity at each discrete angle in the measurements presented below. Relative variance at low q was negligible, but increased considerably at the last few data points of very high q. Increased noise with higher q was also the case for continuous measurements.

Good experimental practices demand the standardization of the measurements from the more elaborate EPLS setup by calibrating it using known results. This was done by preparing a suspension of 450 nm average diameter polystyrene latex spheres in distilled water, and comparing experimentally measured scattering matrix elements with those from the Lorenz-Mie scattering theory for homogeneous spheres of the same size and optical properties. Latex sample was carefully drawn from its bottle (Duke Scientific 5045A, $\rho=1.05$ g/cm^3, $n=1.59$) with a Fisherbrand Finnpipette and diluted to a volume fraction of $f_v=1.1\times10^{-6}$ followed by ultrasonication at a moderate power for several minutes.

EPLS measurements as well as I_{vv} measurements were performed with bundled WO_3 nanowires suspended in three different solvents: 1-methoxy-2-propanol ($\rho=0.921$ g/cm^3, $n=1.403$), distilled water ($\rho=1.0$ g/cm^3, $n=1.333$), and N,N-dimethylformamide ($\rho=0.948$ g/cm^3, $n=1.428$) with 0.1 wt%. These samples were prepared from their respective concentrated suspensions of 0.7wt%, 0.5 wt%, and 0.4 wt% with which some *additional* measurements were performed to investigate the effect of increased particle concentration during storage. All samples were diluted to volume fractions of the order of $f_v=10^{-6}$ to ensure independent scattering behavior. EPLS and I_{vv} measurements on the diluted samples of WO_3 nanowires were performed *without* any stirring. EPLS measurements were carried out with 5^o increments between $\theta=25^o$-145^o, and for the six different sets of polarizer and retarder angle combinations as explained in Chapter 3.

5.3. RESULTS AND DISCUSSION

5.3.1. SEM Analysis of Bundled WO_3 Nanowires

SEM images showing the WO_3 nanowires are given in Figure 5.1. The nanowires seen in the figure have a wide distribution in diameter and length. The primary particles comprising the aggregates of WO_3 nanowires have the appearance of a number of cylinders "bundled" together that result in an overall diameter of about 100 nm with an average wire length of 2 μm. Different process conditions during chemical synthesis yield different nanowires (e.g., single or bundled), and depending on the power and duration of ultrasonication used to prepare the nanowires, their aggregates can break up then re-aggregate in the suspension (e.g., see [156]). Bundled WO_3 nanowires, therefore, are expected to have a different size distribution and possibly form different aggregate structures than "uneven" nanowires of a similar average length which were examined in Chapter 4. The nominal size parameter of an individual bundled WO_3 nanowire of L=2 μm average length is x=10, or x_{eff}=1.5. However, for the bundled nanowire samples λ=632 nm and r_o=20 nm were used in the I_{vv} versus qr_o plots to consistently compare all measurements with the single nanowires as well as with spherical nanoparticles. As mentioned in Chapter 4, the application of RGD theory is still justified with such high particle sizes for the determination of fractal dimensions as we will rely on finding the D_f from a log-log plot of I_{vv} intensity versus q (rather than absolute value of I_{vv}).

5.3.2. Effect of Solvent Type on Aggregation

As always, the experimental setup was tested for proper alignment and configuration of the optical components for the EPLS technique by comparing experimentally measured scattering matrix elements with those from the Lorenz-Mie scattering theory. Figure 5.2 presents theoretical predictions together with the measurements performed on a suspension of 450 nm average diameter latex spheres in distilled water at a volume fraction of $f_v=1.1\times10^{-6}$. Experimental measurements in all six figures are in very good agreement with the theory which demonstrates the proper alignment of the setup. The

discrepancy in S_{34} between experimental measurements and the theoretical values in Figure 5.2.e is moderate and experimental results follow the trends of theoretical curve to a good extent. This observation is in line with the well known fact that S_{34} is difficult to obtain experimentally for any combination of retarder and polarizer angles [90].

EPLS measurements on bundled WO_3 nanowires for three different solvents all with 0.1 wt% WO_3 nanowire content were performed after the calibration of the setup. Samples from 1-methoxy-2-propanol, distilled water and N,N-dimethylformamide suspensions were diluted to volume fractions f_v=0.6×10^{-6}, 0.8×10^{-6}, and 0.7×10^{-6}, respectively. Measurements of S_{11}-S_{22} (normalized by the highest value at θ=25^o) versus qr_o for the three samples are plotted in Figure 5.3. To find the slope a linear fit was performed on incremental measurement data points between θ=25^o-50^o, θ=30^o-65^o and θ=30^o-70^o, which yielded fractal dimensions of 1.80, 1.77, and 1.35 for WO_3 nanowires in 1-methoxy-2-propanol, distilled water and N,N-dimethylformamide, respectively.

The difference in fractal dimensions is the evidence to the effect of solvent rheological properties on aggregation behavior of WO_3 nanowires. All three suspensions were prepared from the products of the same nanowire synthesis. It should be emphasized, however, that due to the polydispersity of the nanowires and the consequent errors in pipetting, the samples might very well be biased towards a certain size distribution in one suspension than the other. Therefore, rather than using the absolute values of the fractal dimensions reported above, their relative values should be emphasized as an indication of the effect of solvent type. The comparison of fractal dimensions clearly favors the use of N,N-dimethylformamide to obtain relatively open, linear aggregates of WO_3 nanowires. N,N-dimethylformamide has increased stability of WO_3 nanowires in the suspension by reducing their tendency to form entangled, high fractal dimension aggregates. A similar value of fractal dimension (D_f=1.42) found through numerical simulations was attributed to polarizable clusters formed as a result of aggregation on tips of aggregates [131].

Another important point that should be noted is that there is almost a week difference for between the time the bundled WO_3 nanowire suspensions were prepared and any light

scattering analysis was performed, which might have affected fractal dimension to some extent. This, however, is expected to be a minor effect, since WO_3 nanowires of *low* aspect ratios tend to have a slow aggregation rate even in extended periods of time as discussed in Chapter 4. Measurements on bundled WO_3 nanowires were repeated to detect possible changes in aggregate morphology with time. The measurements in Figure 5.3 are labeled as Day-1.

5.3.3. Change in Aggregate Morphology with Time

Figure 5.4.a shows normalized I_{vv} versus q measurements for bundled WO_3 nanowire aggregates in 1-methoxy-2-propanol at $f_v=0.6\times10^{-6}$ carried out 2 days (labeled as Day-3) and 5 days (labeled as Day-6) after the first measurements shown in Figure 5.3. Solid lines corresponds to the average of two continuous measurements performed for scattering angles between $\theta=3^o$-90^o. Experiments between the same scattering angles were repeated by performing the measurements at discrete scattering angles. It is apparent in Figure 5.4.a that the incremental measurements follow the trend of the continuous measurement except for a shift in intensity readings to lower values, which was also observed for the measurements given in Chapter 4. Using incremental measurements provide more reliable estimates as discussed in Chapter 4, and was used throughout this chapter.

On Day-3, D_f=1.82 was found from the slope of the fractal scattering region by making a linear fit on data points between $\theta=6^o$-20^o, a negligible increase within a 2 day period. Guinier analysis of the same measurements produced R_g=2.2 μm from the linear fit between $\theta=6^o$-18^o as shown in Figure 5.4.b. D_f=1.92 found on Day-6 from the slope of the fractal scattering region between $\theta=6^o$-20^o as shown in Figure 5.4.a proves that there is only a slight increase in fractal dimension of nanowire aggregates during the 6 day time span. Guinier analysis of the same measurements produced R_g=1.9 μm from the linear fit between $\theta=5^o$-16^o as shown in Figure 5.4.b. The slight decrease in R_g corresponds to a negligible change in the spatial extent of nanowire aggregates in the same time period.

The increase in the fractal dimension does not necessarily point to the existence of a tendency of WO_3 nanowires to aggregate, but confirms the presence of restructuring of the aggregates in the suspension. Note that even though no shearing forces to complicate the structure were present for nanowire suspensions of bundled WO_3 nanowires, restructuring may still have occurred due to van der Waals attraction. R_g on the other hand is an indication to the emergence of larger particles formed by aggregation and should be observed along with any increase in absolute values of forward scattered intensities to follow an aggregation process. Bundled WO_3 nanowire aggregates in 1-methoxy-2-propanol therefore seem to breakup to a small extend and turn into slightly more compact aggregates.

A similar test was done on bundled WO_3 nanowire aggregates in water with the suspension that has 0.5 wt% initial concentration. Two samples of bundled WO_3 nanowire aggregates in water at $f_v=1.3\times10^{-6}$ were prepared on Day-3 and Day-7 of the measurements. Figure 5.5.a shows normalized I_{vv} versus q measurements for the two measurements performed for scattering angles between $\theta=3^o$-90^o. On Day-3, $D_f=2.63$ was found from the slope of the fractal scattering region by making a linear fit on data points between $\theta=6^o$-20^o. An increase to $D_f=2.74$ was observed on Day-7 as found from a linear fit between $\theta=6^o$-18^o. Guinier analysis of the same measurements as shown in Figure 5.5.b produced $R_g=3.1$ μm from the linear fit between $\theta=6^o$-16^o and $R_g=3.5$ μm between $\theta=7^o$-18^o on Day-3 and Day-7, respectively. Unlike the results seen in for 1-methoxy-2-propanol in Figure 5.6, the more compact WO_3 aggregates seen in Figure 5.5 were attained along with an increase in size, i.e., through aggregation, in water.

Results of two other measurements performed (not shown) on samples diluted from more concentrated suspensions on Day-3 are tabulated in Table 1. Measurements performed for bundled WO_3 nanowire aggregates in 1-methoxy-2-propanol diluted to $f_v=0.9\times10^{-6}$ was prepared from its suspension with an initial concentration of 0.7 wt%. The sample in N,N-dimethylformamide diluted to $f_v=1.0\times10^{-6}$ was prepared from its suspension of 0.4 wt% initial concentration.

Even in the absence of shearing forces, van der Waals forces will ensure that particles will bond one another when brought close enough thus restructure the aggregate [67]: (p. 9). In fact, high concentration suspensions such as the one in Figure 5.5 are potentially at a higher risk of undergoing restructuring due to increased probability of bonding (see a discussion of various effects on aggregation in Chapter 6). However, the higher initial suspension concentration does not seem to have a major effect on WO_3 aggregates when 1-methoxy-2-propanol was used as the solvent. D_f=1.86 and R_g=1.8 μm on Day-3 (0.7 wt%) given in Table 1 are very close to the results given in Figure 5.4 (0.1 wt%) on the same day.

Similarly, even with a higher storing concentration (Day-3, 0.4 wt%) N,N-dimethylformamide maintained linear structure of WO_3 nanowire aggregates and had a D_f=1.43 as seen in Table 1 (compared to D_f=1.35 in Figure 5.3). Although fractal dimension for nanowire aggregates was the lowest in N,N-dimethylformamide, the aggregate size (R_g=2.6 μm) for the same sample, was between those obtained with 1-methoxy-2-propanol or water as solvents. Therefore, the effect of storing the suspensions in higher concentrations used in this study does not universally cause to an increase in fractal dimension or aggregate size. Further investigation on the effect of storage concentration is needed for more definitive conclusions.

5.4. SUMMARY

We have studied the effect of solvent rheological properties on aggregation characteristics of the WO_3 nanowires. Of all the three solvents used to suspend bundled WO_3 nanowires, DMF produced the most linear structure, although their aggregates were intermediate in size (in terms of R_g) when compared to those obtained with water (largest R_g) and 1M-2P (smallest R_g). 1M-2P also created an open structure (though not as perfectly linear as was with DMF), but provided the smallest aggregate size, indicating a small tendency for aggregation, and weak bonds between the primary particles. Water

causes dramatically more compact aggregates (D_f=1.8-2.7) and the highest aggregate size (up to 3.5 μm), and as such would not provide well-dispersed, stable suspensions.

The aggregate structures created by 1M-2P could be visualized to be in the form of snow flakes. In a suspension the snow flakes coagulate with one another (diffusion limited cluster-cluster aggregation) to create somewhat a high D_f (~1.80 on Day-1 to ~1.92 on Day-6, no mechanical stirring). The increase in fractal dimension shows that these clusters may have a tendency to aggregate in a period of six days, but their bonds are fragile so as to break, for example, during sampling (i.e., restructuring) that the overall extent of nanowire aggregates decreases (R_g~2.2 on Day-3 to ~1.9 on Day-6).

The aggregate structures created by DMF could be visualized to consist of bundles of wires like a bunch of pencils. The D_f is small (1.35 to 1.43), and the pencil bunch looks linear as a result of aggregation on tips of aggregates which could be attributed to "polarizable" nanowire clusters. R_g on the other hand is very large (~2.6 μm), because the bunch is large in spatial extent.

The closed structures formed in water, on the other hand, do not easily break up from one another. They were more entangled and round, and in time combined together to form even larger R_g.

Storing the suspensions in higher concentrations up to the values presented in this study does not universally cause to an increase in aggregate size (due to increased frequency of collisions) or a lower fractal dimension (due to fast reaction), which we will deal with more detail in Chapter 6.

A sketch of the nanowire geometries which we examine in this study is given in Figure 5.6. In this figure we also suggest the possible aggregate structures based on our discussions above for the "bundled" WO_3 nanowires of Chapter 5, as well as for the "single" and "uneven" nanowire geometries investigated in Chapter 4.

Table 5.1. Fractal properties of aggregates of "bundled" WO_3 nanowires. (*Measurements were performed approximately one week after suspension was prepared.)

Solvent	Suspension was Sampled*	Initial wt%	D_f (or Slope)	R_g, μm
1-Methoxy-2-Propanol	Day-1	0.1	1.80	-
N,N Dimethyl Formamide	Day-1	0.1	1.35	-
Water	Day-1	0.1	1.77	-
1-Methoxy-2-Propanol	Day-3	0.1	1.82	2.2
1-Methoxy-2-Propanol	Day-6	0.1	1.92	1.9
Water	Day-3	0.5	2.63	3.1
Water	Day-7	0.5	2.74	3.5
1-Methoxy-2-Propanol	Day-3	0.7	1.86	1.8
N,N Dimethyl Formamide	Day-3	0.4	1.43	2.6

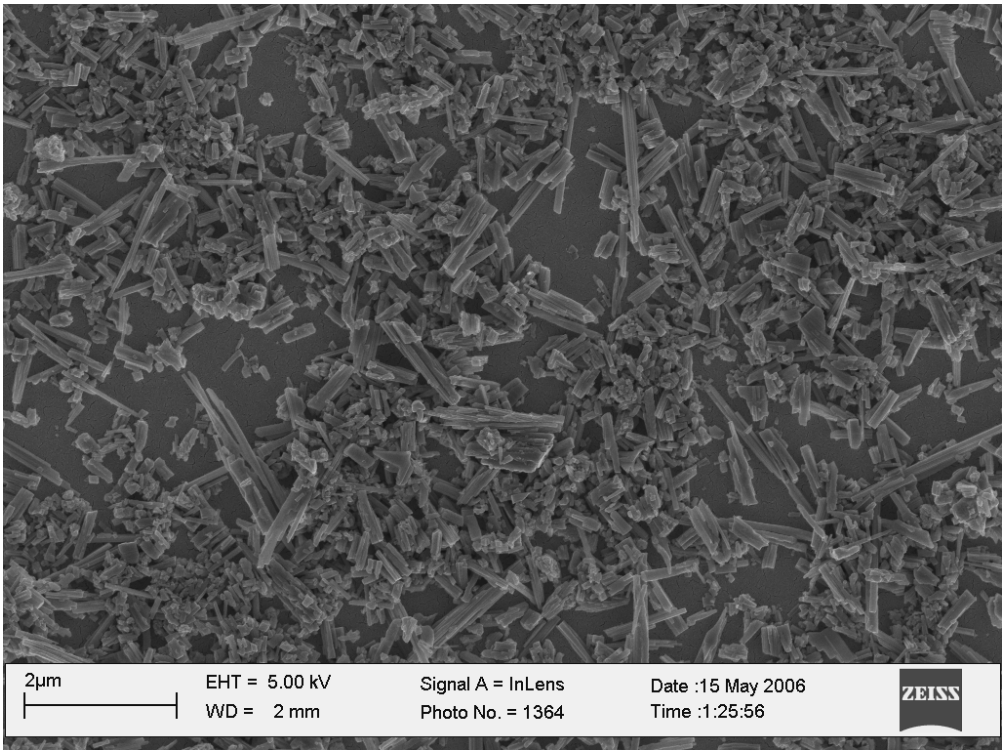

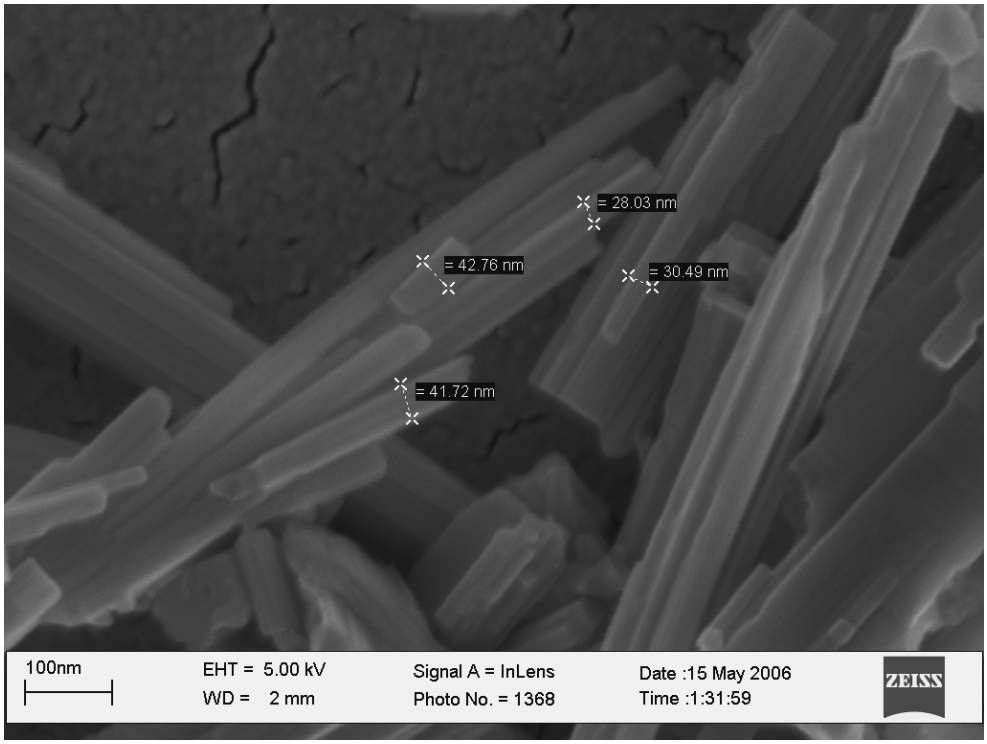

Figure 5.1. SEM images of aggregates of bundled WO_3 nanowires of 2 µm average length.

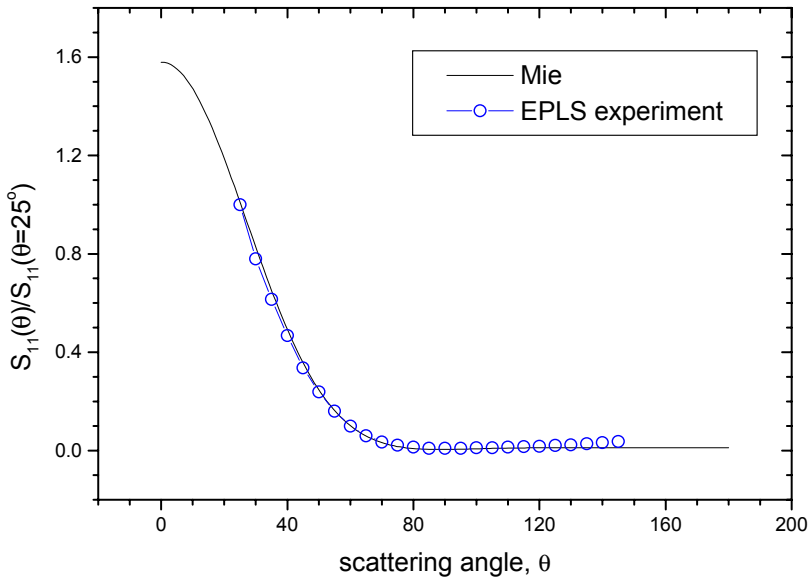

Figure 5.2.a. Scattering matrix element S_{11} normalized by its value at θ=25°. Comparison of EPLS measurements and exact values from the Lorenz-Mie scattering theory for latex spheres suspended in water.

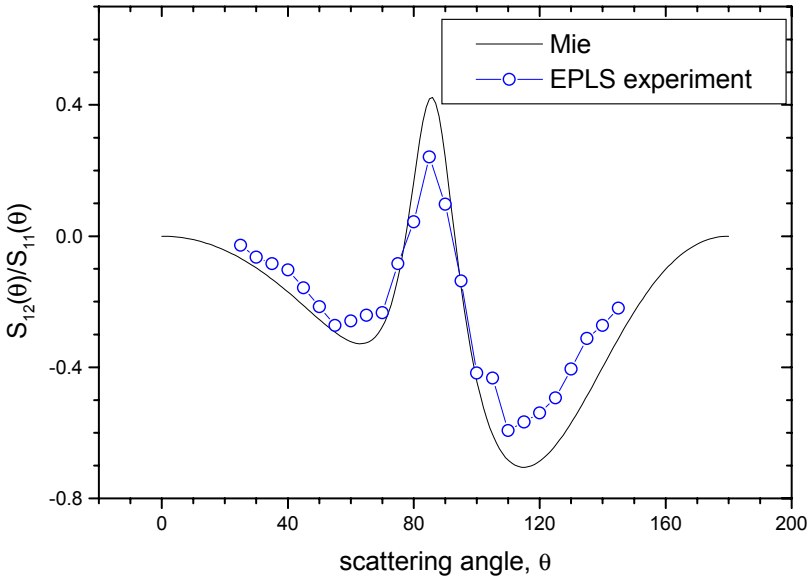

Figure 5.2.b. Scattering matrix element S_{12} normalized by S_{11} at the same angle. Comparison of EPLS measurements and exact values from the Lorenz-Mie scattering theory for latex spheres suspended in water.

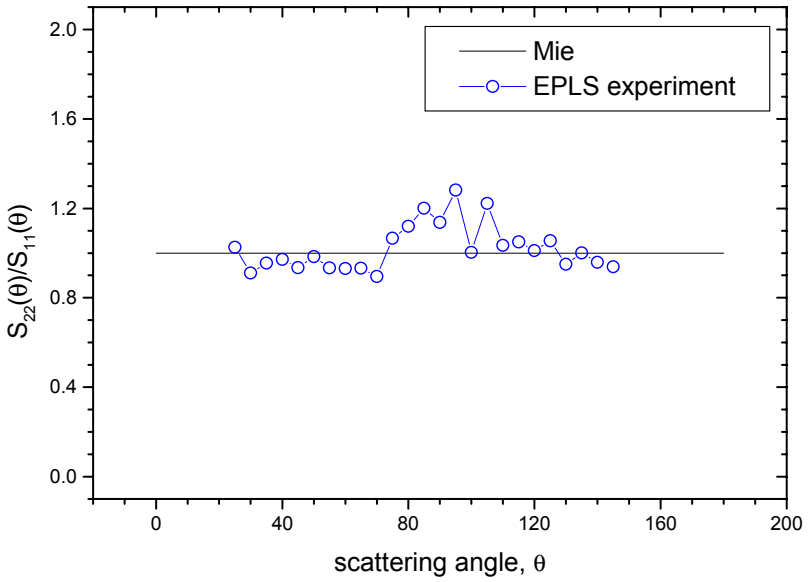

Figure 5.2.c. Scattering matrix element S_{22} normalized by S_{11} at the same angle. Comparison of EPLS measurements and exact values from the Lorenz-Mie scattering theory for latex spheres suspended in water.

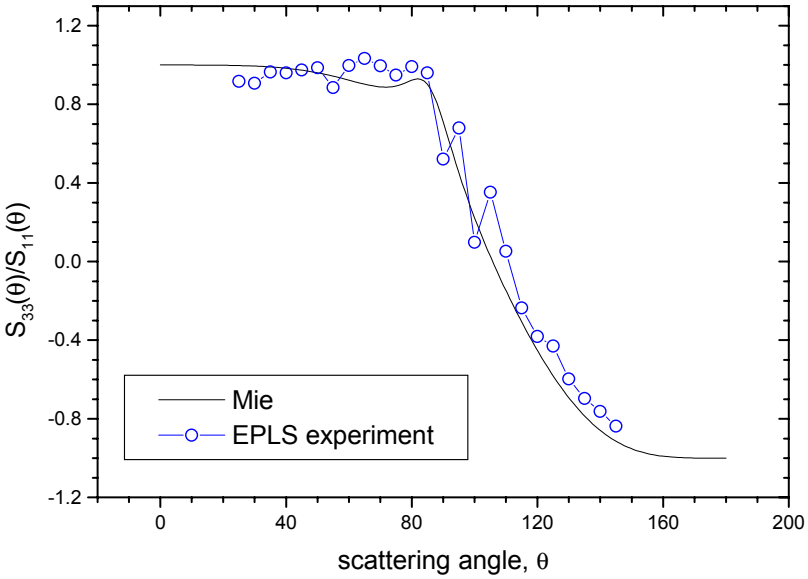

Figure 5.2.d. Scattering matrix element S_{33} normalized by S_{11} at the same angle. Comparison of EPLS measurements and exact values from the Lorenz-Mie scattering theory for latex spheres suspended in water.

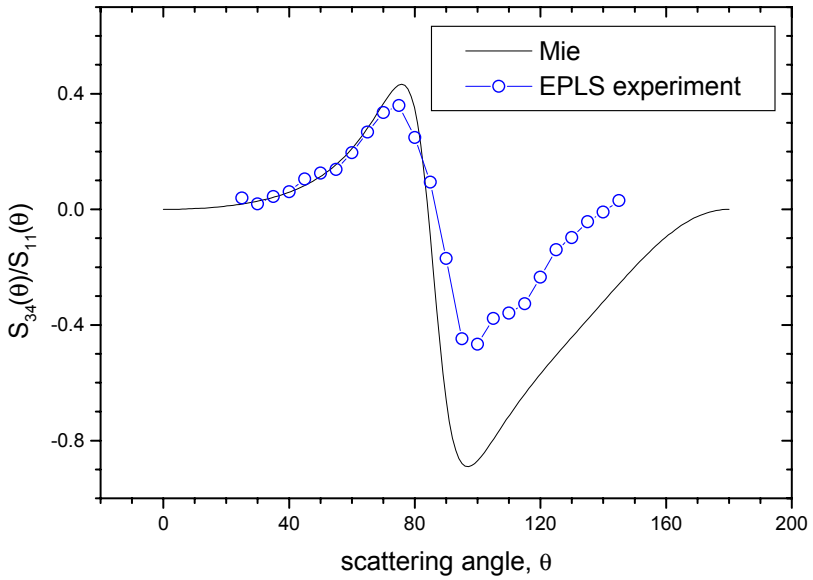

Figure 5.2.e. Scattering matrix element S_{34} normalized by S_{11} at the same angle. Comparison of EPLS measurements and exact values from the Lorenz-Mie scattering theory for latex spheres suspended in water.

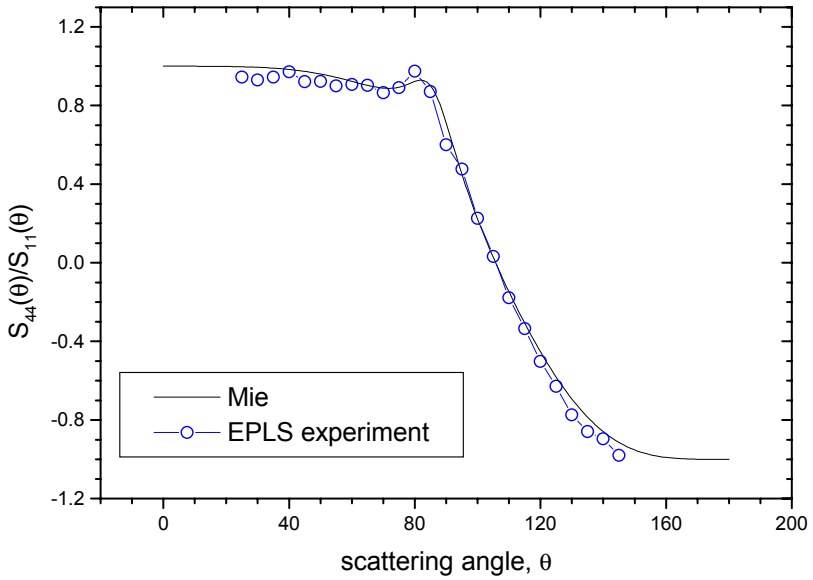

Figure 5.2.f. Scattering matrix element S_{44} normalized by S_{11} at the same angle. Comparison of EPLS measurements and exact values from the Lorenz-Mie scattering theory for latex spheres suspended in water.

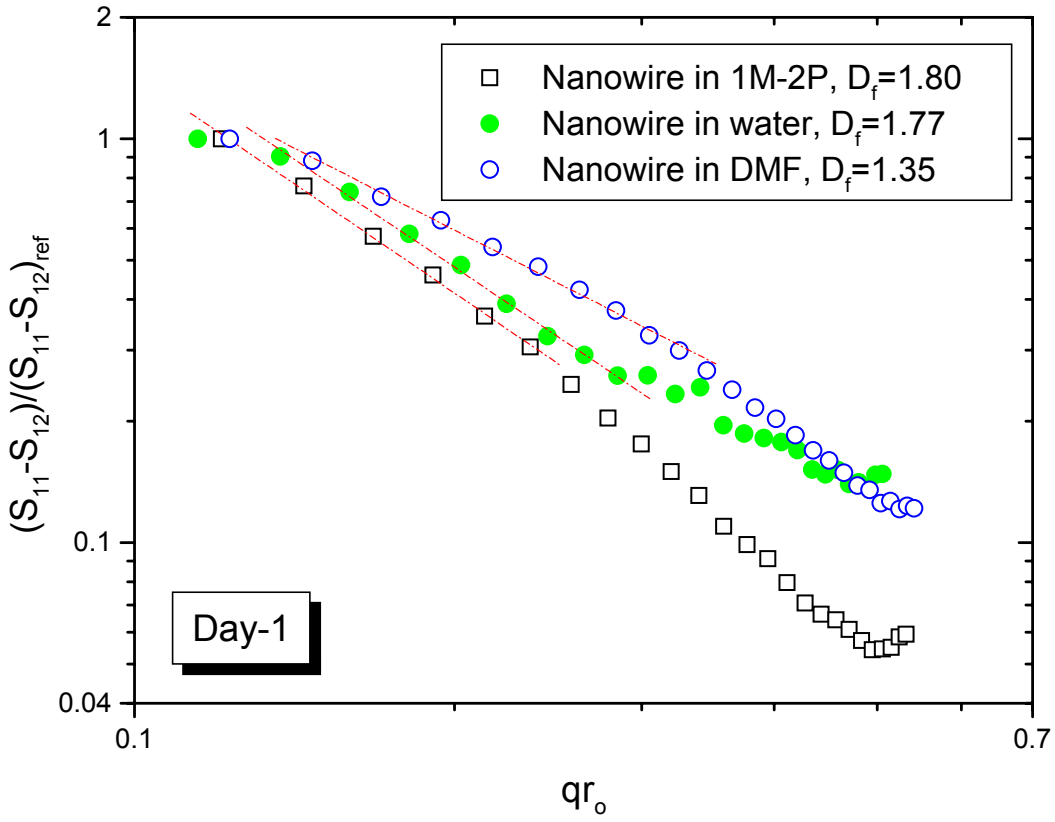

Figure 5.3. Determination of fractal dimension using elliptically polarized light scattering (EPLS) for aggregates of "bundled" WO_3 nanowires of 2 µm average length in 1-methoxy-2-propanol (1M-2P), water and N,N-dimethylformamide (DMF) on Day-1. Linear fit is for incremental data points between θ=25°-50°, θ=30°-65° and θ=30°-70°, respectively.

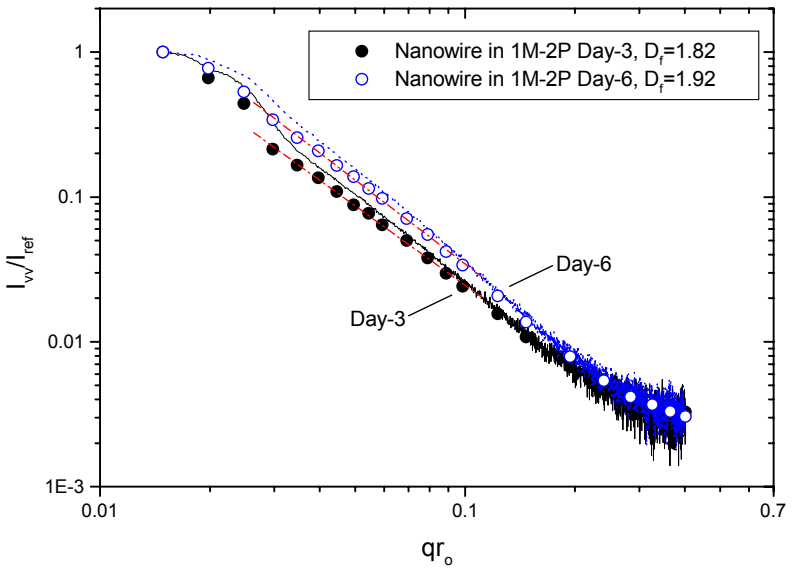

Figure 5.4.a. Determination of fractal dimension using small angle static light scattering for aggregates of bundled WO_3 nanowires of 2 µm average length in 1-methoxy-2-propanol (1M-2P) on Day-3 (solid line, solid circle) and Day-6 (dotted line, open circle). Linear fits (dash-dot) are for incremental data points between θ=6°-20°.

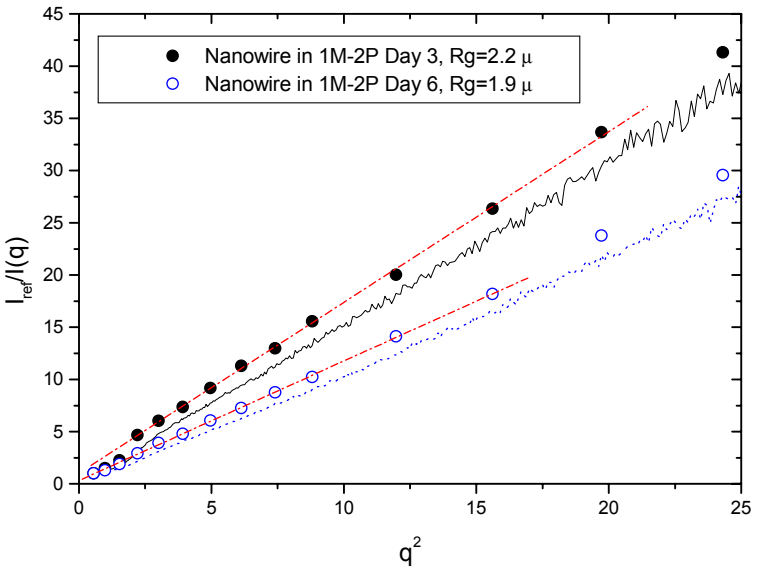

Figure 5.4.b. R_g for aggregates of bundled WO_3 nanowires of 2µm average length in 1-methoxy-2-propanol (1M-2P) on Day-3 (solid line, solid circle) and Day-6 (dotted line, open circle). Linear fits (dash-dot) are for data points between θ=6°-18° and θ=5°-16°, respectively.

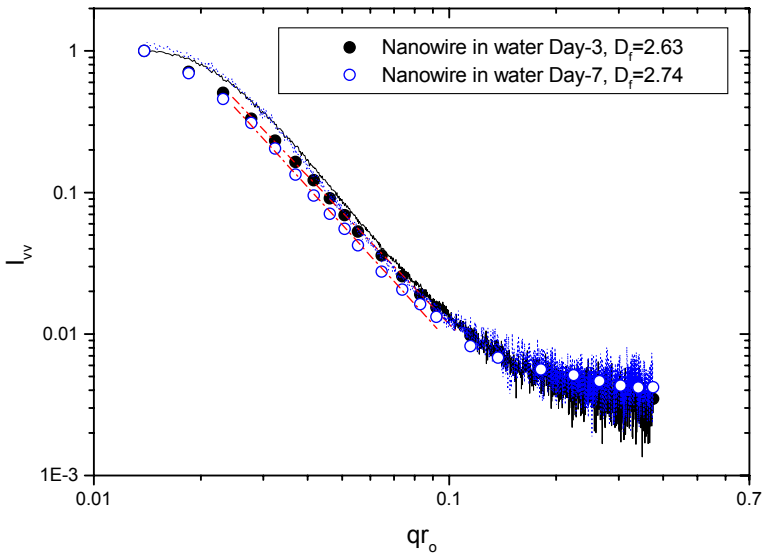

Figure 5.5.a. Determination of fractal dimension using small angle static light scattering for aggregates of bundled WO_3 nanowires of 2 μ average length in water on Day-3 (solid line, solid circle) and Day-7 (dotted line, open circle). Initial nanowire concentration is 0.5 wt%. Linear fits are for incremental points between θ=6°-20° and θ=6°-18° for Day-3 and Day-7, respectively.

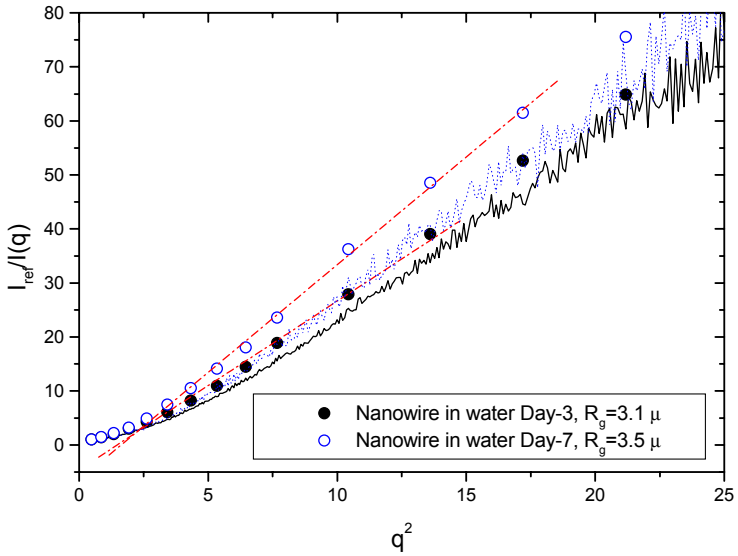

Figure 5.5.b. R_g for aggregates of bundled WO_3 nanowires of 2μm average length in water on Day-3 (solid line, solid circle) and Day-7 (dotted line, open circle). Initial nanowire concentration is 0.5 wt%. Linear fits (dash-dot) are for data points between θ=6°-16° and θ=7°-18° for Day-3 and Day-7, respectively.

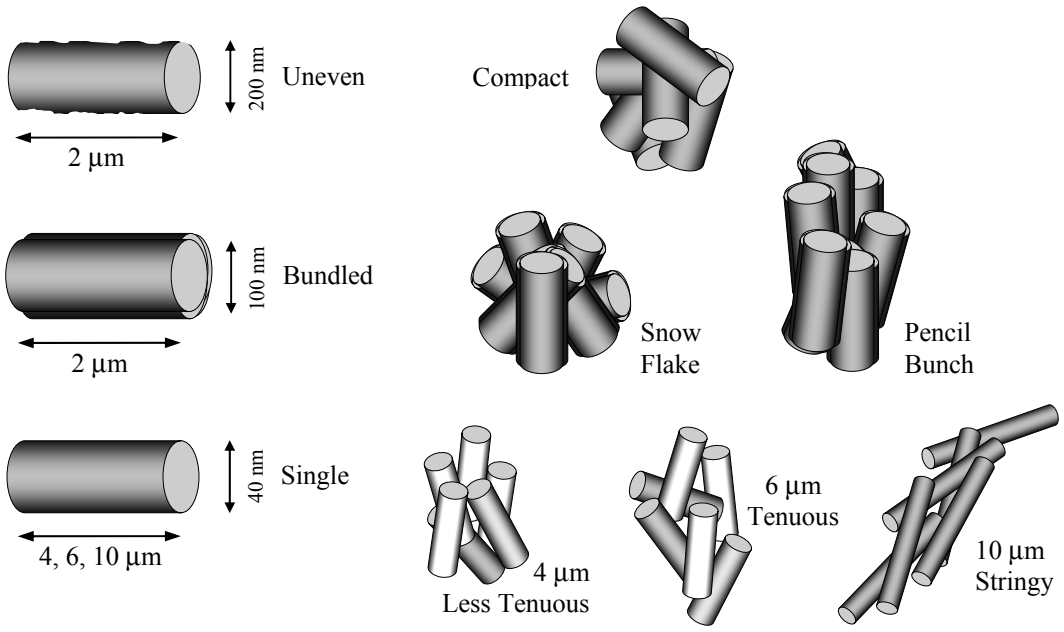

Figure 5.6. Classification based on appearance of nanowires and their aggregates, approximate dimensions (not to scale).

CHAPTER 6

AGGREGATION OF WO_3 NANOWIRES AUGMENTED BY ELECTROLYTE ADDITION

6.1. INTRODUCTION

Aggregation mechanisms from colloid formation to diffusion or reaction limited conditions, and the resulting structures have been studied extensively in the literature for spherical primary particles of various materials [61]. Aggregation of nanoparticles is usually induced by a chemical agent in the solution. Most commonly these are univalent or higher ionic strength electrolytes (such as NaCl, KCl, KNO_3, CsCl, $MgCl_2$, $CaCl_2$, Na_2SO_4) which are added at different concentrations to induce aggregation of nanoparticles suspended in water. The surface charge on the particles is adjusted by the pH of the solution [61, 157] by the addition of appropriate amounts of acid or base (e.g., HCl, NaOH, HNO_3, KOH); or soaking the particles in an appropriate pH solution (stock solution) well before adding them into the electrolyte solution [93, 158]. The electrolyte brings down the potential barrier due to the surface charge that already existed or was created by the pH of the solution, and the contribution of the electrolyte addition can be parametrically studied. It should be noted, however, that the aggregation in colloidal dispersions is not always an undesirable phenomenon, such as in the case photonic glasses are grown [97, 159].

The aggregation reaction is a function of many parameters including temperature, species concentrations (of clusters made up of various numbers of monomers and of the electrolyte), pH of the solution, surface treatment of particles, and the presence of shear forces on the aggregated structures. Table 6.1 presents a summary of aggregation studies that worked on these parameters and the outcomes they have observed [61, 93, 157, 158, 160]. However, aggregation studies available in the literature have focused on spherical

particles and resulting fractal structure as mentioned in the previous chapters. For example, using the EPLS technique Saltiel and coworkers have investigated the rate of change of fractal dimension for TiO_2 nanoparticles with and without surface treatment in the absence of an electrolyte that would have expedited the aggregation [90].

The one exception that we came across with which studied aggregates formed by non-spherical primary particles was that of Vincze and coworkers [92]. They used carbon rods which are quite larger (~140 μm long, with 35 μm diameter) than the average nanowire sizes investigated in this study [92]: (p. 7457, and their Tables 2 and 3). This study was limited to a two-dimensional geometry at the water-air interface. In addition, two dimensional images, rather than a light scattering technique, were used to predict the D_f. Therefore, the extension of aggregation analyses of cylindrical geometries (such as rods, wires, or fibers) to three-dimensional systems (colloidal dispersions) is an important addition to the literature. Universal limits on D_f for fractal structures formed with primary particles of these geometries using numerical simulations (see Chapter 2 for the related theory) and light scattering measurements (as experimental verification) are also needed in three dimensional space.

The electrolyte induced aggregation processes can be observed by means of light scattering techniques such as the small-angle static light scattering technique to infer the spatial extent (radius of gyration, R_g) and the structure (fractal dimension, D_f) of the aggregate defined in terms of fractal geometry [53, 64]. Static light scattering is a powerful in-situ characterization tool since it samples a large number of aggregates, and thus provides a statistical average of the aggregate mixture. As such, it has well-known advantages over the off-line analysis techniques such as SEM, TEM and AFM which have the potential risk of modifying aggregate structure during handling or biasing aggregate orientation on a slide [67]: (p. 5), [68]. Controlled self assembly of nanowires which respond to magnetic fields have been characterized using light scattering techniques in the literature, although with no comprehensive fractal analysis [161, 162]. To our knowledge, electrolyte induced aggregation and characterization of aggregates

using light scattering techniques for cylindrical primary particle geometries is not available in the literature.

In this chapter, we explore the possibility of describing the aggregation process of WO_3 nanowires in the presence of a simple (monovalent) electrolyte by means of the small angle light scattering technique. In particular, we present the first analysis of the limits and parameters that affect the aggregation of nanowires by monitoring the time evolution of aggregate morphology (fractal dimension, D_f) and quantify the aggregation and the corresponding settling percentages when such nanowire suspensions are introduced in a simple electrolyte solution of various concentrations. Making use of the fact that the samples under investigation were maintained in the independent scattering regime, forward scattering intensities were used to deduce information on the relative change in number concentration of the aggregates in the suspension.

6.2. EXPERIMENTAL DETAILS

6.2.1. Sample Preparation

The samples which arrived as suspensions of WO_3 nanowires (ρ=7.16 g/cm^3, m=1.98+i0.009) in water were diluted to volume fractions in the order of f_v=10^{-6} in the light scattering experiments to ensure independent scattering behavior. The primary particles comprising the WO_3 aggregates had the appearance of circular cylinders bundled together that resulted in an overall diameter of about 100 nm and an average wire length of 2 μm as determined from SEM analyses [53]. Initial concentrations of all WO_3 nanowire suspensions used in this chapter were 0.46 wt% WO_3 nanowires in water before dilution. No further ultrasonication was used on any WO_3 sample before the light scattering measurements, after those used in the synthesis and sample preparation stage.

Except for the test sample with no HCl, acidity of all samples in de-ionized water (Millipore, Milli-Q) were adjusted by using a 12.1 M HCl solution (EMD Chemicals Inc.,

~38% assay HX0603-3) such that pH=3 was achieved. KCl (EMD Chemicals Inc., 99-100.5% assay PX1405-1) used as the electrolyte was weighed to obtain electrolyte concentrations of 0.05, 0.1, 0.3, 0.5 and 1 M, and mixed with de-ionized water of pH=3. WO_3 samples were then carefully drawn out of their bottles with a Fisherbrand Finnpipette and transferred into the sample cell containing 100 ml of the solvent used. After gently stirring the suspension, the sample cell was placed into the experimental setup. The same procedure was followed for all samples.

6.2.2. Light Scattering Setup

The experimental setup used to measure the I_{vv} profiles was obtained by making the modifications on the EPLS setup described in Chapter 3. The EPLS setup was used to perform the calibration experiments before the modifications for the small angle static light scattering configuration were made.

6.2.3. In-Situ Characterization Procedure

Change of scattering behavior with time over a 24 hour period was investigated for three different samples in de-ionized water with pH=3 using 2 μm "bundled" WO_3 nanowires. Keeping the pH value constant helps isolate its affect on the aggregation so that other parameters (such as particle and electrolyte concentration) in the solutions could be studied. The first sample consisted of 0.1 M KCl at $f_v=1.3\times10^{-6}$, while the remaining two had 0.5 M KCl at $f_v=0.7\times10^{-6}$ and $f_v=1.3\times10^{-6}$. Most measurements of I_{vv} intensity in this chapter were performed for scattering angles between $\theta=3^o$-50^o, except for few cases where measurements were between $\theta=3^o$-90^o. Continuous measurements were performed at a low sweeping speed with PMT readings of 10 counts/s and lasted for 94 seconds (174 seconds if $\theta=3^o$-90^o). Continuous plots are the average of two measurements for all figures given below. Measurements at discrete scattering angles, with 1^o increments up to $\theta=10^o$ and with higher increments thereafter were taken for 10 seconds (100 readings at each point) at each scattering angle.

For each sample, the first one of the continuous measurements was performed *before* the incremental measurements, and the second immediately after. Negligible deviations observed between the two continuous measurements indicate a good degree of repeatability of measurements, so that their average was plotted. Continuous measurements provide a good indication of the onset of different regimes, however, incremental measurements provide more reliable estimates, and was used throughout this study to report D_f and the scattered intensities at different times [53, 146].

The vertically polarized incident and detected light intensity measurements (I_{vv}) reported in this chapter correspond to the angular scattered intensity measured relative to the intensity read by the reference PMT, $I_{vv} \equiv I_{rat}(\theta) = I(\theta)/I_{ref,PMT}$ as explained in Chapter 3. Since the same combination of filters was used for the *reference* PMT in all sets, I_{rat} values are also directly comparable. Otherwise, I_{rat} readings would have to be normalized by a value at a predetermined scattering angle, θ_{ref}, so that $I_{vv}/I_{vv,ref} = \Phi/\Phi_{\text{ref}}$. Scattering profiles reported in terms of I_{rat} has the advantage of providing additional information on the state of the suspension (e.g., percentage of aggregates settled) instead of a mere fractal structure, D_f, reported using the normalized intensities. Measurements presented below were *not* normalized by a reference scattered intensity (e.g., the highest attained intensity at $\theta = 3^o$) unless otherwise noted.

6.3. RESULTS AND DISCUSSION

6.3.1. Effect of Solution Acidity on Aggregation

Figure 6.1 shows the I_{vv} (I_{rat}) versus q measurements corresponding to two samples of 2 μm bundled WO_3 nanowires, suspended in de-ionized water at $f_v = 1.3 \times 10^{-6}$ one *with* (so as to achieve pH=3), the other *without* the addition of HCl. The suspensions were diluted from the original WO_3 nanowire suspension only a few minutes apart and the scattered intensity measurement on pH=3 sample followed the measurement on the sample without

any HCl. Continuous measurements were done in 174 seconds between θ=3°-90°, and are the average of two runs.

The intensity profiles for WO_3 nanowire samples in Figure 6.1 perfectly follow the exponential behavior of fractal aggregates. The subdued intensity variation at high q (Porod region) is an indication of the broad size distribution in the nanowire samples. A detailed analysis of fractal behavior of WO_3 nanowires is presented in Chapters 4 and 5 as well as in [53, 146]. To find the slope in the fractal scattering region, a linear fit was performed on incremental measurement data points of both samples between θ=7°-12°. D_f=2.89 was obtained for the sample with no HCl, and a decrease to D_f=2.73 was observed for the pH=3 sample. It should be emphasized, however, that the measurements reported in this and other figures that follow were performed about two weeks after WO_3 nanowires were synthesized and first dispersed in water, which have contributed to the high D_f observed in Figure 6.1 (measurements with no HCl in Figure 6.1 corresponds to measurements of Day-7 reported in Chapter 4 and in [53]). The increase in D_f in a period of few days reported before is indicative of the tendency of 0.46 wt% WO_3 nanowires in water to aggregate into more compact structures [53]. However, a more interesting observation in Figure 6.1 is the noted decrease in fractal dimension of the WO_3 suspension with increased acidity.

Surface charge on the WO_3 nanowires is altered with the presence of HCl in de-ionized water solution. Considering the high acidity of the solution set at pH=3, a substantial positive surface charge can be expected which lessen the tendency of WO_3 nanowires to aggregate [61]: (p. 4384), [158]: (p. 133). Due to the increased repelling forces, primary particles are now unlocked from one another, and the fractal structure becomes more tenuous. The overall extend of the aggregates is also reduced for the pH=3 solution as can be confirmed from the decreased forward scattering intensity measured at θ=3°.

Effect of pH on aggregation at various particle concentrations is studied in the literature for spherical nanoparticles and related to zeta potential or surface equilibrium electrophoretic mobility [61, 98, 157, 158]. Therefore, the zeta potential measurements

performed on various WO_3 nanowires for pH=4 to 9, at the laboratory of Dr Sunkara of UofL provide important information. The iso-electric point for 2, 6, and 10 μm WO_3 nanowires, as well as nanoparticles is reached at about pH=4, and the curve starts to reach a constant negative value at or after pH=9 [150]: (p. 43, 44 and Figures 24, 25). Although zeta-potential measurements for pH values lower than pH=4 is not provided, a symmetrical behavior (with positive zeta potential values) can be expected. For Ta_2O_5 nanowires, which also had the iso-electric point at pH=4, an increase in sedimentation was observed below pH=3 and above pH=9. This is contrary to the expected behavior of a higher aggregation rate around the iso-electric point. The observed discrepancy was explained to be a result of decreased Debye length facilitated with the high number of ions in the solution due to very low or very high pH [150]: (p. 42).

Assuming a similar behavior would be observed for WO_3 nanowires as the Ta_2O_5 nanowires, choosing pH=3 for the solutions studied in this chapter should not cause a dramatic increase in aggregation. With a low pH, the electrolyte concentration required to effect the aggregation increases according to Beattie and coworkers [158]: (p. 133 and Figure 4). However, as noted in the same study, the pH dependence of electrolyte concentration required to initiate aggregation is not the same as the pH dependence of the zeta potential [158]: (p.134). Studies methodically investigating the effect of pH on the WO_3 nanowires are needed before further comments can be made.

6.3.2. Effect of Electrolyte Addition on Aggregation

After the observations on the effect of acidity on the fractal structure of WO_3 nanowires, we have investigated the effect of presence of a monovalent electrolyte (KCl). Figure 6.2 shows the change in the scattering profile for pH=3 solutions of WO_3 nanowires in de-ionized water with the presence of 1 M KCl. WO_3 nanowires from the same 0.46 wt% initial concentration suspension was added to KCl solutions of 0.05, 0.1, 0.3, and 1 M in de-ionized water of pH=3 to achieve a particle concentration of $f_v=1.3\times10^{-6}$ as in Figure 6.1. Continuous and incremental scattered intensity measurements were performed immediately after WO_3 nanowires were added to the KCl

solutions following the same procedure detailed in the experimental section. All continuous measurements were done in 174 seconds between θ=3°-90°, and once again are the average of two runs. Measurements on pH=3 solution with no KCl was carried over from Figure 6.1 for comparison. Measurements performed for the rest of electrolyte concentrations (not shown) fall between the limits given by the two curves for no KCl and 1 M KCl solutions.

An increase in I_{vv} in forward scattering angle (at θ=3°) was detected with 1 M KCl as expected. However, the same increase was not observed for intensities at side scattering angles, and the intensity dropped rapidly after the Guinier scattering region (refer to Chapter 2 and Figure 2.4 for different regimes). D_f=2.90 was found from the slope of the fractal scattering region of the 1 M KCl solution by making a linear fit on incremental data points between θ=7°-12°, a substantial increase compared to the sample with no salt.

The slump in the fractal scattering region is indicative of a decrease in number of particles in the small end of the aggregate size distribution. The shorter Rayleigh scattering region and the bulged, non-linear behavior at intermediate q at the far end of the fractal scattering region, as well as the rapid transition in Guinier region that resulted in a high D_f are all in line with theoretical description and experimental observations in the literature of what is caused by the increased inter-particle spacing due to presence of longer primary particles alongside the shorter, and by a narrower aggregate size distribution in the nonetheless polydisperse system (see Chapter 2 for the related theory, i.e., § 2.3.2, for the effect of dilution of the fractal structure [110], and the narrow size distribution [67]).

Increase in the size of the aggregates combined with the fact that density of WO_3 is substantially higher than that of water, would result in an increase in rate of sedimentation with KCl concentration. This in turn might increase the D_f due to restructuring caused by hydrodynamic shear forces during settling, and be another factor that contributes to the observed behavior in Figure 6.2 (see [109]: (p. 190) for a discussion of references where sedimentation influenced restructuring).

Similar observations were made for all three samples of 0.05, 0.1, and 0.3 M KCl solutions as in Figure 6.2 for 1M KCl. Rather than presenting the scattering profiles of these solutions, results were combined as a single plot in Figure 6.3. The gradual increase in D_f with KCl concentration found from the slope of fractal scattering region by making a linear fit on the same incremental data points between θ=7°-12° can be seen in Figure 6.3.b. The highest fractal dimension of D_f ~ 2.90 is already reached for 0.3 M KCl solution indicating an upper limit for electrolyte concentration to achieve the highest D_f. The error bars are provided as a general guide and correspond to the extrema in the range of possible slopes that are determined through a linear fit in the linear portion of the scattered intensity profiles (i.e., by choosing different lower and upper limits of scattering angles). As explained before, there is a wide linear region in the figures in the incremental measurements that we can confine the fractal analysis to regions away from the onset of the Porod ripples and the Guinier scattering region and present the corresponding D_f values with a high level of confidence. As seen in Figure 6.3.a the addition of even the lowest KCl concentration increased the forward scattering intensity considerably (I_{vv}=17.1 to 23.3, for [KCl]=0 M to 0.05 M, respectively). The intensities (aggregate size) increased only moderately with further increases in electrolyte concentration. The error bars on incremental scattered intensity measurements show the actual spread of the readings at each point around an arithmetic mean (100 measurements). Forward scattering intensities at θ=3° and D_f values of the findings with electrolyte addition are also tabulated in Table 6.2.

The observed increase in fractal dimension with electrolyte concentration for the WO_3 nanowires presents a stark contradiction to the observations reported in the literature. At low electrolyte concentrations the aggregation reaction is completed in extended periods of time, and primary particles can diffuse further into the aggregate to form compact aggregates of high D_f, whereas diffusion limited (fast aggregation) reaction induced by high electrolyte concentration results in lower D_f. However, the observation is similar to that reported by Dr Sunkara's group for increased ion concentration in the solution due to very low or very high pH, in which the decrease in Debye length has facilitated the fast

aggregation and a subsequent sedimentation. The apparent departure from the behavior previously observed for spherical primary particles *might* also lie in the fact that the lack of rotational symmetry for WO_3 nanowires used in this study could affect the sticking probabilities in different ways, as we now have one dimensional, cylindrical primary particles. This, combined with the high polydispersity of the WO_3 nanowires and unfavorable solvent rheology of water for the WO_3 nanowire dispersions (high fractal dimensions were observed in water even without the addition of an electrolyte as noted in Chapter 5 and [53]) results in considerably compact aggregates with KCl addition.

Although D_f=2.90 was observed as an upper limit, further studies with electrolyte concentration is required to determine fractal dimension limits corresponding to different aggregation behaviors. In particular, electrolyte concentration for which the reversible flocculation (or aggregation) regime turns into irreversible regime (see Chapter 2 and Figure 2.2); and its lower and upper limits for diffusion limited and reaction limited aggregation are not known for the WO_3 nanowires [163]: (p. 4666, and Figure 2).

6.3.3. Change in Aggregate Morphology with Time

(i). High Particles Concentration and Low Salinity (Case A)

The change in scattering behavior and fractal structure due to electrolyte induced aggregation in time was investigated for the WO_3 nanowire suspension of $f_v=1.3\times10^{-6}$ in a 0.1 M KCl de-ionized water solution of pH=3. Figure 6.4 shows the changes during the period of the aggregation process for this solution. As seen in the figure scattered intensity profiles at the initial and final stages, as well as the rest of the scattered intensities at intermediate times, present fractal behaviors. The initial D_f=2.83 found from the slope of the fractal scattering region by making a linear fit on incremental data points between $\theta=7^o$-12^o, decreases to D_f=2.31 at the final stage of the process within ~22 hours when evaluated between the same scattering angles.

The significant shift in I_{vv} versus q profile towards lower intensity values observed in this figure illustrates the significant tendency for sedimentation in the WO_3 suspension even with a moderate salt concentration. The rest of the measurements at smaller times present a behavior similar to the t=0 curve, with intensity profiles shifting towards lower values only slowly up to about the 4 hours mark.

Figure 6.5 illustrates the change in I_{vv} at the forward scattering angles during the entire aggregation process. About 15% of the particulate matter in the form of WO_3 nanowire aggregates have settled down in slightly more than 2 hours (at the t=133 minutes mark) as can be deduced from the intensity data given in Figure 6.5 by assuming a linear dependence of scattered intensity to concentration in the independent scattering regime (recall $I_{vv} \propto n_a$ where n_a is the number density of aggregates in the solution). Rapid aggregation and a consequent rapid sedimentation (due to significant difference in WO_3 and water densities) continues after this point and 66% of the nanowire suspension has sedimented in the end (at t=1302 minutes or after ~22 hours). As a consequence of sedimentation, the typical Tyndall effect (see §2.3.2 for its description) that would result in a parallel shift in I_{vv} in fractal scattering region with time (hence a constant slope) was not observed.

Also shown in Figure 6.5 is the change in D_f with time determined by following the same procedures mentioned above between scattering angles θ=7°-12°. An initial peak to D_f=2.90 within the first 18 minutes gradually decreased to D_f=2.74 at about the 4 hours mark. At this point a significant percentage of the suspension (about 28%) has already settled down, and yet the fractal dimension is quite high indicating highly entangled structure of the remaining aggregates suspended in the solution. D_f=2.31 at the final stage of the process shows that, although the WO_3 aggregates floating in the dispersed phase still form entangled fractal aggregates, they are somewhat more tenuous which possibly results in a higher cross sectional area and a lesser gravitational force helping them to float.

It is interesting to note that the change in D_f followed a somewhat similar trend to that of the change in forward scattering intensity and continued to decrease as time passed, despite minor, erratic increases. This shows that the large aggregates formed in the sample were quite compact and settled first, compared to the smaller and more tenuous aggregates which stayed suspended for longer times.

Results of Figures 6.4 and 6.5 are also summarized in Table 6.3. The suspension was manually stirred after the final measurement at ~22 hours, and a similar measurement was performed on this sample as described above. Scattered intensity and the D_f determined after the suspension was stirred are presented in the same table. Both values increase dramatically compared to the final measurement. D_f=2.86 is almost the same as the initial value of D_f=2.83, however, the forward scattering intensity is not recovered and is lower than its initial value, indicating the breakage of large aggregates that were initially observed due to the shear forces exerted on the aggregates.

(ii). High Particles Concentration and High Salinity (Case B)

A similar study to observe changes in fractal structure and aggregation rate of WO_3 nanowires was made under the same conditions of $f_v=1.3\times10^{-6}$ and pH=3, but with a higher salt concentration of 0.5 M KCl in de-ionized water two days after the measurements presented in Figure 6.4. Figure 6.6 shows the change in scattering profile of this sample between its initial and final states in a ~26 hours observation period.

As seen in Figure 6.6, when the electrolyte concentration was increased the shift in I_{vv} versus q profile for the final state compared to the initial was even more severe. This illustrates the increased tendency for aggregation and for the consequent sedimentation in the WO_3 sample with 0.5 M KCl concentration, more so than with the 0.1 M KCl solution. The measurements given in Figure 6.6 were performed two days after than those presented in Figure 6.4, hence correspond to a somewhat different initial structure of WO_3 nanowire aggregates. As a result, an initial scattering exponent of SE=3.30 was found from the slope of the fractal scattering region from a linear fit on incremental data

points between θ=7°-12°, which decreased to D_f=2.16 at the final stage of the process after 24 hours between the same scattering angles. Again, no Tyndall effect was observed due to significant sedimentation.

The additional shelf time of only few days resulting in an increased *SE* for *bundled* nanowires is in line with the observations made in Chapter 5 (see Table 5.1) and in [53]. However, the scattering exponents in the presumed fractal scattering region at the initial state is beyond the physical limit of fractal dimension D_f=3 which is realized for a sphere. This, however, is unlike the case studied in Chapter 4 and in [146] where the primary particles in the shape of thin, but long "single" WO_3 nanowires had comparable length scales with the wavelength of incident light (i.e., high size parameter, x), which resulted in scattering exponents much greater than 3. Observations made in Figure 6.6, therefore, are the result of rapid aggregation in a highly polydisperse suspension made up of shorter and "bundled" primary particles which intrinsically present some surface roughness (see SEM images in Chapter 5). In the case of rough surfaced aggregates, scattering exponent lies between $3 \leq SE \leq 4$ as was also experimentally observed by [93] in KCl induced aggregation of hematite spheres, and is the most plausible reason for the high *SE* values in Figure 6.6.

The migration of the Porod regime towards smaller q values is another important observation in Figure 6.6 when compared to Figure 6.4, which was shown to be as a result of the non-linear contribution to fractal scattering by larger primary particles spread out in a matrix of smaller primary particles forming a fractal aggregate [110]: (p. 6), as a result of the faster aggregation due to the higher electrolyte concentration (as detailed in Chapter 2).

Figure 6.7 illustrates the change in I_{vv} at the forward scattering angles during the entire aggregation process. More than 11% of the particulate matter in the form of WO_3 nanowire aggregates have settled down within an hour (at the t=46 minute mark), and 33% in slightly more than two hours (at the t=133 minute mark)—more than double the amount that settled at the same observation time for the case of low salinity shown in

Figure 6.5. 83% of the WO_3 nanowires initially suspended have sedimented in the end (at t=1538 minutes, i.e., ~26 hours).

The change in scattering exponent with time is also shown in Figure 6.7 which was determined by following the same procedures mentioned above between scattering angles θ=7°-12°. The change in *SE* follows a somewhat similar trend to that of the change in forward scattering intensity, again with minor, occasional increases. An initial value of *SE*=3.30 gradually decreased to D_f=2.98 only at the ~4 hours mark. Although D_f=2.16 at the final stage of the process for the 0.5 M KCl solution is smaller than the value obtained at the end of the aggregation process for the 0.1 M KCl solution, a linear interpolation on the experimental data of the 0.5 M KCl solution would give almost exactly the *same* fractal dimension of D_f=2.32 at the same observation time (~22 hours) at the end of the process for the 0.1 M KCl solution. A further decrease in the fractal dimension of WO_3 aggregates floating in the suspension should be expected if the measurements were continued without disturbing the suspension.

When the suspension was stirred mechanically the forward scattering intensity and the D_f increased dramatically. However, the initial values are not recovered. The lower forward scattering intensity shows that aggregates that are smaller than initially observed were present in the sample after stirring, which should have been produced by breakage with the stirring. The surface fractal dimensions D_s corresponding to measurements with D_f>3 along with results from Figure 6.7 are presented in Table 6.4.

(iii). Low Particles Concentration and High Salinity (Case C)

The final study to observe changes in fractal structure and aggregation rate of WO_3 nanowires was made under the same conditions and on the same day, concurrently with the measurements presented in Figures 6.6 and 6.7, but with a lower WO_3 nanowire content of f_v=0.7×10^{-6}. Figure 6.8 shows the change in scattering profile of this sample between its initial state and during a ~24 hour observation period. Since the measurements were done concurrently with the 0.5 M KCl, f_v=1.3×10^{-6} solution, any

difference in observed behaviors are due solely to the difference in volume fractions and not the initial aggregate structures.

The rapid shift in scattered intensity curve within the first 4 hours, which is very close to the final scattered intensity curve after ~24 hours, is the most striking difference between the two measurements. Considering the number of particles is much less in the $f_v=0.7\times10^{-6}$ solution compared to the $f_v=1.3\times10^{-6}$ solution with the same 0.5 M KCl concentration, the reaction probability between WO_3 nanowires in the suspension is decreased. As discussed earlier, it is known that with higher particle concentration the primary particles can diffuse further into the branches of the aggregate producing more compact structures of high fractal dimensions (see also Table 6.1). As a result of lower particle concentration, more linear aggregates have formed (as if for the fast reaction) as seen from SE=3.20 in Figure 6.8 at the onset of aggregation which is lower than the corresponding value in Figure 6.6. Slower aggregation rate (higher D_f) with higher particle concentrations and stronger bonds with higher D_f are in line with previous observations in the literature [157]. The fractal dimension D_f=1.38 reported at the end of the 24 hour process is only symbolic, since a fractal behavior is not observed for the sample at this stage anymore. Again, the Tyndall effect was not observed.

Fractal dimension throughout the aggregation process of the lower f_v solution given in Figure 6.9 is lower compared to those in Figure 6.7. As seen in Figure 6.9, with the volume fraction halved to $f_v=0.7\times10^{-6}$, the initial intensity (I_{vv}=18.4) is also almost halved compared to the measurements performed on the $f_v=1.3\times10^{-6}$ solution (I_{vv}=32.4) given in Figure 6.7, in line with independent scattering theory. The faster sedimentation can be quantified if we compare the 28% reduction in forward scattering intensity at the 46 minutes mark for low particles concentration in Figure 6.9 to the 11% reduction for the high particles concentration that was reported in Figure 6.7 at the same observation time and with the same degree of salinity. The same amount of KCl has more ionic concentration per nanowire now to accelerate the aggregation and the consequent sedimentation (the same effect if the electrolyte concentration were to be increased, keeping the f_v the same).

After the suspension was stirred manually the forward scattering intensity and fractal dimension both increased, but not to the extent that the initial values were obtained. The lower forward scattering intensity and D_f after stirring indicates that the linear, tenuous aggregates broke down to form smaller and less compact aggregates compared to those initially observed in the process. These and other results given in Figures 6.8 and 6.9 are presented in Table 6.5.

Figure 6.10.a compares the time rate of change in scattered intensities at θ=3^o (rate of depletion in the dispersed phase) for the three cases studied above (i.e., $rate = (I_{vv}(t) - I_{vv}(t_o))/(t - t_o)$). Recall that, as a consequence of independent scattering, the scattered intensity is proportional to the number of colloidal particles in the system. As seen in Figure 6.10.a the *fastest* reduction in the number of suspended particles (WO_3 nanowires and their aggregates) occurs within the first 50 minutes in all three cases. Case B and C (both are in a 0.5 M KCl solution) have about the same absolute value of highest sedimentation rates, and have a greater value than for Case A (0.1 M KCl). Sedimentation continues at a finite rate after this time, though with a progressively lower vigor. Note, however, that the particle concentrations are not kept constant for all three cases. It appears that by keeping the particle concentration between Cases A and B, a high sedimentation rate can be reached with an increased electrolyte concentration (no surprise there). However, at the same high electrolyte concentration (0.5 M KCl) the maximum rate of sedimentation that can be attained is the same (-0.113 1/s) for Cases B and C, and there is no change due to particle concentration.

A useful way of assessing the effect of KCl concentration on the electrolyte facilitated sedimentation behaviors can be to compare the relative change in scattered intensities in time (i.e., $rel.\ rate = (I_{vv}(t) - I_{vv}(t_o))/(I_{vv}(t_o)(t - t_o))$). By performing a normalization with the intensity value at the onset of sedimentation as in Figure 6.10.b, in effect, we isolate the effect of particle concentration on the scattered intensities, thus on the sedimentation rates. This amounts to claiming that the rate of depletion in dispersed phase can be estimated by observing electrolyte concentration relative to the particles

concentration, or using the ratio [KCl]/f_v. The [KCl]/f_v ratio is 0.8×10^5, 3.8×10^5, and 7.1×10^5 for Case A, B, and C, respectively. Further studies are required to check the validity of this observation. A semi-log plot of change of this ratio with time shows that the curves shift down in the same order as Case A, B, and C.

6.4. SUMMARY

We have shown quantitatively that adjusting the electrolyte concentration at a constant solution pH could affect the sedimentation of suspensions of WO_3 nanowire aggregates by means of altering the reaction rate and influencing the fractal structure (D_f) along the way.

The addition of KCl results in an immediate increase in I_{vv} in forward scattering angles, and a rapid transition from Guinier to fractal scattering region. Aggregation of WO_3 nanowires in water was aggravated by even the slightest addition salt (0.05 M KCl), and the resulting increased forward scattering was accompanied by decreased side scattering due to the larger particles formed, which also resulted in compact aggregate morphologies with high D_f as the KCl concentration increased. The compactness of WO_3 nanowire aggregates without an electrolyte ($D_f \sim 2.7$), increased further and reached to $D_f \sim 2.9$ with the increase in solution salinity to 0.3 M KCl, after which point remained constant up to 1 M of KCl in the solution.

Considering the rapid increase in forward scattering intensities with even 0.05 M KCl, the electrolyte concentration should be lowered if the aggregation mechanisms of diffusion limited and reaction limited conditions were to be investigated thoroughly—perhaps similar to the KCl concentration ranges of 0.003-0.080 M of KCl used in [93]. However, the nature of the particle-type—electrolyte-type interaction should also be taken into consideration and other electrolytes should also be tried [158] (e.g., as summarized in Table 6.1).

The three samples on which the sedimentation experiments were performed over a one day period were categorized as high particles concentration-low salinity (Case A: f_v=1.3×10^{-6} with 0.1 M KCl), high particles concentration-high salinity (Case B: f_v=1.3×10^{-6} with 0.5 M KCl), and low particles concentration-high salinity (Case C: f_v=0.7×10^{-6} with 0.5 M KCl).

Increase in the spatial extent (R_g) of the aggregates combined with the fact that density of WO_3 is substantially higher than that of water resulted in high sedimentation rates observed through the decrease in forward scattering intensities. Within the first 46 minutes of the onset of aggregation, the 10% sedimentation (by interpolation) of the high particles concentration sample (Case A) is observed, which is surpassed by the 11% sedimentation of a similar sample but with higher KCl concentration (Case B). When the particles concentration was halved at the high KCl level (Case C), the amount of sedimentation reached 28%. The same trend was observed at the 133 minutes of reaction with 15% sedimentation percentage increasing to 33% and 48% (by interpolation) for the same three samples studied, respectively. These observations are in line with previous finding in the literature that the increase in ionic strength of the solution *keeping* the particles concentration the same would increase the aggregation rate (and in the case of WO_3 nanowires the sedimentation rate, as well). An interesting observation is that the relative concentration of electrolyte with respect to particle concentration could be used to approximate the sedimentation rates: the rate of depletion in the dispersed phase follows the order of A<B<C, in line with [KCl]/f_v ratio values (0.8×10^5, 3.8×10^5, and 7.1×10^5, respectively).

The fractal dimensions of the three cases mentioned above, increased from D_f=2.83 at the onset of aggregation for the first sample (Case A) to beyond the limit D_f=3 for Case B and C, as the ionic strength relative to particles concentration increased. For these samples the high ionic strength caused highly entangled aggregates and the scattering from the aggregate surface resulted in surface fractals due to the surface roughness of primary particles which look like “bundled” nanowires, with *SE*=3.30 (Case B) and *SE*=3.20 (Case C) at the onset of aggregation. Comparing the intensities with same

particles concentrations (Case A and B) at forward scattering angles (and throughout the range of measurements) the increase in size with high salinity is also observed (e.g., I_{vv}=22.9 as opposed to I_{vv}=32.4 at θ=3^{o}, for Case A and B, respectively).

The fractal dimensions decreased for all three samples when observed over the 24 hour aggregation process, indicating that the dispersed nanowires floating in the suspension were more open structures than the sedimented aggregates. The aggregates floating in the dispersed phase still formed substantially entangled aggregates with high D_f values, although more tenuous in fractal structure. Their tenuous structure might have resulted in a lesser gravitational force due to higher cross sectional areas and help them to float.

The compact aggregates at the end of the aggregation processes are not strongly attached that after agitating the suspension through manual stirring, the broken aggregates are somewhat smaller in size (deduced by observing their I_{vv} at forward scattering angles at the onset of aggregation and after manually stirring), though still with considerably compact structures (i.e., comparably high D_f values).

It has been shown in Chapter 5 that the low aspect ratio, "bundled" WO_3 nanowires have a high tendency to aggregate, especially when suspended in water. Strictly speaking, the WO_3 nanowires have already aggregated to some extent at the onset of measurements and have a considerably high D_f even before their dilution in the electrolyte solution. Ultrasonication of these samples in an attempt to re-disperse the nanowires was avoided as it may result in breakage of the individual nanowires, and complicate the aggregate structures by increasing the polydispersity in size distribution [53, 156]. Therefore, we do not claim a thorough analysis of electrolyte induced aggregation of primary particles of cylindrical geometry. Such an analysis would require a better classification of the products of the nanowire synthesis from the chemical vapor deposition process so that the primary particles are well defined in *size* and in *shape*.

The information presented in this chapter could prove useful in understanding aggregation rates and the resulting aggregate structures from primary particles in the form

of nanowires in saline solutions (or other solvents besides water). Such information has the potential of solving problems encountered in handling these nanowires samples such as determining the optimum storage concentrations, but also can provide new possibilities in waste water treatment, e.g., by using nanowires for contaminant removal due to their high settling tendency, and in determining filtration requirements in separation processes where separation efficiency is strongly influenced by the structure of the aggregates, in addition to other uses in biological sciences.

Table 6.1. Parameters that affect aggregation and a summary of *sample* outcomes.

Parameter	Particles	Electrolyte	pH	Comparative Observations
Shear	SiO_2 unknown diameter	1 M NaCl	8.5, 9.6	Shaking the samples *v*. swirling were qualitatively determined to cause a greater increase in D_f due to restructuring [61].
Electrolyte-particle interaction	Hematite 70 nm diameter	50-80 mM KCl	3	10 times the KCl concentration required to aggregate hematite [93] was used to initiate aggregation of γ-alumina [158]. Minute amounts of Na_2SO_4 would suffice to start aggregation of γ-alumina [158], similar to the small amount of KCl required for hematite.
	γ-Alumina 20 nm diameter	0.5-0.9 M KCl or NaCl	4.5	
		0.1-0.3 mM Na_2SO_4		
Solution ionic strength	γ-Alumina 20 nm diameter	0.2-0.6 M $CaCl_2$	4.5	The same Cl^- concentration from $CaCl_2$ [158, 160] was required to start γ-alumina aggregation as from NaCl or KCl [158].
Acidity, pH	SiO_2 unknown [61], 22 nm [157] diameter	1 M NaCl	8.5, 9.6 [61], 6.7, 8.6 [157]	D_f=1.97 decreased to 1.78 as pH increased [61], which also agreed with the decrease from D_f=2.11 to 1.75 [157].
Surface treatment	Hematite 70 nm diameter	3-50 mM KCl	3	Particles treated with fulvic acid result in even more compact aggregates [93], surface roughness yield *SE*>3 at lower KCl limit (slow aggregation)
Particle concentration	SiO_2 unknown [61], 22 nm [157] diameter	1 M NaCl	8.5, 9.6 [61], ~7.5 [157]	Particle concentration increase between 0.00025-0.01 wt% resulted in an aggregation rate decrease, and D_f ~ 1.73 increased to ~1.97 at e.g., pH=8.5 [61]. Similarly, a fast aggregation rate caused restructuring as the particle concentration varied between 0.0001-0.008 wt%, and D_f ~ 1.75 increased to ~2.1 [157]. Further increase in particle concentration between 0.008-0.6 wt% resulted in slow aggregation rates and high D_f ~ 2.1 [157].

Table 6.2. Effect of [KCl] concentration on fractal dimensions of 2 μm "bundled" WO_3 nanowire aggregates under electrolyte induced aggregation conditions.

[KCl], M	Acidity, pH	D_f (θ=5°-10°)	D_f (θ=4°-12°)	I_{vv} [arb. units]
0	No HCl	2.89	2.82	24.4
0	3	2.73	2.64	17.1
0.05	3	2.78	2.72	23.3
0.1	3	2.83	2.77	21.4
0.3	3	2.90	2.80	23.2
1	3	2.90	2.79	22.4

Table 6.3. Change in suspension of 2 μm "bundled" WO_3 nanowire aggregates with time (Case A: under electrolyte induced aggregation conditions in a DI-water solution with f_v=1.3×10^{-6}, [KCl]=0.1 M, pH=3.) Measurements are on the same day as those in Table 1. (*After suspension was mechanically stirred. +Interpolation, not an actual measurement.)

Time, min	I_{vv} [arb. units]	% Reduc. in *Ivv*	Rate of Depletion [1/min]	D_f
1	22.9	0.0	0	2.83
18	22.5	1.7	-0.0235	2.90
34	20.6	10.0	-0.0697	2.73
46^{+}	*20.7*$^{+}$	*9.6*$^{+}$	*-0.0489*$^{+}$	*2.77*$^{+}$
71	20.9	8.7	-0.0286	2.84
133	19.5	14.8	-0.0258	2.74
224	16.4	28.4	-0.0291	2.74
1302	7.9	65.5	-0.0115	2.31
1319*	17.5*	23.6	-	2.86*

Table 6.4. Change in suspension of 2 μm "bundled" WO_3 nanowire aggregates with time (Case B: under electrolyte induced aggregation conditions in a DI-water solution with f_v=1.3×10^{-6}, [KCl]=0.5 M, pH=3.) Measurements are 2 days after those given in Table 1. (*After suspension was mechanically stirred. +Interpolation, not an actual measurement.)

Time, min	I_{vv} [arb. units]	% Reduc. in I_{vv}	Rate of Depletion [1/min]	D_f (or *SE*)	D_s
1	32.4	0.0	0	3.30	2.70
15	30.9	4.6	-0.1071	3.23	2.77
31	29.0	10.5	-0.1133	3.18	2.82
46	28.7	11.4	-0.0822	3.18	2.82
96	24.3	25.0	-0.0853	3.20	2.80
133	21.7	33.0	-0.0811	3.14	2.86
198	18.3	43.5	-0.0716	3.18	2.82
257	16.5	49.1	-0.0621	2.98	-
334	13.9	57.1	-0.0556	2.91	-
411	12.0	63.0	-0.0498	2.94	-
1302^{+}	*6.9*$^{+}$	*78.7*$^{+}$	*-0.0196*$^{+}$	*2.32*$^{+}$	-
1538	5.5	83.0	-0.0175	2.16	-
1566*	24.5*	24.4	-	3.13*	2.87*

Table 6.5. Change in suspension of 2 μm "bundled" WO_3 nanowire aggregates with time (Case C: under electrolyte induced aggregation conditions in a DI-water solution with f_v=0.7×10^{-6}, [KCl]=0.5 M, pH=3.) Measurements are 2 days after those given in Table 1. (*After suspension was mechanically stirred. +Interpolation, not an actual measurement.)

Time, min	I_{vv} [arb. units]	% Reduc. in I_{vv}	Rate of Depletion [1/min]	D_f (or *SE*)	D_s
1	18.4	0.0	0	3.20	2.80
16	17.7	3.8	-0.0467	2.85	-
46	13.3	27.7	-0.1133	2.99	-
67	12.1	34.2	-0.0955	2.65	-
114	10.0	45.7	-0.0743	2.64	-
133^{+}	*9.5*$^{+}$	*48.4*$^{+}$	*-0.0674*$^{+}$	*2.28*$^{+}$	-
187	8.1	56.0	-0.0554	2.40	-
226	7.3	60.3	-0.0493	2.34	-
1302^{+}	*5.9*$^{+}$	*67.9*$^{+}$	*-0.0096*$^{+}$	*1.48*$^{+}$	-
1423	5.7	69.0	-0.0089	1.38	-
1439*	15.5*	15.8	-	2.70*	-

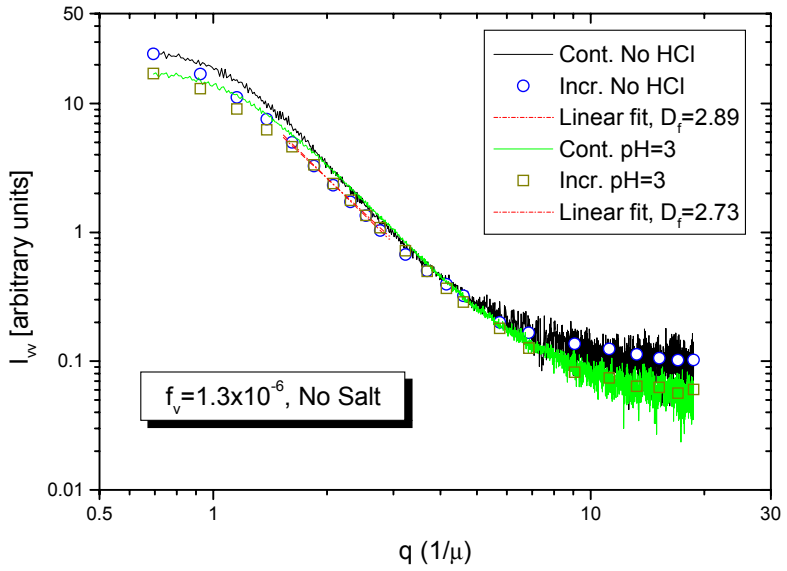

Figure 6.1. Effect of acidity on 2 μm average length WO_3 nanowire aggregates in DI-water with f_v=1.3×10^{-6}. Measurements are between θ=3°-90°, linear fits between θ=7°-12°.

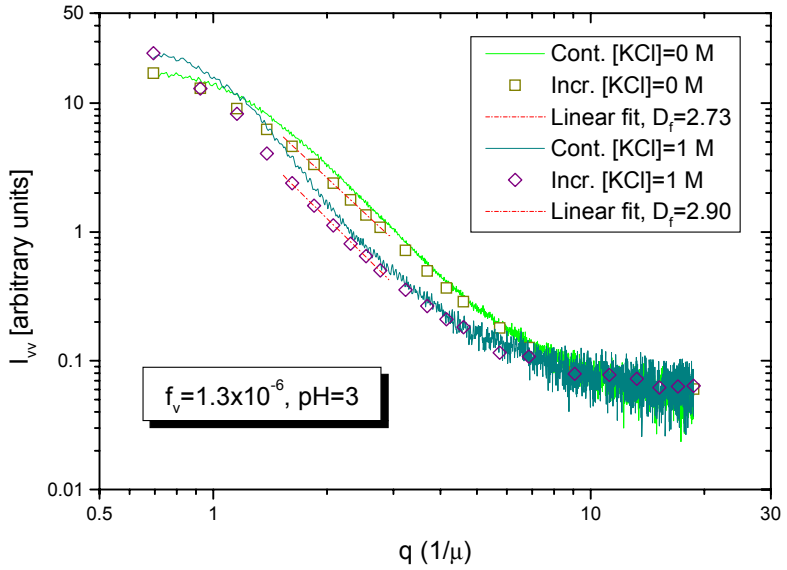

Figure 6.2. Effect of electrolyte addition on 2 μm average length WO_3 nanowire aggregates in pH=3 DI-water. Measurements are between θ=3°-90°, linear fits between θ=7°-12°.

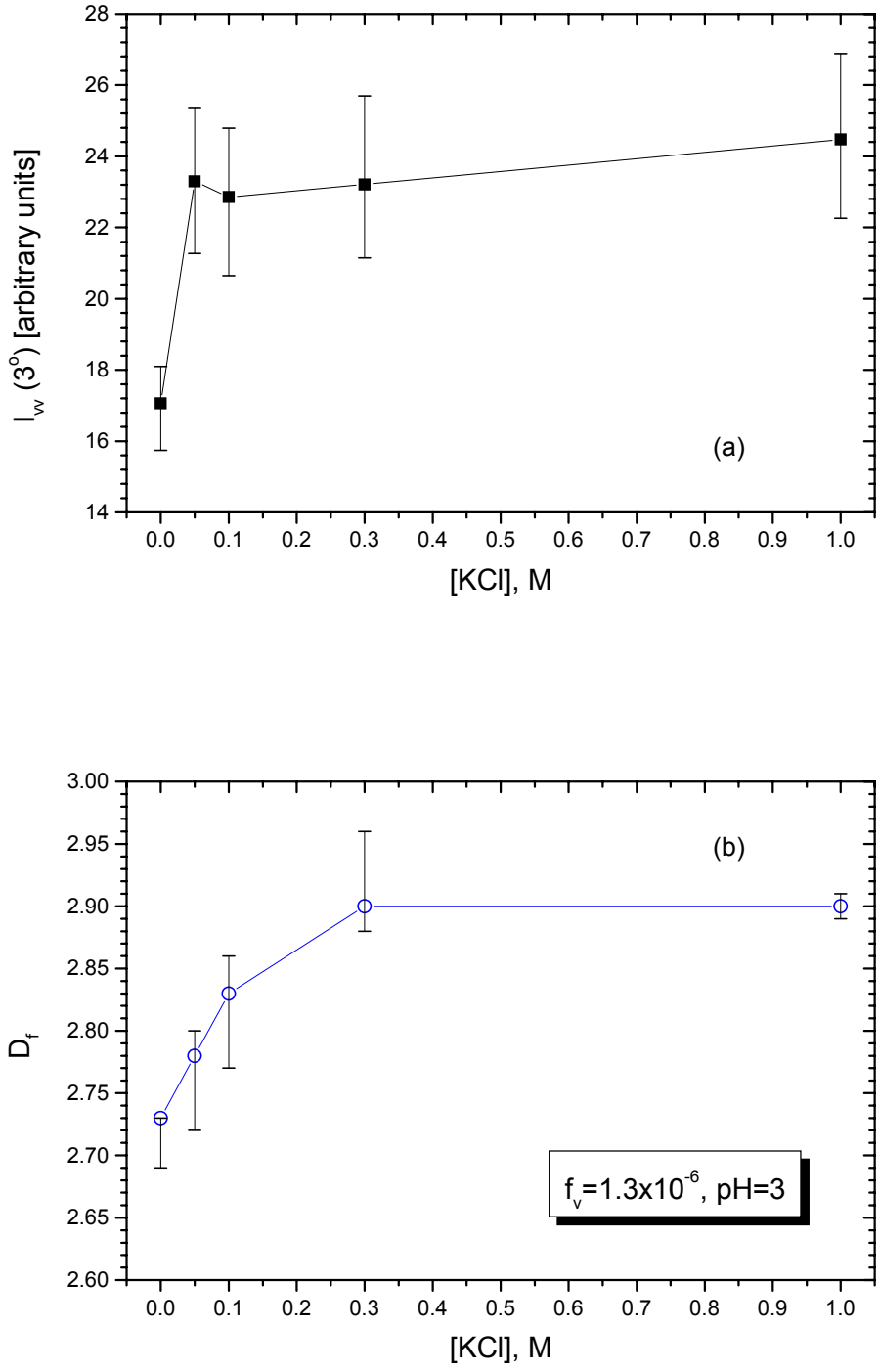

Figure 6.3. Effect of electrolyte addition on fractal dimension of 2 µm average length WO_3 nanowire aggregates in pH=3 DI-water solution (a) Scattered intensity at forward angles (b) Fractal dimension.

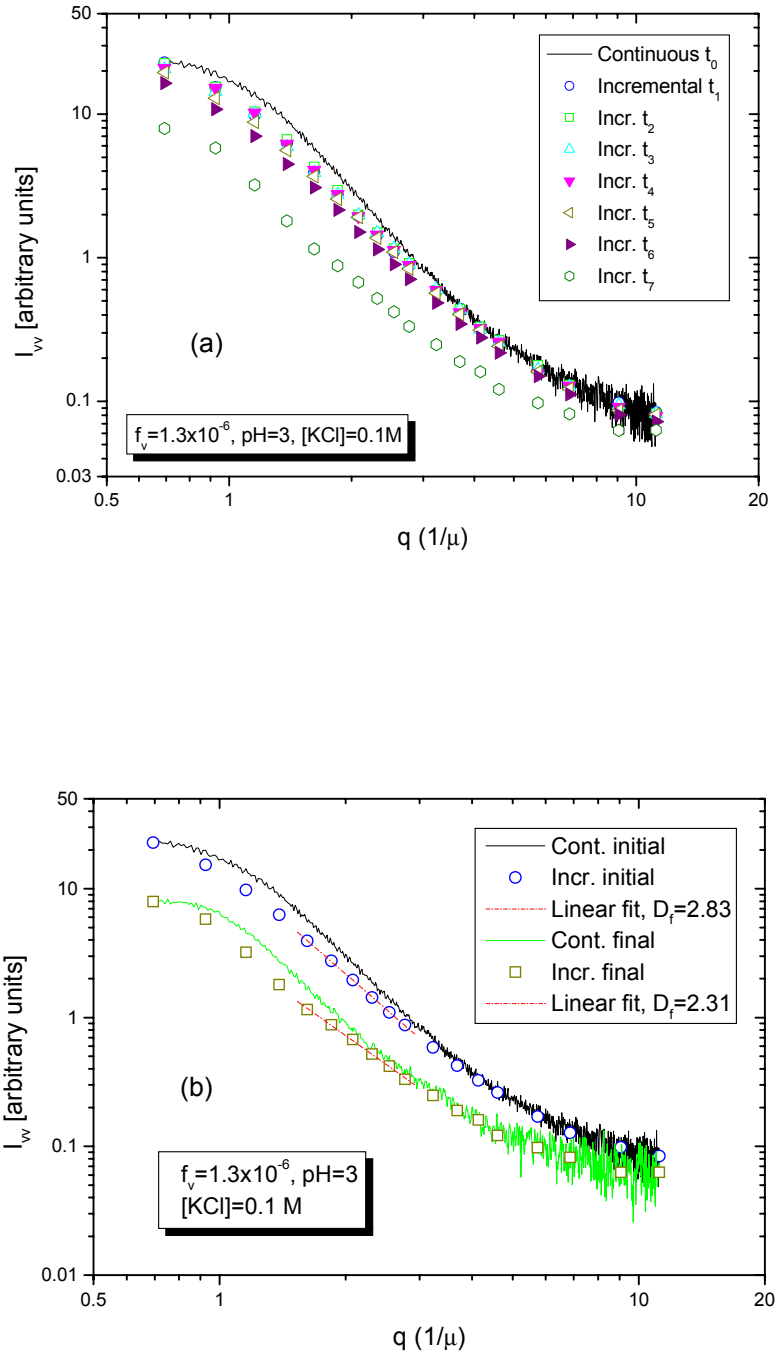

Figure 6.4. Change in scattered intensity profile over a ~22 hour period (21h 42min) for 2 μm WO_3 aggregates (Case A: in a DI-water solution with f_v=1.3×10^{-6}, [KCl]=0.1 M and pH=3.) All measurements are between θ=3^o-50^o, linear fits between θ=5^o-10^o. Continuous measurements were done in 94 seconds, and are average of two runs.

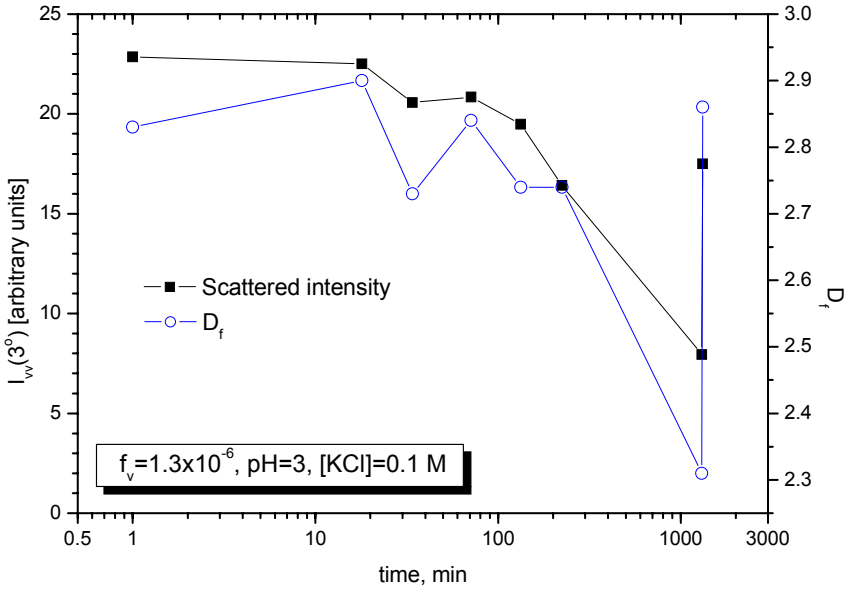

Figure 6.5. Change in forward scattering intensity and D_f with time for 2 μm WO_3 aggregates (Case A: in a DI-water solution with f_v=1.3×10^{-6}, [KCl]=0.1 M and pH=3.)

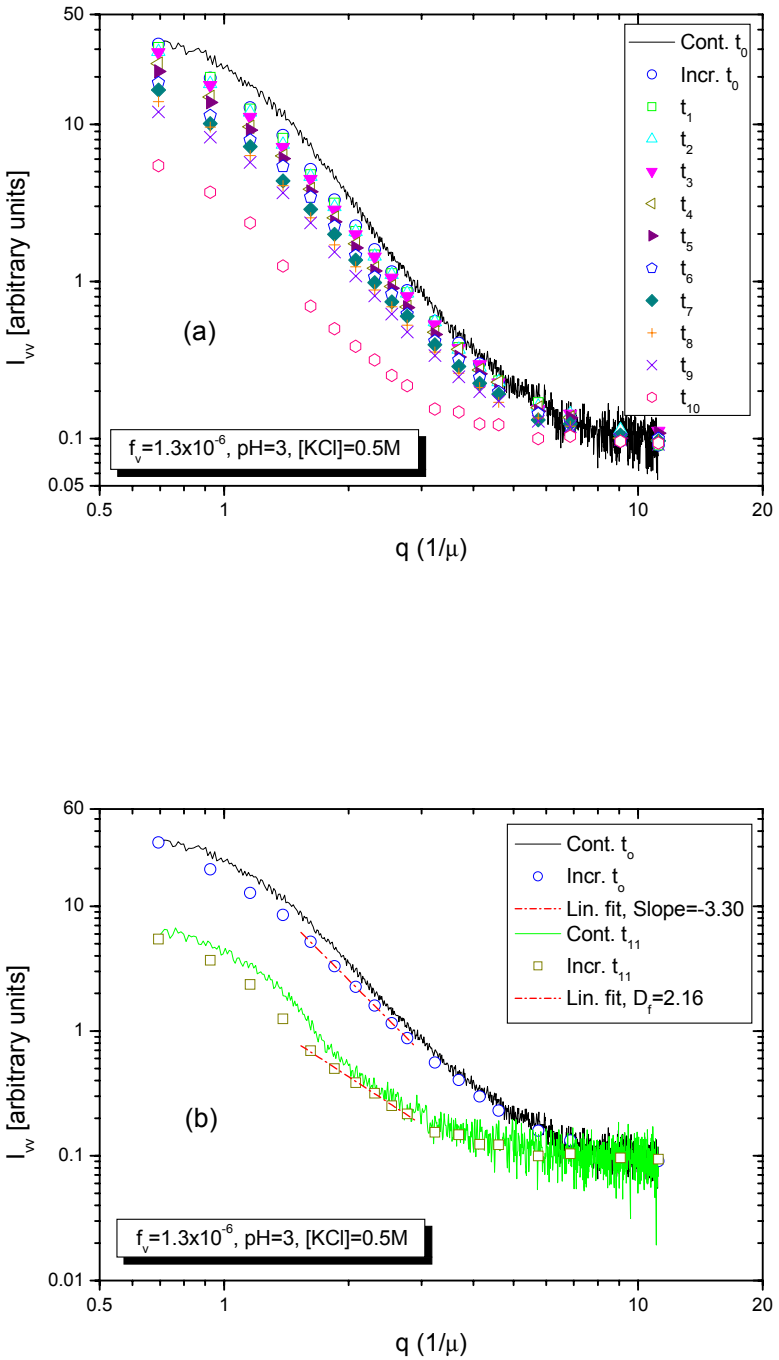

Figure 6.6. Change in scattered intensity profile over a ~26 hour period (25h 38min) for 2 μm WO_3 aggregates (Case B: in a DI-water solution with f_v=1.3×10^{-6}, [KCl]=0.5 M and pH=3. All measurements are between θ=3^o-50^o, linear fits between θ=7^o-12^o.) Continuous measurements were done in 94 seconds, and are average of two runs.

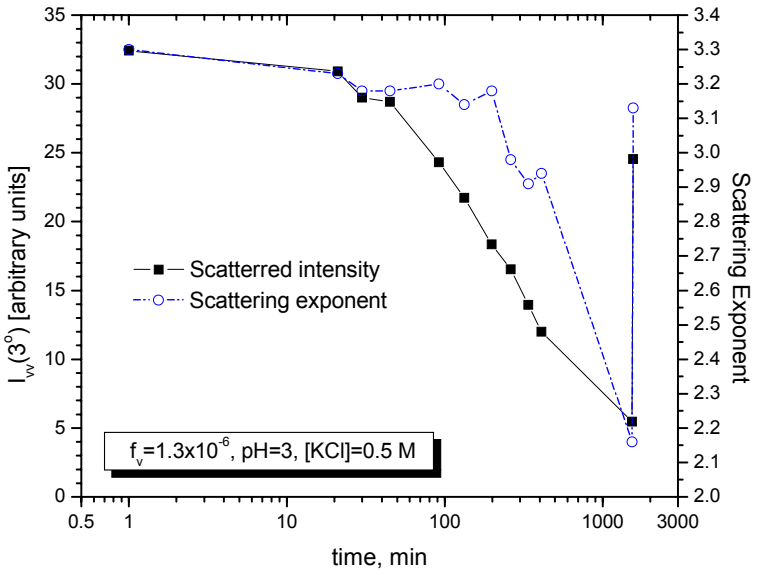

Figure 6.7. Change in forward scattering intensity and scattering exponent (slope in fractal scattering region) with time for 2 μm WO_3 aggregates (Case B: in a DI-water solution with f_v=1.3×10^{-6}, [KCl]=0.5 M and pH=3.

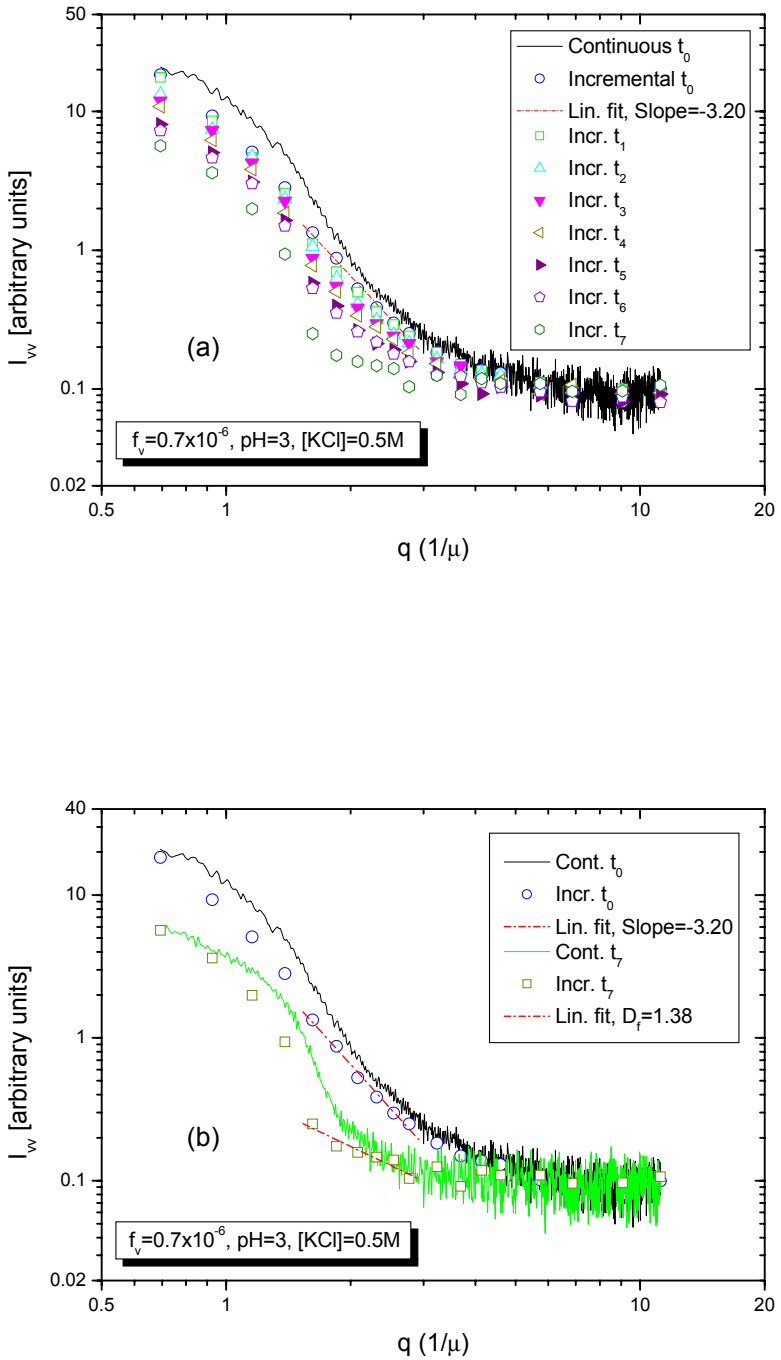

Figure 6.8. Change in scattered intensity profile over a ~24 hour period (23h 43min) for 2 μm WO_3 aggregates (Case C: in a DI-water solution with f_v=0.7×10^{-6}, [KCl]=0.5 M and pH=3.) All measurements are between θ=3^o-50^o, linear fits between θ=7^o-12^o. Continuous measurements were done in 94 seconds, and are average of two runs.

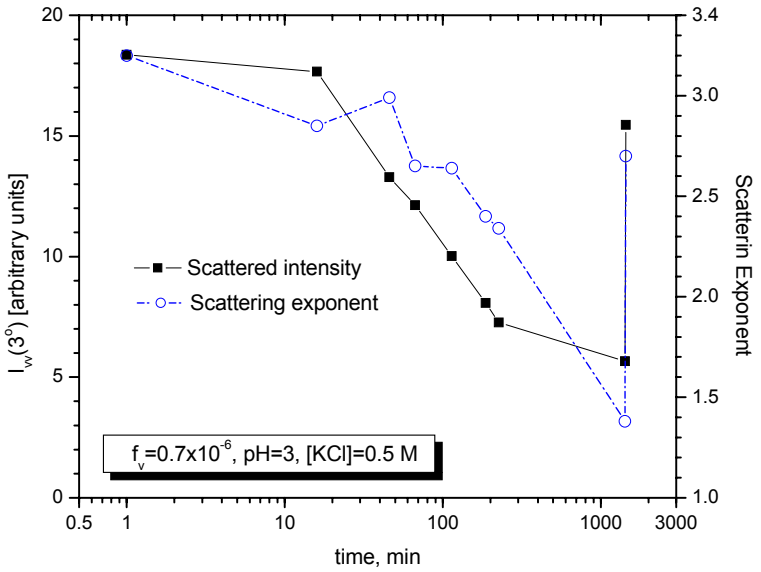

Figure 6.9. Change in forward scattering intensity and scattering exponent (slope in fractal scattering region) with time for 2 μm WO_3 aggregates (Case C: in a DI-water solution with f_v=0.7×10^{-6}, [KCl]=0.5 M and pH=3.)

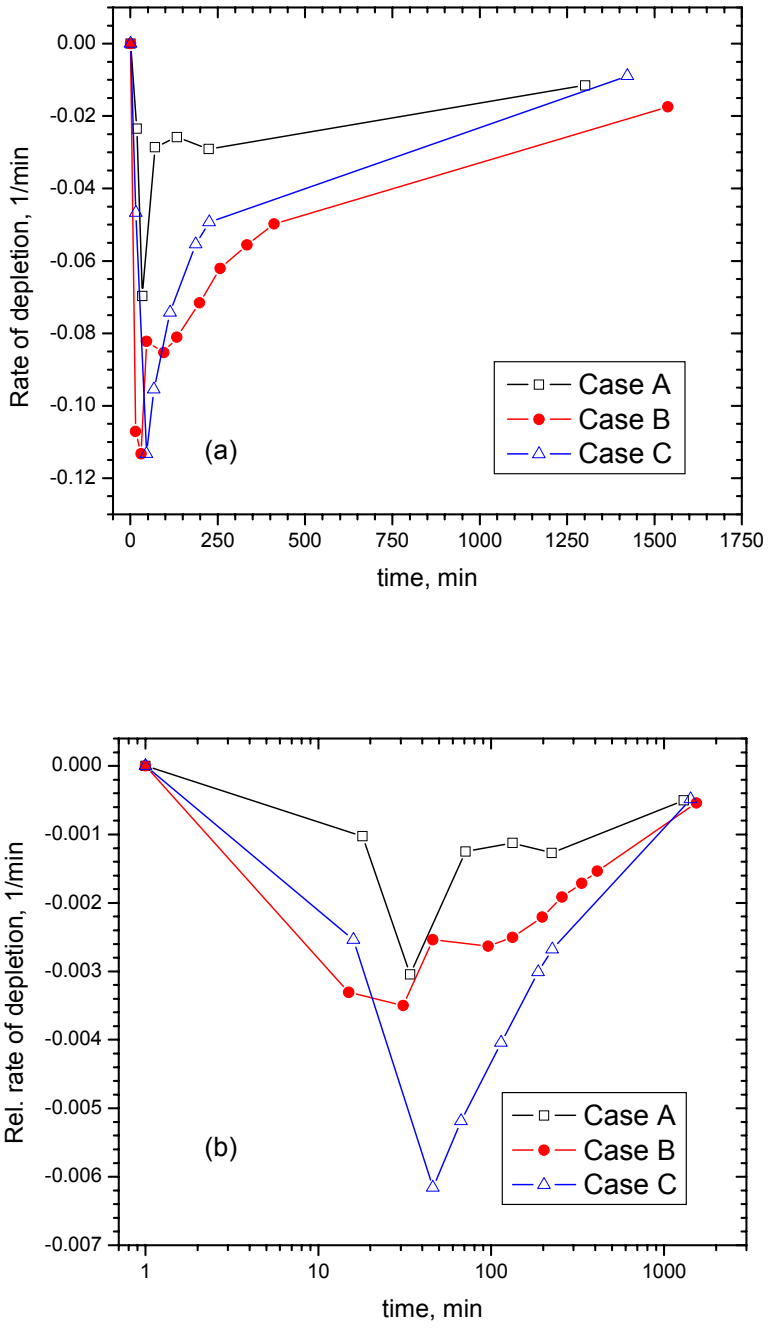

Figure 6.10.(a). Sedimentation rate of 2 μm WO_3 nanowire aggregates under various conditions. particle concentration. (b) Normalized sedimentation rates. (in a DI-water solution with pH=3 and Case A: f_v=1.3×10^{-6}, [KCl]=0.1 M, Case B: f_v=1.3×10^{-6}, [KCl]=0.5 M, Case C: f_v=0.7×10^{-6}, [KCl]=0.5 M.)

CHAPTER 7

CONCLUDING REMARKS

7.1. SUMMATION

Colloidal particles in nanometer scale with various geometric shapes, structures, and equally diverse behaviors present unique opportunities as well as challenges in nanotechnology. These materials have potential applications across multiple disciplines provided that the geometries are well characterized and their aggregation patterns in solutions are well understood, which demand observation and control in real time. Among several techniques available for characterization of nanoparticles and their aggregates, light scattering stands out as an accurate, rapid, non-intrusive and in-situ method, and is anticipated to gain increasing attention.

In this study, we provided a thorough light scattering analysis of the effect of geometry of nanoparticles and solution properties on colloidal stability, aggregation patterns, aggregation rates, and morphology of resulting structures formed in various commonly used polar solvents without the use of dispersants. The effects of low solution pH and electrolyte concentration in the solution on degree of aggregation and its change in time were also investigated.

Colloidal nanoparticles made of tungsten trioxide (WO_3) in the shape of spherical nanoparticles (D~40 nm) and nanowires of different aspect ratios (2, 4, 6, and 10 μm nominal lengths, with nominal diameters of 40, 100, or 200 nm) dispersed in solvents (water; acetone; isopropanol, or IPA for short; ethanol, or EtOH; 1-methoxy-2-propanol, or 1M2P; and N,N-dimethylformamide, or DMF) without dispersing agents were investigated by means of fractal theory using the small angle light scattering and the elliptically polarized light scattering (EPLS) techniques. Vertically polarized incident and

scattered light intensities (I_{vv}) as part of the small angle light scattering technique, and scattering matrix elements (S_{ij}) as part of the elliptically polarized light scattering technique were used to determine spatial extent (radius of gyration, R_g) and fractal dimension (D_f) of the aggregates. Experimental results were also interpreted based on fundamental principles from radiative transfer and Lorenz-Mie theory, utilizing a distilled analysis of available theoretical and experimental results presented in previous studies in the literature.

Although the irregular nanoparticles formed compact aggregates, the nanowires presented diverse behaviors depending on their aspect ratios which resulted in different aggregate morphologies. Nanoparticles invariably formed compact spherical aggregates (D_f~2.6) in ethanol or in acetone, whereas 2 μm nanowires with the lowest aspect ratio (L/D~10, with an uneven ~200 nm diameter) followed a reaction limited (slow) cluster-cluster aggregation mechanism with no discernable change in fractal dimension (D_f~2.1) monitored in an extended period of six months, despite a considerable growth in size (radius of gyration, R_g = 1.8-3.1 μm).

Aggregation of 2 μm nominal length, bundled nanowires with a relatively low aspect ratio (L/D~20, with a 100 nm diameter) monitored through the change in spatial extent of the aggregate was found to be minimal in 1M2P (R_g~1.8-2.2 μm), with a small change in aggregate structure (D_f~1.8 to 1.9) in a time period of six days. The same nanowire sample was found to have the lowest D_f when suspended in DMF (D_f~1.4) which is observed in polarizable clusters indicative of aggregates with a tenuous structure.

For higher aspect ratio nanowires (4, 6, and 10 μm nominal length nanowires with L/D~100, 150, and 250, respectively, all with 40 nm nominal diameter), scattered intensity profiles which migrated towards the Porod regime qualitatively obeyed the Lorenz-Mie theory predictions (Porod limit analogy of the Lorenz-Mie theory). For these nanowire samples of high aspect ratios for which D_f could not directly be inferred from measurements, an analytical and a quasi-experimental method both based on spherical primary particle formulations were used to determine I_{vv} and the D_f, both of which

provided a good approximation of the experimental observations. Analytical methods based on spherical primary particle formulations predicted D_f=1.9, 1.7 and 1.4 for 4, 6, and 10 μm nanowires, respectively. 10 μm nanowires with very high aspect ratio (L/D~250) were observed to form stable dispersions in a time span of six days.

Aggregation of 2 μm WO_3 nanowires (with ~100 nm uneven diameter) in water was aggravated by even the slightest addition of electrolyte (0.05 M KCl) at pH=3, which resulted in very compact aggregate morphologies (D_f~2.7 for [KCl]=0 M to D_f~2.9 for [KCl]=0.3 M), and a subsequent increase in sedimentation (from 66% to 79% in ~22 hours with an increase in [KCl]=0.1 to 0.5 M). Using relative concentration of the electrolyte with respect to particle concentration for Case A<B<C ([KCl]/f_v of 0.8×10^5, 3.8×10^5, and 7.1×10^5, respectively), successfully approximated the overall sedimentation behaviors (rate of depletion in the dispersed phase) which followed the same order.

7.2. FUTURE WORK

Analytical solutions for primary particles in the shape of circular cylinders can be formulated using exact solutions for infinite right circular cylinders [36]: (p. 194-213), or finite cylinders (p. 163-165). Such solutions can either be incorporated into the scattered intensity approximation as the Porod regime formulation (i.e., as an analytical relation for $P(q)$ in the conceptualized for scattered intensity of $I(q)\propto S(q)P(q)$ following §2.3.2 and §2.4 of this dissertation), or simply provide a better approximation than the ripple structure of Lorenz-Mie spheres which was shown to work to some extent to construct an analogy for the Porod regime ripples. Polarization state of the incident light and orientation of the infinite right circular cylinder is important and should be taken into account, e.g., by angular averaging.

Recalling that the use of theoretical formulations—though based on spherical primary particles—was dictated by the high size parameter of individual nanowires comprising the fractal aggregates, certain adjustments in experimental analysis could be made.

Considering the fractal dimension can be experimentally determined for values of q in the $1/R_g<q<1/r_o$ range, the most obvious change in the experimental setup is using a more suitable wavelength of incident light, so that individual particle size parameter is lower, and the linear fractal scattering region in the scattered intensity profile falls between fractal scattering limits. The use of a variable wavelength light scattering setup would be most beneficial in this case, since nanowire dimensions have a wide variance.

Aggregation of WO_3 nanowires is easily induced by minute amounts of KCl in the vicinity of 0.05M. Critical coagulation concentration of the electrolyte (beyond which an increase in electrolyte concentration would not be followed by a corresponding increase in aggregation rate) should be determined more precisely [164]: (p. 15 and Figures A.1 and A.2), [98]: (see their Figure 4). Electrolyte concentration for which the reversible aggregation regime turns into an irreversible regime, and the lower and upper D_f limits of diffusion limited and reaction limited aggregation should be conformed experimentally [163]. Establishment of these limits would provide valuable information on the formation mechanisms of the aggregates under similar conditions in industrial applications.

Numerically generated aggregate structures constructed from cylindrical primary particle geometries could be a simple, yet important addition to the fractal aggregate literature (following §2.5 of this dissertation). Simulations for various aggregation mechanisms based on mimicking algorithms of the Brownian motion of particles in suspensions could provide valuable insight to aggregation kinetics and resulting limits on fractal dimension, just like fractal aggregates constructed with spherical primary particles have done in the past. This also has practical implications since it is difficult to synthesize specific nanowire geometries or to devise experiments that can isolate their aggregation mechanisms experimentally.

There are several possible routes to numerically generate fractal aggregates from cylindrical primary particles. A quick (but inaccurate) way to visualize some features of such aggregates would be using the geometrical centers of spherical primary particles of a fractal aggregate (e.g., from Eden model Version-C). The only difference would be that

a random number generation procedure should be utilized to determine the orientation of the cylinders. The touching points need not be taken into consideration, as monomer sites are only valid for spherical particles anyway, and the resulting structure does not necessarily correspond to a connected fractal aggregate. A more accurate way would be to follow the trajectory of cylindrical primary particles on a cubic lattice (e.g., conforming to a Witten-Sander model), and letting the particle rotate randomly at each step (e.g., by allowing only the six directions of Cartesian coordinates, or a higher number of possible rotation angle on the 4π solid angle), and to let it stick irreversibly to the aggregate upon contact with any of its constituent primary particles, choosing among the possible touching points (e.g., the two tips and the middle, or one of the many possible location on the outer surface). At this stage the question of whether limiting the coordination number (sticking points) to two as in spherical primary particles or more should also be addresses, too. A variant of this model could be rotating the diffusing cylindrical primary particle randomly at its initial step, but then treating the particle as if it has three dimensional symmetry during the entire random walk process (e.g., with no rotation), until it touches any of the constituent monomers of the aggregate. A short pseudo-algorithm that can be used for this purpose is described below:

- Use Cluster-Cluster and Particle-Cluster aggregation models to generate aggregates of cylindrical primary particles.
- Orientation can be fixed with two vectors on the particle coordinates as it is done in DDSCAT [80].
- For the first particle being fired, select from the three Euler angles as in DDSCAT. Add a step, and then determine an angle again.
- The diameter and the length should be taken into account to check if outer walls touch existing cylinders within the aggregate.
- Coordinates can be used to determine D_f from the exponential definition (i.e., using e^{ikr} formulation) as done in for spheres [119].

Scattering matrix elements (S_{ij}) can provide additional information on the shape, size, and size distribution of the primary particles. This is in addition to the fractal structure

information and should be explored in conjunction with spherical particles and nanowires of various dimensions. In particular, certain ranges of the scattering angle in angular scattering matrix element profiles can be more sensitive to geometry (spherical versus cylindrical), dimensions (L/D), or structure (single versus bundled) of the individual nanowire.

REFERENCES

1. Taniguchi, N., *On the Basic Concept of 'Nano-Technology'*, in *Proceedings of the International Conference on Prod. Eng., Part II*. 1974 Society of Precision Engineering: Tokyo, Japan.
2. *Norio Taniguchi:* http://en.wikipedia.org/wiki/Norio_Taniguchi. February 26 2007.
3. *Plenty of Room at the Bottom:* http://www.its.caltech.edu/~feynman/plenty.html. February 26 2007.
4. Feynman, R.P. *There's Plenty of Room at the Bottom: An Invitation to Enter a New Field of Physics*. in *Miniaturization*. 1961. New York: Reinhold.
5. Drexler, K.E., *Nanotechnology: From Feynman to Funding.* Bulletin of Science, Technology and Society, 2004. **24**(1): p. 21-27.
6. *Nanotechnology:* http://en.wikipedia.org. February 14, 2007.
7. Roco, M.C., *Nanotechnology's Future:* http://www.sciam.com/. August, 2006.
8. *Nanoscience & Nanotechnology: Overview*, Pacific Nanotechnology: Santa Clara, CA. p. 1-4.
9. Gates, B.D., Q. Xu, J.C. Love, D.B. Wolfe, and G.M. Whitesides, *Unconventional Nanofabrication.* Annual Review of Material Research, 2004. **34**: p. 339-372.
10. Edelstein, A.S. and R.C. Cammarata, *Introduction*, in *Nanomaterials - Synthesis, Properties and Applications*, A.S. Edelstein and R.C. Cammarata, Editors. 1996, IOP Publishing Ltd.: Bristol, UK.
11. Rolison, D.R., *Chemical Properties*, in *Nanomaterials - Synthesis, Properties and Applications*, A.S. Edelstein and R.C. Cammarata, Editors. 1996, IOP Publishing Ltd.: Bristol, UK.
12. Kreibig, U., *Optics of Nanosized Metals*, in *Handbook of Optical Properties - Volume II: Optics of Small Particles, Interfaces, and Surfaces*, R.E. Hummel and P. Wissmann, Editors. 1997, CRC Press. p. 145-190.
13. Forrest, D.R. *Low Cost, Atomically-Precise Manufacturing of Defense Systems: Progress and Applications*. in *Productive Nanosystems*. October 9-10, 2007. Arlington, VA: Society of Manufacturing Engineers: www.sme.org/nanosystems.
14. *IBM Unveils Two Major Nanotechnology Breakthroughs as Building Blocks for Atomic Structures and Devices*. September 4, 2007 [cited; Available from: http://www-03.ibm.com/press/us/en/pressrelease/22254.wss.
15. Dubin, C.H. *Small Steps for Mankind: Controlled-Release Gets Smarter Thanks to Nanotechnology* September 4, 2007 [cited; Available from: http://www.drugdeliverytech.com/cgi-bin/articles.cgi?idArticle=256.
16. Adamopoulos, O. and T. Papadopoulos, *Nanostructured Bioceramics for Maxillofacial Applications.* J. Mater. Sci.: Mater. Med., 2007. **18**: p. 1587-1597.
17. Dong, W., T. Zhang, J. Epstein, L. Cooney, H. Wang, Y. Li, Y.-B. Jiang, A. Cogbill, V. Varadan, and Z.R. Tian, *Multifunctional Nanowire Bioscaffolds on Titanium.* Chemistry of Materials, 2007. **19**: p. 4454-4459.

18. West, J.L. and N.J. Halas, *Engineered Nanomaterials for Biophotonics Applications: Improving Sensing, Imaging, and Therapeutics.* Annual Review of Biomedical Engineering, 2003. **5**: p. 285-292.
19. Schmidt, M., *Chapter 15. Simulations of Systems with Colloidal Particles*, in *Computational Methods in Surface and Colloid Science*, M. Borowko, Editor. 2000, Marcel Dekker: New York, NY.
20. Goodwin, J.W., *Colloids and Interfaces with Surfactants and Polymers-An Introduction*. 2004, West Sussex, England: John Wiley and Sons.
21. Brady, J.E. and F. Senese, *Chemistry: Matter and Its Changes*. 4 ed. 2004, Hoboken, NJ: John Wiley & Sons.
22. *Suspension (chemistry): http://en.wikipedia.org/wiki/*. September 10, 2007.
23. Kozan, M., B. Gharaibeh, M. Aslan, K. Saito, and M.P. Mengüç. *Effect of Fluorescent Additives on Optical Behavior of Ultra High Solid Epoxy Paint – A Polarized Light Scattering Analysis*. in *Proceedings of Painting Technology Workshop*. 2005. Lexington, KY: University of Kentucky Center for Manufacturing.
24. Chow, G.M. and K.E. Gonsalves, *Particle Synthesis by Chemical Routes*, in *Nanomaterials - Synthesis, Properties and Applications*, A.S. Edelstein and R.C. Cammarata, Editors. 1996, IOP Publishing Ltd.: Bristol, UK.
25. *General Purpose Latex Particles: http://www.dukescientific.com/*. 2007.
26. Hawes, E.D., *Directed Self-Assembly of Nano-Size Particles, PhD Dissertation*, in *Mechanical Engineering Department*. 2007, University of Kentucky: Lexington, KY.
27. Modest, M.F., *Radiative Heat Transfer*. 1993, New York: McGraw-Hill, Inc.
28. Shipway, A.N., E. Katz, and I. Willner, *Nanoparticle Arrays on Surfaces for Electronic, Optical, and Sensor Applications.* Chem Phys Chem, 2000. **1**: p. 18-52.
29. *http://www.shiseido.co.jp/com*. February 26 2007.
30. Yamada, J., A. Kawamura, Y. Miura, S. Takata, and K. Ogawa, *Study on Radiation Transfer in Human Skin for Cosmetics.* Journal of Quantitative Spectroscopy & Radiative Transfer, 2005. **93**: p. 219-230.
31. *Nanotex: http://www.nano-tex.com*. February 26 2007.
32. Heilmann, A., *Polymer Films with Embedded Metal Nanoparticles*. Springer series in materials science ; 52. 2003, Berlin ; New York: Springer. x, 216.
33. Purcell, E.M. and C.R. Pennypacker, *Scattering and Absorption of Light by Nonspherical Dielectric Grains.* The Astrophysical Journal, 1973. **186**: p. 705-714.
34. Draine, B.T., *The Discrete Dipole Approximation an Its Application to Interstellar Graphite Grains.* Astrophysical Journal, 1988. **333**: p. 848-872.
35. Draine, B.T. and J. Goodman, *Beyond Clausius-Mossotti - Wave-Propagation on a Polarizable Point Lattice and the Discrete Dipole Approximation.* Astrophysical Journal, 1993. **405**(2): p. 685-697.
36. Bohren, C.F. and D.R. Huffman, *Absorption and Scattering of Light by Small Particles*. 1983, New York: John Wiley & Sons.
37. Jackson, J.D., *Classical Electrodynamics*. 3rd edition ed. 2005: John Wiley & Sons, Inc.

38. Kozan, M., M.P. Mengüç, and S. Manickavasagam, *Hollow-Core Approach in Modeling Irregularly Shaped Metallic Nanoparticles, Poster Presentation*, in *Fourth International Conference on Radiative Transfer*. 2004, International Center for Heat and Mass Transfer: Istanbul, Turkey.
39. Wong, B.T., *Thermal Heat Transport at the Nano-Scale Level and its Application to Nano-Machining, Phd Dissertation*, in *Mechanical Engineering Department*. 2006, University of Kentucky: Lexington, KY.
40. Demarest, K.R., *Engineering Electomagnetics*. 1998, Upper Saddle River, N.J.: Prentice Hall.
41. Hecht, E., *Optics*. 3rd ed. 1998, Reading, Massachusetts: Addison Wesley Longman, Inc.
42. Osborne, N.S., H.F. Stimson, and E.F. Fiock, *A Calorimetric Determination of Thermal Properties of Saturated Water and Steam from 0 to 270 oC.* Bur. Stand. J. Res., 1930. **5**: p. 411-480.
43. Keenan, J.H. and F.G. Keyes, *Thermodynamic Properties of Steam Including Data for the Liquid and Solid Phases*. 1936, New York, NY: John Wiley and Sons.
44. Harvey, A.H. and J.M.H.L. Sengers, *Thermodynamic Properties of Water and Steam for Power Generation*. March 20, 2007: http://nvl.nist.gov/pub/nistpubs/sp958-lide/049-052.pdf.
45. *Bottom-up Methods for Making Nanotechnology Products: http://www.azonano.com*. September 11, 2007.
46. Allen, G.L., R.A. Bayles, W.W. Gile, and W.A. Jesser, *Small Particle Melting of Pure Metals.* Thin Solid Films, 1986. **144**: p. 297-308.
47. Perfect, E. and B.D. Kay, *Application of Fractals in Soil and Tillage Research: A Review.* Soil and Tillage Research, 1995. **36**: p. 1-20.
48. *Nanocatalysis: http://www.ldl.gatech.edu/research.htm*. September 12, 2007, Research Group of M. A. El-Sayed.
49. Jin, R., Y.W. Cao, C.A. Mirkin, K.L. Kelly, G.C. Schatz, and J.G. Zheng, *Photoinduced Conversion of Silver Nanospheres to Nanoprisms.* Science, 2001. **294**: p. 1901-1903.
50. Ahmadi, T.S., Z.L. Wang, T.C. Green, A. Henglein, and M.A. El-Sayed, *Shape-Controlled Synthesis of Colloidal Platinum Nanoparticles.* Science, 1996. **272**: p. 1924-1926.
51. Sun, Y. and Y. Xia, *Shape-Controlled Synthesis of Gold and Silver Nanoparticles.* Science, 2002. **298**: p. 2176-2179.
52. Malinsky, M.D., K.L. Kelly, G.C. Schatz, and R.P. Van Duyne, *Nanosphere Lithography: Effect of Substrate on the Localized Surface Plasmon Resonance Spectrum of Silver Nanoparticles.* Journal of Physical Chemistry B, 2001. **105**(12): p. 2343-2350.
53. Kozan, M., J. Thangala, R. Bogale, M.P. Mengüç, and M.K. Sunkara, *In-Situ Characterization of Dispersion Stability of WO3 Nanoparticles and Nanowires.* Journal of Nanoparticle Research, 2007 (in print), http://dx.doi.org/10.1007/s11051-007-9290-y.
54. Hou, F.Y., W. Wang, and H.T. Guo, *Effect of the Dispersibility of ZrO2 Nanoparticles in Ni-ZrO2 Electroplated Nanocomposite Coatings on the*

Mechanical Properties of Nanocomposite Coatings. Applied Surface Science, 2006. **252**(10): p. 3812-3817.
55. Schuerman, D.W., ed. Light Scattering by Irregularly Shaped Particles. 1979, Plenum Press: State University of New York at Albany, NY.
56. Vonnegut, B. *Atmospheric Ice Crystals*. in *Light Scattering by Irregularly Shaped Particles*. 1979. State University of New York at Albany: Plenum Press.
57. Cheng, R.J. *Physical Properties of Atmospheric Particulates*. in *Light Scattering by Irregularly Shaped Particles*. 1979. State University of New York at Albany: Plenum Press.
58. Mandelbrot, B.B., *Les Objets Fractals: Forme, Hasard et Dimension*. 1975, Paris: Flammarion.
59. Forrest, S.R. and T.A. Witten, *Long-Range Correlations in Smoke-Particle Aggregates.* Journal of Physics A, 1979. **12**: p. L109.
60. Witten, T.A. and L.M. Sander, *Fractal Growth: A Continuing Mystery.* Current Contents, 1993. **18**(May 3): p. 8.
61. Martin, J.E., J.P. Wilcoxon, D. Schaefer, and J. Odinek, *Fast Aggregation of Colloidal Silica.* Physical Review A, 1990. **41**(8): p. 4379-4391.
62. Jullien, R. and R. Botet, *Aggregation and Fractal Aggregates*. 1987, Singapore: World Scientific Publishing Co Pte Ltd.
63. Bolle, G., C. Cametti, P. Codastefano, and P. Tartaglia, *Kinetics of Salt-Induced Aggregation in Polystyrene Lattices Studied by Quasielastic Light Scattering.* Physical Review A, 1987. **35**(2): p. 837-841.
64. Sorensen, C.M., *Light scattering by Fractal Aggregates: A Review.* Aerosol Science and Technology, 2001. **35**(2): p. 648-687.
65. Filippov, A.V., M. Zurita, and D.E. Rosner, *Fractal-like Aggregates: Relation between Morphology and Physical Properties.* Journal of Colloid and Interface Science, 2000. **229**(1): p. 261-273.
66. Deepak, F.L., P. Saldanha, S.R.C. Vivekchand, and A. Govindaraj, *A Study of the Dispersions of Metal Oxide Nanowires in Polar Solvents.* Chemical Physics Letters, 2006. **417**: p. 535-539.
67. Bushell, G.C., Y.D. Yan, D. Woodfield, J. Raper, and R. Amal, *On Techniques for the Measurement of the Mass Fractal Dimension of Aggregates.* Advances in Colloid and Interface Science, 2002. **95**(1): p. 1-50.
68. Sorensen, C.M., *Scattering and Absorption of Light by Particles and Aggregates*, in *Handbook of Surface and Colloid Chemistry*, K.S. Birdi, Editor. 1997, CRC Press LLC. p. 533-558.
69. Govindan, R., S. Manickavasagam, and M.P. Mengüç. *On Measuring the Mueller Matrix Elements of Soot Agglomerates*. in *Radiation-I: Proceedings of the First International Symposium on Radiative Heat Transfer*. August 1995. Kusadasi, Turkey: Begell House, NY, 1996.
70. Agarwal, B.M. and M.P. Mengüç, *Forward and Inverse Analysis of Single and Multiple Scattering of Collimated Radiation in an Axisymmetric System.* International Journal of Heat and Mass Transfer, 1991. **34**(3): p. 633-647.
71. Mengüç, M.P. and S. Manickavasagam, *Radiation Transfer and Polarized Light.* International Journal of Engineering Sciences, 1998. **36**: p. 1569-1593.

72. Schaefer, D.W., J.E. Martin, P. Wiltzius, and D.S. Cannell, *Fractal Geometry of Colloidal Aggregates.* Physical Review Letters, 1984. **52**: p. 2371.
73. Mandelbrot, B.B., *The Fractal Geometry of Nature*. 1983, San Fransico, CA: W. H. Freeman.
74. Gündüz, G., *The Fractal Dimension of the Rise of an Empire.* Journal of Mathematical Sociology, 2000. **24**(4): p. 303-320.
75. Griffiths, D.J., *Introduction to Electrodynamics*. 3rd ed. 1999, Upper Saddle River, N.J.: Prentice Hall. xv, 576.
76. Siegel, R. and J.R. Howell, *Thermal Radiation Heat Transfer*. 3rd ed. 1992, Washington: Hemisphere Publication Cooperation.
77. Lilienfeld, P., *Gustav Mie: The Person.* Applied Optics, 1991. **30**(33): p. 4696-4698.
78. Manickavasagam, S. and M.P. Mengüç, *Scattering Matrix Elements of Fractal-Like Soot Agglomerates.* Applied Optics, 1997. **36**(6): p. 1337-1351.
79. Kozan, M., M.P. Mengüç, S. Manickavasagam, and C. Saltiel. *Effect of Particle Shape Irregularities on the Angular Profiles of Scattering Matrix Elements*. in *8th AIAA/ASME Joint Thermophysics and Heat Transfer Conference*. 2002. St. Louis, Missouri: American Institute of Aeronautics and Astronautics, Inc.
80. Draine, B.T. and P.J. Flatau, *User Guide for the Discrete Dipole Approximation Code DDSCAT (Version 6.0)*. 2003, http://arxiv.org/abs/astro-ph/0309069.
81. Brasil, A.M., T.L. Farias, and M.G. Carvalho, *A Recipe for Image Characterization of Fractal-Like Aggregates.* Journal of Aerosol Science, 1999. **30**(10): p. 1379-1389.
82. *floc: http://m-w.com*. 2005, Merriam-Webster Online Dictionary.
83. *Fractal: http://mathworld.wolfram.com/Fractal.html*. [cited 2005 March 2].
84. Martin, J.E. and A.J. Hurd, *Scattering from Fractals.* Journal of Applied Crystallography, 1987. **20**: p. 61-78.
85. Colbeck, I., *Fractal Analysis of Aerosol Particles.* Analytical Proceedings Including Analytical Communications, 1995. **32**(September): p. 383-386.
86. Meakin, P., *Diffusion-Controlled Cluster Formation in 2-6 Dimensional Space.* Physical Review A, 1983. **27**(3): p. 1495-1507.
87. Greene, B., *The Elegant Universe - String's the Thing: http://www.pbs.org/wgbh/nova/transcripts/3013_elegant.html*. September 13, 2007.
88. Weitz, D.A., J.S. Huang, M.Y. Lin, and J. Sung, *Limits of the Fractal Dimension for Irreversible Kinetic Aggregation of Gold Colloids.* Physical Review Letters, 1985. **54**(13): p. 1416-1419.
89. Neimark, A.V., U.O. Koylu, and D.E. Rosner, *Extended Characterization of Combustion-Generated Aggregates: Self-Affinity and Lacunarities.* Journal Of Colloid And Interface Science, 1996. **180**(2): p. 590-597.
90. Saltiel, C., Q. Chen, S. Manickavasagam, L.S. Schadler, R.W. Siegel, and M.P. Mengüç, *Identification of the Dispersion Behavior of Surface Treated Nanoscale Powders.* Journal of Nanoparticle Research, 2004. **6**(1): p. 35-46.
91. Lin, M.Y., H.M. Lindsay, D.A. Weitz, R.C. Ball, R. Klein, and P. Meakin, *Universality in Colloid Aggregation.* Letters to Nature, 1989. **339**(June 1): p. 360-362.

92. Vincze, A., R. Fata, M. Zrinyi, Z. Horvolgyi, and J. Kertsz, *Comparison of Aggregation of Rodlike and Spherical Particles: A Fractal Analysis.* Journal of Chemical Physics, 1997. **18**(8): p. 7451-7458.
93. Raper, J.A. and R. Amal, *Measurement of Aggregate Fractal Dimensions Using Static Light-Scattering.* Particle & Particle Systems Characterization, 1993. **10**(5): p. 239-245.
94. Brasil, A.M., T.L. Farias, M.G. Carvalho, and U.O. Koylu, *Numerical Characterization of the Morphology of Aggregated Particles.* Journal of Aerosol Science, 2001. **32**(4): p. 489-508.
95. Gottsleben, F. and D. Hesse, *Possibilities and Limitations of the Fractal Description of Pore Textures.* Hungarian Journal of Industrial Chemistry, 1992. **20**(2): p. 121-126.
96. Stafiej, J. and B. Badiali, *Chapter 17. Double Layer Theory: A New Point of View*, in *Computational Methods in Surface and Colloid Science*, M. Borowko, Editor. 2000, Marcel Dekker: New York, NY.
97. *Colloid:* http://en.wikipedia.org/. September 18, 2007.
98. Burns, J.L., Y.D. Yan, G.J. Jameson, and S. Biggs, *A Light Scattering Study of the Fractal Aggregation Behavior of a Model Colloidal System.* Langmuir, 1997. **13**(24): p. 6413-6420.
99. Cametti, C., P. Codastefano, and P. Tartaglia, *Light-Scattering Measurements of Slow Aggregation in Colloids: Devivation from Asymptotic Time Scaling.* Physica Review A, 1987. **36**(10): p. 4916-4921.
100. Zhou, Z.K. and B.J. Chu, *Light-Scattering Study on the Fractal Aggregates of Polystyrene Spheres - Kinetic and Structural Approaches.* Journal of Colloid and Interface Science, 1991. **143**(2): p. 356-365.
101. *Zeta Potential:* http://en.wikipedia.org. September 21, 2007.
102. *Zeta Potential:* www.silver-colloids.com/Papers/. September 21, 2007.
103. *Zeta Potential Range of Value:* www.silver-colloids.com. September 21, 2007.
104. *Influence of pH on Zeta Potential:* www.silver-colloids.com. September 21, 2007.
105. *Determining the Particle Size of a Suspension or Emulsion*. 1999, Warwick, RI: Colloidal Dynamics Inc.
106. Singham, S.B. and C.F. Bohren, *Scattering of Unpolarized and Polarized Light by Particle Aggregates of Different Size and Fractal Dimension.* Langmuir, 1993. **9**: p. 1431-1435.
107. Van de Hulst, H.C., *Light Scattering by Small Particles*. 1957, New York: John Wiley and Sons, Inc.
108. Mountain, R.D. and G.W. Mulholland, *Light Scattering from Simulated Smoke Aggregates.* Langmuir, 1988. **4**: p. 1321-1326.
109. Bushell, G. and R. Amal, *Measurement of Fractal Aggregates of Polydisperse Particles Using small-Angle Light Scattering.* Journal of Colloid and Interface Science, 2000. **221**(2): p. 186-194.
110. Bushell, G., R. Amal, and J. Raper, *The Effect of Polydispersity in Primary Particle Size on Measurement of the Fractal Dimension of Aggregates.* Particle & Particle Systems Characterization, 1998. **15**(1): p. 3-8.

111. Dimon, P., S.K. Sinha, D.A. Weitz, C.R. Safinya, G.S. Smith, W.A. Varady, and H.M. Lindsay, *Structure of Aggregated Gold Colloids.* Physical Review Letters, 1986. **57**(5): p. 595-598.
112. Hasmy, A., R. Vacher, and R. Jullien, *Small-Angle Scattering by Fractal Aggregates: A Numerical Investigation of the Crossover between the Fractal Regime and the Porod Regime.* Physical Review B, 1994. **50**(2): p. 1305-1308.
113. Klusek, C., *Characterization of the Morphology of Fractal-Shaped Soot Agglomerates via the Mueller Scattering Matrix, Master's thesis*, in *Mechanical Engineering Department*. 1999, University of Kentucky: Lexington, KY.
114. Chen, Q., C. Saltiel, S. Manickavasagam, L.S. Schadler, R.W. Siegel, and H. Yang, *Aggregation Behavior of Singlewalled Carbon Nanotubes in Dilute Aqueous Suspension.* J. Colloid Interface Sci., 2004. **280**: p. 91-97.
115. Saltiel, C., S. Manickavasagam, M.P. Mengüç, and R. Andrews, *Light-Scattering and Dispersion Behavior of Multiwalled Carbon Nanotubes.* J. Opt. Soc. Am. A, 2005. **22**(8): p. 1546-1554.
116. Chen, S.-H. and J. Teixeira, *Structure and Fractal Dimension of Protein-Detergent Complexes.* Physical Review Letters, 1986. **57**(20): p. 2583-2586.
117. Amal, R., D. Gazeau, and T.D. Waite, *Small-Angle X-Ray Scattering of Hematite Aggregates.* Particle & Particle Systems Characterization, 1994. **11**(4): p. 315-319.
118. Microsoft, *Compaq Visual Fortran Professional 6.1.0*. 1999.
119. Hasmy, A., M. Foret, J. Pelous, and R. Jullien, *Small-Angle Neutron-Scattering Investigation of Short-Range Correlations in Fractal Aerogels - Simulations and Experiments.* Physical Review B, 1993. **48**(13): p. 9345-9353.
120. Mackowski, D.W., *Calculation of Totla Cross Sections of Multiple-Sphere Clusters.* Journal of Optical Society of America, A, 1994. **11**(11): p. 2851-2861.
121. Eden, M. in *Proceedings of the Fourth Berkeley Symposium on Mathematical Statistics and Probability*. 1961. University of California, Berkeley.
122. Witten, T.A. and L.M. Sander, *Diffusion-Limited Aggregation, A Kinetic Critical Phenomenon.* Physical Review Letters, 1981. **47**(19): p. 1400-1403.
123. Meakin, P., *Diffusion-Controlled Cluster Formation in Two, Three, and Four Dimensions.* Physical Review A, 1983. **27**(1): p. 604-607.
124. Jullien, R. and R. Botet, *Scaling Properties of the Surface of the Eden Model in D = 2, 3, 4.* Journal of Physics A-Mathematical and General, 1985. **18**(12): p. 2279-2287.
125. Jullien, R. and R. Botet, *Surface Thickness in the Eden Model.* Physical Review Letters, 1985. **54**(18): p. 2055-2055.
126. Microsoft, *Microsoft Developer Studio Fortran Power Station 4.0.* 1995.
127. Meakin, P., *Formation of Fractal Clusters and Networks by Irreversible Diffusion-Limited Aggregation.* Physical Review Letters, 1983. **51**(13): p. 1119-1122.
128. Kolb, M., R. Botet, and R. Jullien, *Scaling of Kinetically Growing Clusters.* Physical Review Letters, 1983. **51**(13): p. 1123-1126.
129. Botet, R., R. Jullien, and M. Kolb, *Hierarchical Model for Irreversible Kinetic Cluster Formation.* Journal of Physics A, 1984. **17**: p. L75-L79.

130. Jullien, R., *Comment on "Diffusion-Limited Aggregation in Two Dimensions".* Physical Review Letters, 1985. **55**(16): p. 1697.
131. Jullien, R., *A New Model of Cluster Aggregation.* Journal of Physics A-Mathematical and General, 1986. **19**: p. 2129-2136.
132. Oles, V., *Shear-Induced Aggregation and Breakup of Polystyrene Latex-Particles.* Journal of Colloid and Interface Science, 1992. **154**(2): p. 351-358.
133. Meakin, P., *Diffusion-Controlled Deposition on Fibers and Surfaces.* Physica Review A, 1983. **27**(5): p. 2616-2623.
134. Racz, Z. and T. Vicsek, *Diffusion-Controlled Deposition: Cluster Statics and Scaling.* Physical Review Letters, 1983. **51**(26): p. 2382-2385.
135. Meakin, P. and F. Family, *Diverging Length Scales in Diffusion-Limited Aggregation.* Physica Review A, 1986. **34**(3): p. 2558-2560.
136. Meakin, P., *Multiple-Contact Diffusion-Limited-Aggregation Model.* Physica Review A, 1986. **33**(6): p. 4199-4205.
137. Meakin, P., *Universality, Nonuniversality, and the Effects of Anisotropy on Diffusion-Limited Aggregation.* Physica Review A, 1986. **33**(5): p. 3371-3389.
138. Meakin, P. and Z.R. Wasserman, *Some Universality Properties Associated with the Cluster-Cluster Aggregation Model.* Physics Letters A, 1984. **103**(6-7): p. 337-341.
139. Riefler, N., S. di Stasio, and T. Wriedt, *Structural Analysis of Clusters Using Configurational and Orientational Averaging in Light Scattering Analysis.* Journal of Quantitative Spectroscopy & Radiative Transfer, 2004. **89**: p. 323-342.
140. *Electric Double Layer: www.silver-colloids.com/Tutorials/Intro/pcs17A.html*. September 21, 2007.
141. *Electric Double Layer: www.cartage.org.lb/en/themes/sciences/chemistry*. September 21, 2007.
142. Govindan, R., *Measurement of the Mueller Matrix Elements for Identification of the Structure of Soot Agglomerates in Flames, MS Thesis*, in *Department of Mechanical Engineering*. 1996, University of Kentucky: Lexington, KY.
143. Aslan, M., J. Yamada, M.P. Mengüç, and J.A. Thomasson. *Radiative Properties of Individual Cotton Fibers: Experiments and Predictions*. in *8th AIAA/ASME Joint Thermophysics and Heat Transfer Conference*. 2002. St. Louis, Missouri: American Institute of Aeronautics and Astronautics, Inc.
144. Aslan, M.M., C. Crofcheck, D. Tao, and M.P. Mengüç, *Evaluation of Micro-Bubble Size and Gas Hold-up in Two-Phase Gas–Liquid Columns via Scattered Light Measurements.* Journal of Quantitative Spectroscopy & Radiative Transfer, 2006. **101**: p. 527-539.
145. Aslan, M., *Size and Shape Prediction of Colloidal Metal Oxide MgBaFeO particles from Light Scattering Measurements. Internal report*. 2006, Radiative Transfer Laboratory, Mechanical Engineering Department, University of Kentucky: Lexington, KY.
146. Kozan, M. and M.P. Mengüç, *Exploration of Fractal Nature of WO3 Nanowire Aggregates.* J. Quant. Spectrosc. Radiat. Transfer, 2007 (in print), http://dx.doi.org/10.1016/j.jqsrt.2007.08.020).
147. Baba, J.S., J.R. Chung, and G.L. Cote, *Laser Polarization Noise Elimination in Sensitive Polarimetric Systems.* Optical Engineering, 2002. **41**: p. 938-942.

148. Kozan, M., *Use of Read.for and Matrix.for for Processing Incremental EPLS Measurements. Internal report.* 2005, Radiative Tansfer Laboratory, Mechanical Engineering Department, University of Kentucky: Lexington, KY.
149. Nicolosi, V., D. Vrbanic, A. Mrzel, J. McCauley, S. O'Flaherty, D. Mihailovic, W.J. Blau, and J.N. Coleman, *Solubility of Mo6S4.5I4.5 Nanowires.* Chemical Physics Letters, 2005. **401**(1-3): p. 13-18.
150. Bogale, R., *Stability of Metal Oxide Nanowires versus Nanoparticles in Solvent Based Dispersion, MS Thesis*, in *Department of Chemical Engineering*. 2005, University of Louisville: Louisville.
151. Bushell, G.C., R. Amal, and J.A. Raper, *The Effect of a Bimodal Primary Particle Size Distribution on Scattering from Hematite Aggregates.* Physica A, 1996. **233**(3-4): p. 859-866.
152. Lin, M.Y., R. Klein, H.M. Lindsay, D.A. Weitz, R.C. Ball, and P. Meakin, *The Structure of Fractal Colloidal Aggregates of Finite Extent.* Journal of Colloid and Interface Science, 1990. **137**(1): p. 263-280.
153. Stone, S., G. Bushell, R. Amal, Z. Ma, H.G. Merkus, and B. Scarlett, *Characterization of Large Fractal Aggregates by Small-Angle Light Scattering.* Measurement Science & Technology, 2002. **13**(3): p. 357-364.
154. Sorensen, C.M. and D.J. Fischbach, *Patterns in Mie scattering.* Optics Communications, 2000. **173**(1-6): p. 145-153.
155. Lee, C.S., J.S. Lee, and S.T. Oh, *Dispersion Control of Fe2O3 Nanoparticles Using a Mixed Type of Mechanical and Ultrasonic Milling.* Materials Letters, 2003. **57**(18): p. 2643-2646.
156. Mandzy, N., E. Grulke, and T. Druffel, *Breakage of TiO2 Agglomerates in Electrostatically Stabilized Aqueous Dispersions.* Powder Technology, 2005. **160**: p. 121-126.
157. Aubert, C. and D.S. Cannell, *Restructuring of Colloidal Silica Aggregates.* Physical Review Letters, 1986. **56**(7): p. 738-741.
158. Beattie, J.K., J.K. Cleaver, and T.D. Waite, *Anomalous Aggregation Behaviour of Aluminium Oxyhydroxides.* Colloids and Surfaces a-Physicochemical and Engineering Aspects, 1996. **111**(1-2): p. 131-138.
159. Gan, F. and L. Xu, eds. *Photonic Glasses*. 2006, World Scientific Publishing Company
160. Waite, T.D., J.K. Cleaver, and J.K. Beattie, *Aggregation Kinetics and Fractal Structure of gamma-Alumina Assemblages.* Journal of Colloid and Interface Science, 2001. **241**(2): p. 333-339.
161. Bentley, A.K., A.B. Ellis, G.C. Lisensky, and W.C. Crone, *Suspensions of Nickel Nanowires as Magneto-Optical Switches.* Nanotechnology, 2005. **16**(10): p. 2193-2196.
162. Smith, P.A., C.D. Nordquist, T.N. Jackson, T.S. Mayer, B.R. Martin, J. Mbindyo, and T.E. Mallouk, *Electric-Field Assisted Assembly and Alignment of Metallic Nanowires.* Applied Physics Letters, 2000. **77**(9): p. 1399-1401.
163. Majolino, D., F. Mallamace, P. Migliardo, N. Micali, and C. Vasi, *Elastic and Quasielastic Light-Scattering-Studies of the Aggregation Phenomena in Water Solutions of Polystyrene Particles.* Physical Review A, 1989. **40**(8): p. 4665-4674.

164. Amal, R., J.R. Coury, J.A. Raper, W.P. Walsh, and T.D. Waite, *Structure and Kinetics of Aggregating Colloidal Hematite.* Colloids and Surfaces, 1990. **46**(1): p. 1-19.

VITA

Mehmet Kozan was born on July 1, 1974, in Ilgaz, Cankiri in Turkey. He received his B.S. degree in Chemical Engineering in January 1997 at the Middle East Technical University, Ankara, Turkey as an Honor Student (Ranked 9th of a class of 185 students). He got his M.S. degree in the same department under Professor Nevin Selçuk with his thesis entitled "Investigation of Radiative Heat Transfer in Freeboard of a 0.3 MW AFBC Test Rig". He served at his department as a Teaching Assistant until August 2000, when he started his PhD work under Professor M. Pinar Mengüç in the Mechanical Engineering Department at the University of Kentucky, Lexington, KY, USA. He served at this department as Research Assistant until August 2004 and as Teaching Assistant until December 2006.

ACADEMIC POSITIONS

- Mechanical Engineering Department, UK, Lexington, KY, USA
  Teaching Assistant, August 2004-December 2006
  Research Assistant, August 2000-May 2004
- Chemical Engineering Department, METU, Ankara, Turkey
  Teaching Assistant, January 1997-July 2000

AWARDS

- Center for Computational Sciences Fellowship, 2003-2004: University of Kentucky, Lexington, KY.
- NATO A-1 Science Fellowship, 2000-2002: Scientific and Technical Research Council of Turkey, TÜBİTAK, Ankara.
- National Merit Scholarship, 1989-1992: Ministry of Education of Turkey, Ankara.

JOURNAL ARTICLES

1. **Kozan, M.** and M. P. Mengüç, *Exploration of Fractal Nature of WO3 Nanowire Aggregates*. Journal of Quantitative Spectroscopy & Radiative Transfer, 2007 (*doi:10.1016/j.jqsrt.2007.08.020*).

2. **Kozan, M.**, J. Thangala, R. Bogale, M. P. Mengüç, and M. K. Sunkara, *In-Situ Characterization of Dispersion Stability of WO3 Nanoparticles and Nanowires.* Journal of Nanoparticle Research, 2007 (*doi: 10.1007/s11051-007-9290-y*).

3. **Kozan, M.** and M. P. Mengüç, *Aggregation of WO3 Nanowires Augmented by Electrolyte Addition* (*in preparation*).

4. **Kozan, M.** and N. Selçuk, *Investigation of Radiative Heat Transfer in Freeboard of a 0.3 MWt AFBC Test Rig*, Combustion Science and Technology, 2000, **153**: p. 113-126.

PEER REVIEWED CONFERENCE PAPERS

1. **Kozan, M.** and M. P. Mengüç, *Exploration of Fractal Nature of WO3 Nanowire Aggregates* in Fifth International Symposium on Radiative Transfer, 2007. Bodrum, Turkey: International Center for Heat and Mass Transfer.

2. **Kozan, M.**, M. P. Mengüç, S. Manickavasagam, and C. Saltiel, *Effect of Particle Shape Irregularities on the Angular Profiles of Scattering Matrix Elements* in *8th AIAA/ASME Joint Thermophysics and Heat Transfer Conference*, 2002. St. Louis, Missouri: American Institute of Aeronautics and Astronautics, Inc.

3. **Kozan, M.** and N. Selçuk, *Investigation of Radiative Heat Transfer in Freeboard of a 0.3 MWt AFBC Test Rig* in Mediterranean Combustion Symposium, 1999. Kusadasi, Turkey: International Center for Heat and mass Transfer.

PAPERS PUBLISHED IN PROCEEDINGS AND POSTER PRESENTATIONS

1. **Kozan, M.**, M. Aslan, B. Gharaibeh, M. P. Mengüç and K. Saito, *Effect of Fluorescent Additives on Optical Behavior of Ultra High Solid Epoxy Paint—A Polarized Light Scattering Analysis* in Proceedings of Painting Technology Workshop, 2005. Lexington, KY: University of Kentucky Center for Robotics and Manufacturing Systems.

2. **Kozan, M.**, M. P. Mengüç, and S. Manickavasagam, *Hollow-Core Approach in Modeling Irregularly Shaped Metallic Nanoparticles* in Fourth International Conference on Radiative Transfer, 2004. Istanbul, Turkey: International Center for Heat and Mass Transfer.

3. Mengüç M. P., **M. Kozan**, B. Wong, S. Manickavasagam, and C. Saltiel, *A Compact System for Characterization of Size and Shape of Nano-Particles and Agglomerates*. Third International Symposium on Radiative Transfer, 2001. Antalya, Turkey: International Center for Heat and Mass Transfer.